



UNIVERSIDAD DE CONCEPCIÓN
FACULTAD DE CIENCIAS FÍSICAS Y MATEMÁTICAS

CONCEPTUAL DESIGN OF AN L-BAND DUAL POLARIZATION INTERFEROMETER FOR GALACTIC ISM STUDIES

*Diseño conceptual de un interferómetro de polarización dual en banda L
para estudios del medio interestelar galáctico*

Por: Nicolás Ignacio Montero Améstica

Tesis presentada a la Facultad de Ciencias físicas y matemáticas de la
Universidad de Concepción para optar al grado académico de Magíster en
Astronomía

Enero 2023
Concepción, Chile

Profesor Guía: Rodrigo Andrés Reeves Díaz





© 2022, Nicolás Ignacio Montero Améstica

Se autoriza la reproducción total o parcial, con fines académicos, por cualquier medio o procedimiento, incluyendo la cita bibliográfica del documento



Para la Tinita, Juanita, Jose y mi Rockito

AGRADECIMIENTOS

Primero que todo agradecer a mi familia por todo. A mi querida madre Yannette, que me acompañó a dar el primer paso de mi carrera al viajar conmigo para matricularme en la universidad y resaltar lo fuerte que fue y es al dejar un hijo estudiar casi 2500 km lejos de ella. A mi padre Marco, que siempre me pregunta si conozco a los astrónomos que salen en la televisión y por ir a dejarme hasta la pensión donde viví durante mi época de estudiante universitario. A mi hermano Rodrigo, por preocuparse en que iba a ser después de terminar mi carrera y a mi hermano Marco, que me contaba cosas sobre medicina cada vez que nos veíamos en Santiago o durante vacaciones. Un pilar fundamental en mi vida

Escribir estas palabras me producen un sentimiento de nostalgia al recordar seres queridos que ya no están y momentos que me gustaría volver a vivir. Sin embargo, la vida sigue, y gracias a esto pude emparejarme con Katia, una amiga de muchos años, a quien le quiero agradecer todo su apoyo en momentos que ella sabe me fueron complicados, gracias por creer en mí en todo momento y agradecer también a toda su familia que me preguntaban cosas de astronomía y generaba en mí un impulso para seguir con mis estudios y esta tesis. Agradecer a mi abuela Albertina, que tristemente ya no se encuentra con nosotros y no me vio como astrónomo ni como estudiante de magister, pero sí me vio formarme como profesional y adulto durante muchos años, nunca te olvidare mami.

Agradecer a mis amigos de la carrera, infancia y aquellos que se fueron, pero seguimos en contacto, compañeros y profesores de pregrado, muchas gracias por todo estos años de nuevos aprendizajes y logros.

Finalmente, agradecer a mi profesor guía Rodrigo Reeves, por haber aceptado ser mi profesor guía todos estos años y por qué gracias a él me interesa la instrumentación astronómica y la radioastronomía. Gracias a David Arroyo que junto al profe me motivaban cada reunión que teníamos y por su inconmensurable paciencia y apoyo. Gracias totales.

Resumen

La Universidad de Concepción tiene un radiotelescopio de 3 metros de apertura empleado para la observación de la línea de 21 cm de Hidrogeno neutro con una resolución angular de $\sim 5^\circ$. La línea de HI caracteriza el medio frío, cálido y de baja densidad atómica dentro del ISM. 245 MHz más arriba aproximadamente, en la misma banda de frecuencia (L), es posible detectar la línea de transición radical de Hidroxilo (OH) a 1.665 GHz. Esta se utiliza para caracterizar el medio interestelar molecular de densidad intermedia. Con respecto a esto, ambas líneas se pueden detectar con un sistema receptor de banda L único. Aquí, se informan simulaciones de síntesis de apertura para observaciones a 1,42 GHz y 1,665 GHz con 5 arreglos de antena diferentes. Esta investigación tuvo como objetivo evaluar el rendimiento del beam sintetizado de 5 configuraciones de antenas diferentes de 8 antenas en total de 3 metros de apertura. Se realizaron simulaciones de observaciones de síntesis de apertura y limpieza de imágenes utilizando el paquete Common Astronomy Software Applications. Se evaluaron un total de 12 tiempos de integración y 9 declinaciones de fuente diferentes con un total de 108 escenarios diferentes por configuración. Adicionalmente, se produjeron imágenes limpias con 3 esquemas de peso diferentes por resultados para analizar el efecto en el beam sintetizado. Los resultados de las curvas de fuente de elevación mostraron que las declinaciones de -30° a -70° presentaron una excelente observabilidad de la fuente durante largas horas de observación. Los largos tiempos de integración y las observaciones de alta declinación de la fuente mejoraron la simetría circular del beam sintetizado, logrando una resolución angular de menos de 2 minutos de arco en 3 de las 5 configuraciones evaluadas. Configuraciones orientadas NE y NO produjeron beams alargados con ángulos de posición altos, sin embargo, la configuración abierta reorganizada produjo beams uniformes durante la mayoría de los escenarios probados. En conclusión, es posible lograr una resolución angular de menos de 2 minutos de arco con 3 de las 5 configuraciones evaluadas.

Keywords – Simulación, CASA, Radio-astronomía, Efecto Zeeman

Abstract

The University of Concepcion has a 3 meter radio telescope employed for galactic HI line observation with $\sim 5^\circ$ angular resolution. The HI line characterizes the cold, warm and low atomic density medium within the ISM. 245 MHz above approximately, in the same frequency band (L), it is possible to detect the OH radical transition line at 1.665 GHz. It is used to characterize the intermediate molecular density medium. Then, both lines can be detected with a unique L-band receiver system. Here, is reported aperture synthesis simulations for observations at 1.42 GHz and 1.665 GHz with 5 different arrays. This study aims to evaluate synthesized beam performance of 5 different antenna array configurations with a total of 8 antennas with 3 meters in diameter. It was performed aperture synthesis simulations and image cleaning using the Common Astronomy Software Applications package. A total of 12 different integration times and 9 different source declination were evaluated for each configuration with a total of 108 different scenarios per configuration. Additionally, clean images were produced with 3 different weighting schemes per results to analyze the effect in the synthesized beam. Results of elevation source curves showed that declination from -30° to -70° present excellent source observability during long observation hours. Long integration times and high source declination observations improved the synthesized beam circular symmetric and angular resolution less than 2 arc-minute were achieved. North-East and North-West oriented configurations produced elongated beams with high position angles, however, a rearranged open configuration produced uniform beams during the majority of the tested scenarios. In conclusion, it is possible to achieve less than 2 arc-minute angular resolution with 3 of the 5 tested configurations.

Keywords – Simulations, CASA, Radio-astronomy, Zeeman effect

Contents

AGRADECIMIENTOS	i
Resumen	ii
Abstract	iii
1 Introduction	1
1.1 Motivation	1
1.1.1 Scientific Motivation	1
1.1.2 The Current Radio-Telescope	4
1.2 Project Overview	5
1.2.1 General Objective	6
1.2.2 Specific Objectives	7
1.3 Thesis Organization	8
2 State Of Art	9
2.1 Contextualization	9
2.1.1 The HI and OH Lines	10
2.1.2 Molecular Clouds	13
2.1.3 Molecular Filaments	16
2.1.4 Mass to Magnetic Flux Ratio	18
2.2 Magnetic Field Diagnostic Tools	21
2.2.1 Dust Grain Polarization	23
2.2.2 Synchrotron Radiation	23
2.2.3 Rotation Measure (Faraday Effect)	23
2.2.4 Goldreich-Kylafis Effect	25
2.2.5 Davis-Chandrasekhar-Fermi Method	26
2.2.6 Zeeman Effect	27
2.2.6.1 Brief Historical Background	27
2.2.7 The Effect	28
2.2.8 Measuring Magnetic Fields With the Zeeman Effect	29
2.2.9 HI and OH Zeeman Effect Observational Results	33
2.2.9.1 Interferometric Observations of Magnetic Fields	34
2.3 Aperture Synthesis	37
2.3.1 Interferometry and Aperture Synthesis	37

2.4	About the Bibliographic Revision	39
3	Methods and Execution	40
3.1	Dual Polarization Instrument Approach	40
3.1.1	Primordial Requirements	41
3.2	Antenna Array	42
3.2.1	Sensitivity	42
3.2.2	Overview of the Antenna Array Simulations	43
3.2.2.1	Simulation Mechanics	44
3.2.2.2	Input Sky Model Image	45
3.2.2.3	Creating and Adding an Antenna Array Configuration in CASA	47
3.2.2.4	Executing Simobserve Task	50
3.2.3	Image Cleaning	51
4	Results	54
4.1	The Dual Polarization Design Method	54
4.2	Antenna Array Configuration Results	57
4.2.1	Necessary Bandwidth and Channels	57
4.2.2	Sensitivity	59
4.2.3	Array Positions	62
4.2.4	Simulation Results	65
4.2.4.1	UV-coverage and Dirty Beams	67
4.2.4.2	Major and Minor Beam Width	72
4.2.4.3	Synthesized Beam Eccentricity	75
4.2.4.4	Dirty v/s Clean Image	77
5	Discussion and Conclusion	84
5.1	Array Design Conclusions	84
5.1.1	Future Work	86
	References	88
	Appendix	94
A	Radio-Polarimetry	94
A1	Polarization	94
A2	Techniques For Working With Polarization	99
A2.1	Stokes Parameters	99
A2.2	Jones Formalism	103
A2.3	Mueller Formalism	106
A2.4	Linear and Circular Basis	108
A2.5	Jones to Mueller matrix	109
A3	Radio-Polarimetry	110
A3.1	Native Linear and Circular Dual Polarization Systems	111
A3.2	Element Mueller Matrix	112

A4	The Radio Interferometric Measurement Equation	116
A5	Sensitivity	120
	A5.0.1 Interferometer sensitivity	121
	A5.0.2 Sensitivity in imaging (NRAO)	122



List of Tables

2.2.1 Most used lines in Zeeman observations. $Z = 2\Delta\nu_z$. For the full table see Crutcher & Kemball (2019) Crutcher and Kemball (2019)	32
3.2.1 Parameters for the created observatory added in the observatories copy table in CASA. The provisional name for this observatory is SCientific and Academic L-band dual Polarization Interferometer (ScALPI).	49
3.2.2 Primordial <code>simobserve</code> arguments chosen for each (5) antenna configuration observation simulation. A total of 9 different declination and 12 total observation time were simulated for each antenna configuration, i.e, 108 results per configuration.	51
3.2.3 Principal <code>tclean</code> arguments used for image cleaning. PSF FWHM stands for Point Spread Function Full Width at Half Maximum.	52
4.1.1 Dimensions for each parameter from Fig. 4.1.2 using Eq. 4.1.1.	57
4.2.1 Theoretical resolution properties of the 5 proposed configurations. B_{max} is the maximum antenna separation, B_{min} is the minimum antenna separation, θ_{HPBW} is the synthesized beam width (FWHM), and θ_{MRS} is the maximum recoverable scale visible to the array. $\theta_{HPBW} \propto \lambda/B_{max}$ and $\theta_{MRS} \propto \lambda/B_{min}$, both in radians.	66
A2.1 The 6 common normalized Jones vectors used to represent fully polarized light.	104

List of Figures

1.1.1 3 meters mesh-parabolic dish antenna in the WenuLafquen observatory at the University of Concepcion. Notice the 12 arms acting as "ribs" and the feed horn antenna. Image from the note Panorama Udec	5
1.2.1 (a) Satellite view of the surroundings of the WLK site. (b) Zoomed region of the WLK site (lat 36.842795° (S), Lon 73.025° (O) and elevation ~ 150 m). Maps generated with the free and open code Quantum Geographic Information System (QGIS version 3.16.13) using Google Maps Hybrid as layer map	6
2.1.1 Tidal interactions in M81 group revealed by observation of atomic Hydrogen at 1.42 GHz. Image from Yun (1999)	10
2.1.2 This HI4PI map was produced using data from the 100-m Max-Planck radio telescope in Effelsberg, Germany and the 64-m CSIRO radio telescope in Parkes, Australia. The image intensity reflects the total hydrogen content. The plane of the Milky Way Galaxy runs horizontally across the middle of the image. Image credit: Benjamin Winkel / HI4PI Collaboration.	11
2.1.3 Left: In the upper image the proton and electron have equal spin i.e. parallel, but in the lower image the electron flips his spin from parallel to anti-parallel and a photon is emitted with a wavelength of 21-cm or 1420 MHz. Right: Illustration of 21-cm line transition from Voyager plaque, proving the importance of this line for the humankind.	12
2.1.4 Image of ^{2}CO $J = 1-0$ emission constructed from the Center for Astrophysics campaign to examine the high-latitude sky survey. Image from Heyer and Dame (2015)	14
2.1.5 The H_2 mass surface density as a function of Galactic radius Credits. Image from Heyer and Dame (2015)	15
2.1.6 The Orion A Molecular Cloud. The image is a composite of the wavelengths of 70 microns (blue), 160 microns (green) and 250 microns (red) and spans about 2.4 X 1.3 degrees. North is to the left and east is up. Credit: Orion A ESA/Herschel/Ph. André, D. Polychroni, A. Roy, V. Könyves, N. Schneider for the Gould Belt survey Key Programme	16

2.1.7	Left: Herschel/SPIRE 250 μm image of B211/B213 presented in light blue and purple respectively. Right: Display of optical and infrared polarization vectors from Heyer et al. (2008), Heiles (2000), and Chapman et al. (2011) tracing the magnetic field orientation in the B211/L1495 region, The green, blue, and black segments in the lower right corner represent the average position angles of the polarization vectors, low-density striations (structures perpendicular to the main filament), and B211 filament, respectively. Credits: Palmeirim et al. (2013)	17
2.1.8	Filament width in function of column density for 3 different simulations in Federrath (2016) . the horizontal dotted lines show the average filament width.	18
2.1.9	Dots above the line are sub-critical and below are super-critical. Image credits Crutcher and Kemball (2019)	21
2.2.1	Starlight polarization of 8662 stars. The orientation of each star's polarization is indicated by a short line whose length L in great-circle degrees is $L = [4 < 2P]^\circ$, where P is the percentage polarization; for L , is plotted whichever of the two quantities is smaller. Image from Heiles and Crutcher (2005)	24
2.2.2	Spectrum detected by Vershuur (1968) . Credits: T. Robishaw, Zeeman splitting opportunities with the ngVLA - NRAO (2017)	30
2.2.3	Zeeman effect for neutral Hydrogen: ideal and real Zeeman spectral line profile from Heiles (1989)	31
2.2.4	B_z or B_{los} from different regions in the Milky Way in function of the volume density, where $n(\text{HI})$ is the density of HI and $2n(\text{H}_2)$ is the volume density of molecular Hydrogen. Notice how B_z is approximately constant from 1 to 100 cm^{-3} densities and evolve exponentially as $B_z \propto n^{2/3}$ for higher densities and elements. Image from Crutcher et al. (2010) . Legend for this work.	34
2.2.5	Zeeman-splitting detections for the line-of-sight magnetic field component in the Orion/Barnard Loop. Positive fields are represented by crosses and negative fields by squares. The lines are stellar polarization data, references within Heiles (1997) . Image from Heiles (1997)	35
2.2.6	OH Zeeman Stokes I and V profiles toward NGC2024 at the peak B_{LOS} position from VLA mapping (Crutcher et al., 1999a). Right: Map of B_{LOS} (color) from OH Zeeman. Contours are C18O intensities and yellow line segments are dust polarization directions (Hildebrand et al., 1995). The magnetic field in the plane of the sky is perpendicular to the dust polarization, hence roughly along the minor axis of the molecular cloud defined by C18O (horizontal in the figure). Image from Crutcher et al. (1999)	36
3.2.1	CASA workflow. Gray arrow indicates the simulations and analysis order.	43

3.2.2 (a) Input sky model image created with CASA package. The image has a size of 512×512 pixels and is sampled at 4 arc-seconds per pixel. Image is presented with <code>imview</code> CASA task. (b) Sky coverage during the simulated observations	46
4.1.1 Stepped septum polarizer front view. Image from Kim et al. (2012) .	56
4.1.2 Stepped septum draw with each parameter. K is the distance from feed output to septum and L is the distance from probe to rear wall. The angle α is equal to the arctan of 0.626, which is equal to 32.047 degrees. Image credits Lucas Teske	56
4.2.1 Theoretical spectral line sensitivity of OH line. General calculations parameters are 8 antennas of 3 meters in diameter, dual-polarization and 50 % of correlator and antenna efficiency, respectively. 8 different system temperature and 4 different bandwidth were tested. Top left graph has the same spectral configurations as in Sarma et al. (2013) . Top right has 0.8 MHz, bottom left 1.6 MHz and bottom right 3.2 MHz bandwidth, respectively.	61
4.2.2 Theoretical spectral line sensitivity of HI line. General calculations parameters are 8 antennas of 3 meters in diameter, dual-polarization and 50 % of correlator and antenna efficiency, respectively. 8 different system temperature tested. Spectral parameters are from Sarma et al. (2000)	62
4.2.3 Theoretical spectral line sensitivity of HI line. General calculations parameters are 8 antennas of 3 meters in diameter, dual-polarization and 50 % of correlator and antenna efficiency, respectively. 8 different system temperature tested. Spectral parameters are from Sarma et al. (2002)	63
4.2.4 Antenna position for the WLK array configurations. White circle has a radii of 169 meters which corresponds to the maximum antenna separation distance. Maps generated with the open and free code Quantum Geographic Information System (QGIS version 3.16.13) using Google Maps Hybrid as layer map. White arrow points North and antenna symbols are not to scale.	64
4.2.5 Antenna position for the E-CONF-A array configurations. White circle has a radii of 287 meters which corresponds to the maximum antenna separation distance. Maps generated with the open and free code Quantum Geographic Information System (QGIS version 3.16.13) using Google Maps Hybrid as layer map. White arrow points North and antenna symbols are not to scale.	65
4.2.6 Antenna position for the E-CONF-B array configurations. White circle has a radii of 579 meters which corresponds to the maximum antenna separation distance. Maps generated with the open and free code Quantum Geographic Information System (QGIS version 3.16.13) using Google Maps Hybrid as layer map. White arrow points North and antenna symbols are not to scale.	66

4.2.7	Antenna position for the E-CONF-C array configurations. White circle has a radii of 665 meters which corresponds to the maximum antenna separation distance. Maps generated with the open and free code Quantum Geographic Information System (QGIS version 3.16.13) using Google Maps Hybrid as layer map. White arrow points North and antenna symbols are not to scale.	67
4.2.8	Antenna position for the MW-C+D array configurations. White circle has a radii of 509 meters which corresponds to the maximum antenna separation distance. Maps generated with the Quantum Geographic Information System (QGIS version 3.16.13) using Google Maps Hybrid as layer map. White arrow points North and antenna symbols are not to scale.	68
4.2.9	Elevation curves for the 9 different tested source declination at 36.841° (S) latitude and 73.025° (W) longitude. Observation time (red line) is for a total of 12 hours. X axis in each images are relative hours.	69
4.2.10	U, V plane coverage for 2 hour synthesis simulation results. From top to bottom are WLK, E-CONF-A, E-CONF-B, E-CONF-C and MW-C+D configuration, respectively. Left to right columns are declination from -10° to -90° . Plots created with CASA task <code>plotms</code>	70
4.2.11	U, V plane coverage for 12 hour synthesis simulation results. From top to bottom are WLK, E-CONF-A, E-CONF-B, E-CONF-C and MW-C+D configuration, respectively. Left to right columns are declination from -10° to -90° . Plots created with CASA task <code>plotms</code>	71
4.2.12	All configurations cleaned synthesized beams for 1 hour aperture synthesis simulation at 1.665 GHz for the image model at -10° declination. Top to bottom rows are Natural, Briggs and Uniform weights, respectively. Top left rectangle shows the θ_{maj} , θ_{min} and position angle, respectively. Each image has the same scale. Minimum synthesized beam values were left to -0.4 to 1 <i>Jy/beam</i> to color-scale all images.	72
4.2.13	All configurations cleaned synthesized beams for 12 hour aperture synthesis simulation at 1.665 GHz for the image model at -10° declination. Top to bottom rows are Natural, Briggs and Uniform weights, respectively. Top left rectangle shows the θ_{maj} , θ_{min} and position angle, respectively. Each image has the same scale. Minimum synthesized beam values were left to -0.4 to 1 <i>Jy/beam</i> to color-scale all images.	73

4.2.14	All configurations cleaned synthesized beams for 12 hour aperture synthesis simulation at 1.665 GHz for the image model at -80° declination. Top to bottom rows are Natural, Briggs and Uniform weights, respectively. Top left rectangle shows the θ_{maj} , θ_{min} and position angle, respectively. Each image has the same scale. Minimum synthesized beam values were left to -0.4 to 1 $Jy/beam$ to color-scale all images.	74
4.2.15	Histogram plots of the FWHM size comparison for Natural weighting scheme. 50 bins were used. j sub-index corresponds to the configuration in the numerator and k sub-index corresponds to the configuration in the denominator.	75
4.2.16	Size comparison of Natural/Briggs (blue) and Natural/Uniform (orange) fitted FWHM. 30 bins were used. j sub-index correspond to Natural weighting in the numerator and k sub-index corresponds to Briggs or Uniform weighting in the denominator.	76
4.2.17	2D Gaussian beam shape. P.A. means position angle.	76
4.2.18	Major synthesized beam θ_{maj} (arcmin) evolution at 12 different integration time weighted by 9 different source declination for each configuration. First row shows the dirty major beam results, second, third and fourth rows present the Natural, Briggs (Robust = 0.5) and Uniform weighted beam, respectively. Y-axis labels in each sub-graphic start and end with the minimum and maximum value of θ_{maj}	77
4.2.19	Minor synthesized beam θ_{min} (arcmin) evolution at 12 different integration time weighted by 9 different source declination for each configuration. First row shows the dirty major beam results, second, third and fourth rows present the Natural, Briggs (Robust = 0.5) and Uniform weighted beam, respectively. Y-axis labels in each sub-graphic start and end with the minimum and maximum value of θ_{min}	78
4.2.20	Eccentricity (ϵ) evolution at 12 different integration time weighted by 9 different source declination for each configuration. First row shows the dirty major beam results, second, third and fourth rows present the Natural, Briggs (Robust = 0.5) and Uniform weighted beam, respectively. Y-axis labels in each sub-graphic start and end with the minimum and maximum value of ϵ	79
4.2.21	Histograms of the fitted beam width eccentricity for all the configurations for each weighting schemes used during the imaging process.	80

4.2.2	(a): Dirty image, i.e., real image data convolved with the Uniform weighting synthesized beam. Zero cleaning iterations applied on this image data. (b): Clean image, i.e., cleaned image after 500 iterations with the Hogbom cleaning algorithm Högbom (1974). (c): Residual map after cleaning. Simulations results are from the sky-model image at -10 deg in declination and 1 hour of observation only using MW-C+D configuration 4.2.8.	81
4.2.2	(a): Dirty image, i.e., real image data convolved with the Uniform weighting synthesized beam. Zero cleaning iterations applied on this image data. (b): Clean image, i.e., cleaned image after 500 iterations with the Hogbom cleaning algorithm. (c): Residual map after cleaning. Simulations results are from the sky-model image at -80 deg in declination and 12 hour of observation only using MW-C+D configuration 4.2.8.	82
4.2.2	(a): Dirty image, i.e., real image data convolved with the Uniform weighting synthesized beam. Zero cleaning iterations applied on this image data. (b): Clean image, i.e., cleaned image after 500 iterations with the Hogbom cleaning algorithm. (c): Residual map after cleaning. Simulations results are from the sky-model image at -10 deg in declination and 1 hour of observation only using WLK configuration 4.2.4.	83
A1.1	Polarization Ellipse	95
A1.2	The two components of the electric field oscillating in the x and y plane in the z direction. The total electric field is the blue line and forms a line in the xy plane.	97
A1.3	The two components of the electric field oscillating in the x and y plane in the z direction with the same magnitude (amplitude) but with a 90° phase. The total electric field forms a helix that moves trough time in the z direction and draw a circle in the xy plane.	98
A1.4	The total electric field forms a elliptical helix that moves trough time in the z direction and draw ellipse in the xy plane.	98
A2.1	The Poincare sphere	102
A2.2	The polarization angle χ is measured from X to Y, or from North to East. In dust polarization observation, this angle gives the orientation of the plane-on-the-sky magnetic field component, i.e, morphology.	103

- A3.1 Block diagram of dual-polarized (A and B) single-dish system. The noise diode (a.k.a. cal) output is injected through short cables and directional couplers with combined phase delays ϕ_A and ϕ_B . The total voltage gain of polarization channel A is $g_A = gA1gA2$; the voltage gains are complex, with an amplitude and a phase. The total cable length for channel A is length L_A , which includes the run from the dish to the correlator input so it can be very long (more than 1 km at the Green Bank Telescope). The thick lines represent mechanical structures or passive electronics that do not change with time; the thin lines represent active electronics and other circuitry that do change with time and need calibration. Image from [Robishaw and Heiles \(2021\)](#). 112
- A4.1 Block diagram showing a simple model of an interferometer that can be modelled with the RIME. Radiation from a source propagates through free space to two telescopes, p and q. After passing through the telescope's analogue chain, the two signals are interfered in a cross-correlator. Credits: D.C. Price and O. Smirnov (2015) [Price and Smirnov \(2015\)](#) 117



Chapter 1

Introduction

1.1 Motivation

1.1.1 Scientific Motivation

Stars are formed by the gravitational collapse of an interstellar parsec-scale molecular gas cloud [Krumholz \(2015\)](#) [Crutcher \(2012\)](#), however, the process of formation and evolution remains an open question in contemporary astrophysics. To answer it, it is fundamental to unveil different physical process that intervene, e.g., structure fragmentation, mass accretion, shock-waves, cooling and heating process. As well as a few physical parameters, e.g., magnetic fields, mass, temperature or angular momentum, which are believed to play a crucial role or not, in the process of formation and evolution of molecular gas clouds and stars.

More than three decades ago prior to the Herschel observations, it was pointed out by many authors the presence of parsec-scale filamentary structures inside nearby interstellar clouds and their crucial importance for star formation. Thanks to Herschel's space telescope observation in the *IR* and *NIR* spectrum surveys, it was possible to image clearly these molecular filamentary structures. The ubiquity of filaments in Herschel imaging surveys suggests the formation of filaments precedes star formation in the cold ISM, and is tied to processes acting within the clouds themselves. These filaments seem to be ubiquitous and a fundamental block in the star formation process. The last, makes molecular filaments excellent candidates

for star/cloud formation and evolution study.

Additionally, nowadays it is also known that magnetic fields are ubiquitous in the Universe [Haverkorn \(2015\)](#). They are detected in large and small scale structures, e.g., in the arms and Halo of spiral galaxies and in atomic and molecular gas structures, respectively. Furthermore, in smaller structures like proto-stellar disks, stars and Black Holes, magnetic fields are also present. Study of magnetic fields should provide a valuable opportunity to shed further light on the formation and evolution of interstellar clouds as well as on star formation [Hull and Zhang \(2019\)](#) [Crutcher and Kemball \(2019\)](#).

With respect to magnetic fields in molecular filaments, dust polarization observations with the Herschel space telescope provided information only of the plane-of-the-sky magnetic field (B_{pos}) component orientation and percentage, not magnitude. However, it revealed that magnetic field lines of the B_{pos} tend to be oriented parallel with respect to the main filament, e.g., the Herschel view of Taurus B211/3 filament in [Palmeirim et al. \(2013\)](#) showing a perpendicular orientation of B_{pos} with respect to main filament.

Techniques based on the Zeeman effect are the only ones available for a direct measurement of the magnetic field strengths in interstellar clouds. This effect provides information of the magnitude and direction of the line-of-sight magnetic field component [Crutcher et al. \(1993\)](#). The expected results doing Zeeman in filaments are a helical or toroidal morphology of \vec{B} , like the results of HI Zeeman splitting presented in [Heiles \(1997\)](#) of the Eridanus/Orion region.

Most used lines for Zeeman effect observations are HI, OH and CN [Crutcher and Kemball \(2019\)](#). These three lines characterize the low, intermediate and high density medium in diffuse cold diffuse atomic clouds and molecular gas clouds. Additionally, CCS [Nakamura et al. \(2019\)](#) and SO [Cazzoli et al. \(2017\)](#) molecules could provide an excellent characterization of the high density medium too. Unfortunately, to observe these lines, is strictly required different receiver instrumentation. However, for the HI (1.42 GHz) and OH (1.665, 1.667, 1.772 GHz) transition lines, only one receiver system should be necessary to detect the Zeeman effect in both, e.g., VLA and Arecibo observatories.

However, Zeeman effect observation in the radio-spectrum are very time demanding. It requires good sensitivity, which is inversely proportional to the square root

of the integration time, i.e., $\sigma \propto T_{sys}/\sqrt{\Delta\nu\Delta\tau}$. Additionally, nearby molecular filaments (< 700 pc distance based on the observed by the Herschel Gould Belt Survey [André et al. \(2010\)](#)) have full width at half maximum widths of ~ 0.1 pc for the skeleton part and a few pc, i.e., arc-minute or even arc-second angular scale, requiring high angular resolution. This could be resolved with the development of a hundred-meter antenna. However, large telescopes are costly to produce (price $\propto D^{2.7}$ ¹), the support architecture is heavy and leaves to gravity instability problems. Fortunately, the university already poses a 3 meters telescope located in a large area and a laboratory focused in astronomical instrumentation.

All the presented above motivated the design of a scientific/academic L-band dual polarization interferometer focused on magnetic fields observation through Zeeman effect in the low-atomic and intermediate-molecular density medium in nearby south-hemisphere molecular and atomic clouds.

The following work was focused in magnetic fields and their characterization through the Zeeman effect in nearby ISM (<700 pc) molecular filaments from the south pole, e.g., Corona Australis ($\alpha = 19:03:34.5240$ $\delta = -37:03:57.685$ $d = 130$ pc), Musca ($\alpha = 12:27:15.0130$ $\delta = -71:32:14.192$ $d = 200$ pc) or Lupus ($\alpha = 15:41:08.90$ $\delta = -34:02:55.028$ $d = 200$ pc). On the part of magnetic fields, their observations are motivated to prove two opposite theories, strong or weak magnetic field theory, testing if magnetic fields play (or not) a critical role in the star formation and evolution process within molecular structures, mostly as a pressure force (against gravity), driven matter into the core and interacting with other physical parameters, e.g., kinematics, temperature and turbulence.

With respect to the choice of Zeeman effect technique for magnetic field observations, it is the only diagnostic tool capable to measure magnitude and direction [Crutcher et al. \(1993\)](#) [Heiles \(1989\)](#) [Crutcher et al. \(1999\)](#) (morphology) in star formation regions at different density scales ($n = 10 - 10^6 \text{cm}^{-3}$) via the observation of the HI atomic line and different transitions of OH, CN, CCS, SO, H₂O and CH₃OH molecules [Crutcher and Kemball \(2019\)](#), where the highest densities are observed in the molecular clouds' cores, therefore, Zeeman effect observations can be used as tracers of high-density regions and magnetized structures. Also, with the Zeeman effect observational results is possible to use and compare them with others diagnostics tools results, e.g., DCF method or GK effect [Hull and](#)

¹Lecture by Craig Walker.

Zhang (2019).

Nevertheless, the mentioned atomic and molecular lines are observed at different frequencies, from the cm to the mm range, so, different instrumentation are necessary to detect each line, however, for the HI and OH, which characterize the low and intermediate density medium and are observed at 21 cm (1.42 GHz) and 18 cm (1.665 GHz) respectively, exists a small spectral gap, making the observation of this two lines achievable with one unique instrument installed in a radio-telescope, available at the university. Section below describes the current radio-telescope that also motivated this work.

1.1.2 The Current Radio-Telescope

The WenuLafquen² observatory is located at 1.9 km from the University of Concepcion, Chile. Its geographic coordinates are latitude 36.842795° South, longitude 73.025° East and at an altitude of ~ 150 m. over the sea level. It has a 3 meters mesh-parabolic dish antenna showed in Fig. 1.1.1 built in 2016 by members of the university for academic purposes. Currently, it operates only at 1.42 GHz and has a prime focus optical configuration, i.e., the radiation is reflected by the dish and received by the feed horn located at the focus. Additionally, this feed horn only receives left circular polarization (LCP).

In the optical context, this antenna has ~ 5 degrees angular resolution and only one polarization product, left circular polarization. The last one means null polarization observations capabilities (appendix A). Additionally, it was built for spectral line observation of the 21 cm. (1.42 GHz) atomic Hydrogen emission line focused in undergraduate courses for experimental experience in radio-astronomy. One example work realized with this radio-telescope was the measurement of the Milky Way rotation curve using the 21 cm. line. Academically, the antenna works for medium radio-astronomy courses and even for engineering courses. However, for advanced courses (postgraduate) and even for advertising purposes, this antenna lags behind in comparison with others instruments in Chilean universities or even international.

For the forgoing, it is clear that a new instrument would be positive for the observatory and university progress. In the academic context, this could open

²From Mapudungun, Mapuche language, Wenu: Sky, Lafken: Sea/Lake, *Lake of the heights*



Figure 1.1.1: 3 meters mesh-parabolic dish antenna in the WenuLafquen observatory at the University of Concepcion. Notice the 12 arms acting as "ribs" and the feed horn antenna. Image from the note [Panorama Udec](#)

new courses, motivate students to learn and work during the building process but more important, in the formation of new astronomers and engineers. Additionally this new instrument does not seek to compete with others, but to compare and complement with old and recent studies of the cosmos and forms new professional by teaching the current and new observational techniques.

1.2 Project Overview

This work is presented as a major and extremely ambitious new instrument at the University of Concepcion (Chile): The conceptual design of a scientific and academic L-band dual-polarization interferometer for galactic interstellar medium studies with arc-minutes angular power resolution. The conceptual design consists of 8 parabolic dish antenna of 3 m. in diameter to create an antenna array configuration for aperture synthesis in the future. Additionally, it is designed with intentions to detect the 1.42 GHz (HI) and 1.665 GHz (OH) lines with a dual polarization feed horn antenna. A series of 5 different configuration were created and evaluated through aperture synthesis simulations using the Common Astronomy Software Applications (CASA) package and Python scientific modules.

Figure 1.2.1 shows a satellite view of the surroundings and area for the 5 proposed array configurations. Projections of sensitivity, integration time, analysis of angular and spectral resolution, uv-coverage and Point-spread-function are presented in this work. Additionally, a tentative design method of a stepped septum polarizer with circular-dual polarization outputs is presented.

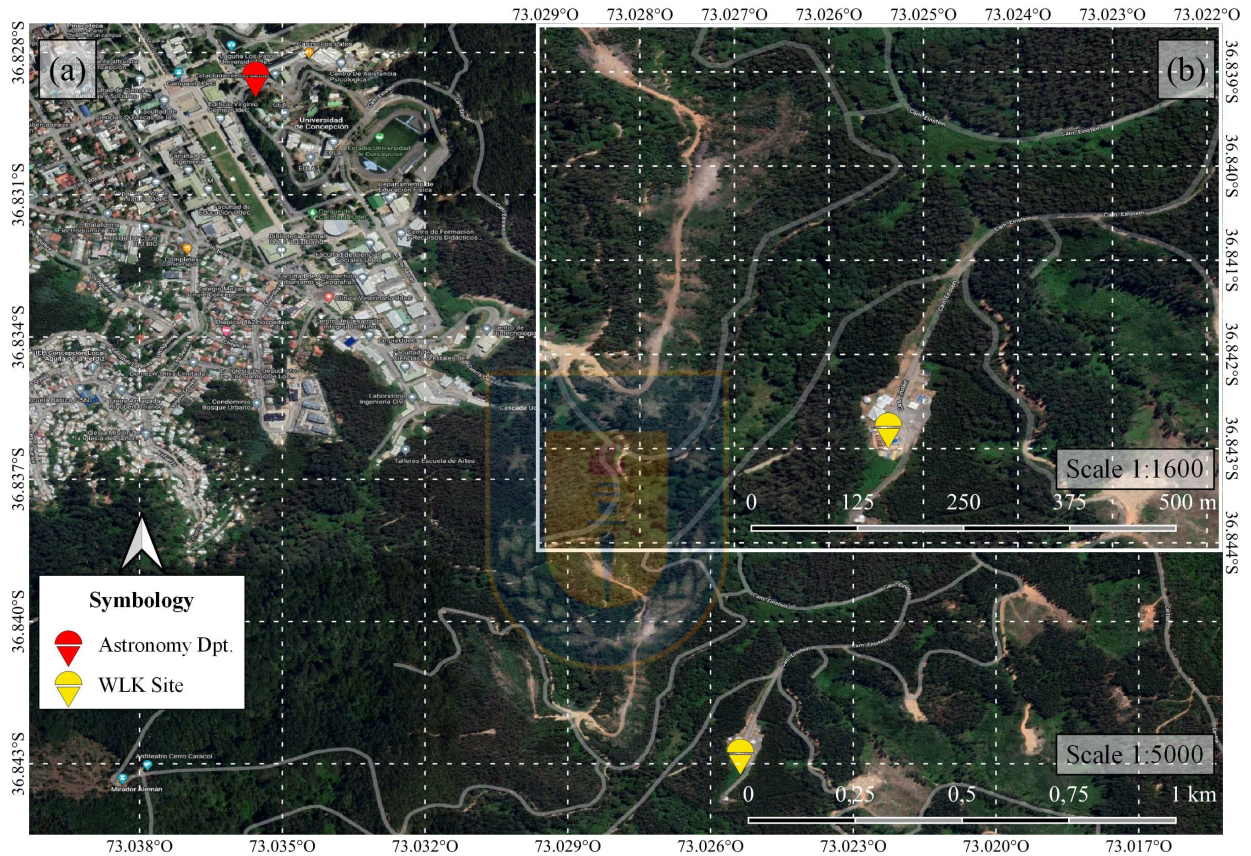


Figure 1.2.1: (a) Satellite view of the surroundings of the WLK site. (b) Zoomed region of the WLK site (lat 36.842795° (S), Lon 73.025° (O) and elevation ~ 150 m). Maps generated with the free and open code Quantum Geographic Information System (QGIS version 3.16.13) using Google Maps Hybrid as layer map.

1.2.1 General Objective

Create a conceptual design of 8-antennas array configurations for scientific and academic aperture synthesis studies in the HI (1.42 GHz) and OH (1.665 GHz) galactic ISM at the Universidad de Concepción.

1.2.2 Specific Objectives

- Research on antennas for dual-polarization observations to work in a 3m radio telescope and for spectral observation from 1.4 to 1.7 GHz.
- Design and evaluate an interferometric array with arcmins angular resolution
 - Investigate and chose a way to design and evaluate the antenna array configuration
 - Propose and design an antenna array configuration with 8 antennas of 3 meters in diameter
 - Create an antenna primary beam response for the 3 meters radio telescope
 - Research and create a simple sky model image to be observed during the aperture synthesis simulations
 - Simulate aperture synthesis observations with a image model to evaluate the array design
 - Analyze the u,v plane coverage for different arrays and source declination and observation times
 - Analyze the synthesized beams
 - Define a metric to qualify the antenna array configuration performance
 - Make a projection measurement for the expected sensitivity with the full system

Also, it is necessary to emphasize some points

- The dual-pol antenna design is focused to work in a 3 meters antenna like the one located in the University.
- The antenna's characteristics for the proposed array are the same as the current 3 meters antenna
- The proposed array configuration (location of antennas) and the number of antennas will be chosen based on the feasibility place and connection to the control room.

- The proposed array configuration has 8 maximum number of antennas. It is based on the current existence of a ROACH FPGA board in the University capable to correlate 8 antennas, i.e., multiplication, time average, addition and subtraction of orthogonal polarization products.

and, in the limitations

- In the global context of pandemic, the whole process of meetings has been carried out remotely via video calls.
- Due to the pandemic, the computational work related with the simulations have been carried out with a low performance computer, making this process extremely slow and sometimes with any results due to a “freezing” of the computer
- Aperture synthesis observation simulations only run in a Linux OS and in Linux or macOS respectively

1.3 Thesis Organization

The following thesis is organized as follows

Chapter 2 presents the scientific context.

Chapter 3 describes the mechanics of the simulation and image analysis process. Additionally, the dual-polarization system investigation is described.

Chapter 4 presents the results and its interpretation of the aperture synthesis simulations and the dual polarization system investigation.

Chapter 5 presents the discussion and conclusions of the results. Additionally, a brief description of a tentative future work is presented.

Appendix A describes extensive but crucial information related with this thesis framework.

Chapter 2

State Of Art

2.1 Contextualization

It has become increasingly clear that cosmic magnetic fields are pervasive, ubiquitous, and likely important in the properties and evolution of almost everything in the Universe, from planets to quasars [Haverkorn \(2015\)](#) [Troland and Crutcher \(2008\)](#), but, for the role played by magnetic fields in low and high mass star formation has remained uncertain [Haverkorn \(2015\)](#). Mapping the morphology of magnetic fields in low- and high-mass star-forming regions is therefore critical to better understand how magnetic fields affect the star-formation process at early times, and how the role of the field changes relative to other dynamical effects (e.g., turbulence, rotation, thermal and radiation pressure, and gravitational collapse) as a function of spatial scale, source environment, and source mass.

The interstellar medium is the space between the astronomical objects inside the Galaxy. It is all the matter and radiation that fills the space. Here we can find molecular clouds, dust, cosmic rays, but principally Hydrogen. This hydrogen is located in all the disk of the Galaxy and in gas clouds of approximately 60 % of the gas in the Milky Way is in HI regions, where the hydrogen is predominantly atomic [Draine \(2011\)](#). Also, the observation of the HI 21-cm line can show us invisible interactions at the visible spectrum, e.g., [figure 2.1.1](#) shows streamers visible only in HI clearly which demonstrates that the M81 group is an interacting system of galaxies.

In the results presented in [Heiles and Troland \(2003\)](#) of the Millennium Arecibo

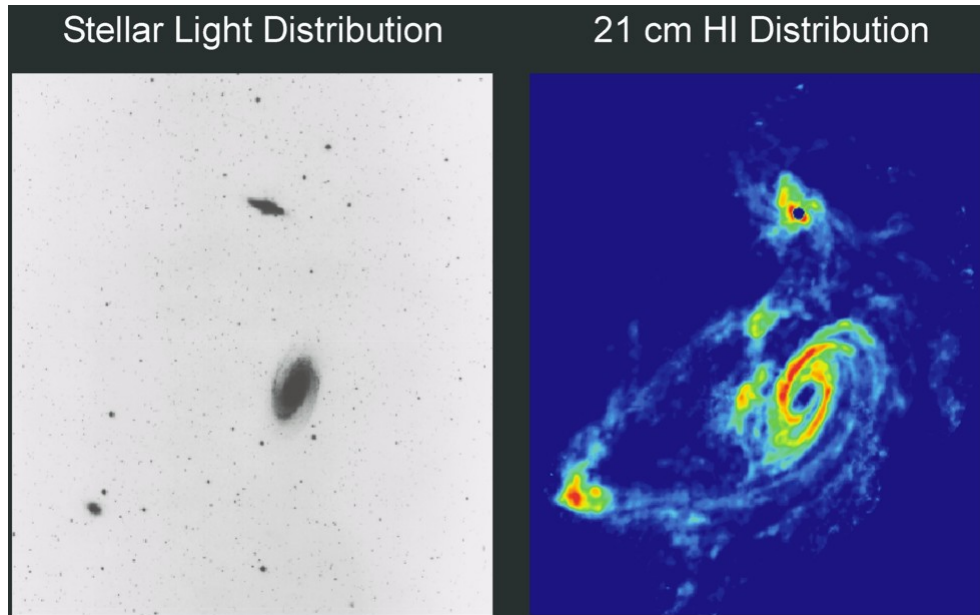


Figure 2.1.1: Tidal interactions in M81 group revealed by observation of atomic Hydrogen at 1.42 GHz. Image from Yun (1999).

21 Centimeter Absorption-Line survey, it was supported the idea that in the solar neighborhood (i.e., within ~ 500 pc of the Sun), interstellar HI is found primarily in two distinct phases: the cold neutral medium (CNM), which has a clumpy structure and the warm neutral medium (WNM) with a diffuse distribution. About 40 % of the HI (by mass) is in the CNM. The remaining 60 % of the HI is in the WNM phase.

In the classical two-phase picture, both phases exist in pressure equilibrium with stable phases for temperatures of $T < 300$ K (CNM) and $T < 5000$ K (WNM) embedded in a hot ionized phase Kalberla and Kerp (2009). Gas at intermediate temperatures is considered to be transient. The masses of this clouds range from a few thousand solar masses and sizes between 10 – 100 pc.

2.1.1 The HI and OH Lines

The Hydrogen atom is the most abundant element in the Universe and with that assumption was that Jan Oort wanted to find a radio spectral line that would allow him to detect objects more than a few thousand light-years away. He wanted a spectral line that would allow the Doppler shift of the line to be easily observed, and he suggested to his graduate student, H. C. van de Hulst, that hydrogen might be a good candidate, so, Hendrik C. van de Hulst predicted in 1944 the existence

of the 21-cm hyper-fine line of neutral interstellar Hydrogen or the 1420 MHz radio frequency signal. The observation of this line is one of the most used radio spectral line in Astronomy. Due to the long extension of the atomic hydrogen around the galactic disk (figure 2.1.2), it is also used to measure galactic rotation. Also, is extremely used to prove cosmological theories, e.g., observing this line at higher redshift ($z \sim 7 - 15$) could prove the epoch of re-ionization (EoR), the time when the universe was only ~ 400 millions and the first Galaxies, Quasars and Pop III stars started to re-ionize the medium. Intensity mapping technique ,e.g., HERA (Hydrogen Epoch of Re-ionization Array), is an example of how detect this radiation. Another use is the mass estimation of a galaxy using the virial mass theorem and to measure the strength of the static magnetic field in the HI cloud using the Zeeman effect that shifts the frequency of the line and is proportional to the strength of the magnetic field. As we can see, observation of atomic Hydrogen has many utilities in astronomy.

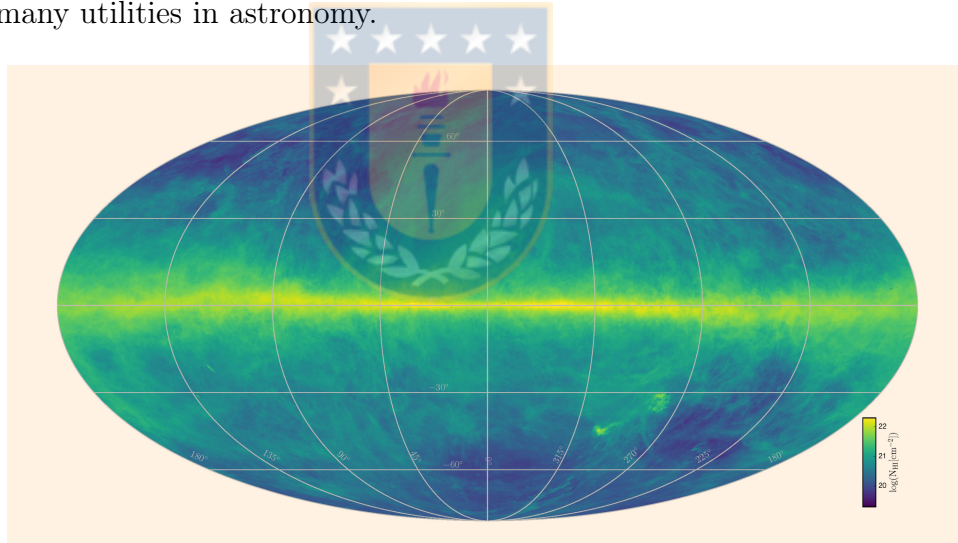


Figure 2.1.2: This HI4PI map was produced using data from the 100-m Max-Planck radio telescope in Effelsberg, Germany and the 64-m CSIRO radio telescope in Parkes, Australia. The image intensity reflects the total hydrogen content. The plane of the Milky Way Galaxy runs horizontally across the middle of the image. Image credit: Benjamin Winkel / HI4PI Collaboration.

But, how is this line produced? The neutral Hydrogen atom has one proton in the nucleus and one electron orbiting at the ground state or more closed to the nucleus [Kalberla and Kerp \(2009\)](#). The particles have intrinsic spin, that can be understood as how these particles are aligned. In quantum theory, the particles can have only two possible alignments or spins, parallel or anti-parallel, so for the HI atom when the electron and the proton both have parallel spin and the electron change

the spin to anti-parallel, this emits a photon carrying an energy of 5.9×10^{-6} eV and a frequency of 1420.405751 MHz (21 cm). This happens approximately 11 million years but how the Hydrogen is the most abundant element in the Universe this line can be detected mostly anywhere but more precisely in HI clouds and Spirals arms of galaxies.

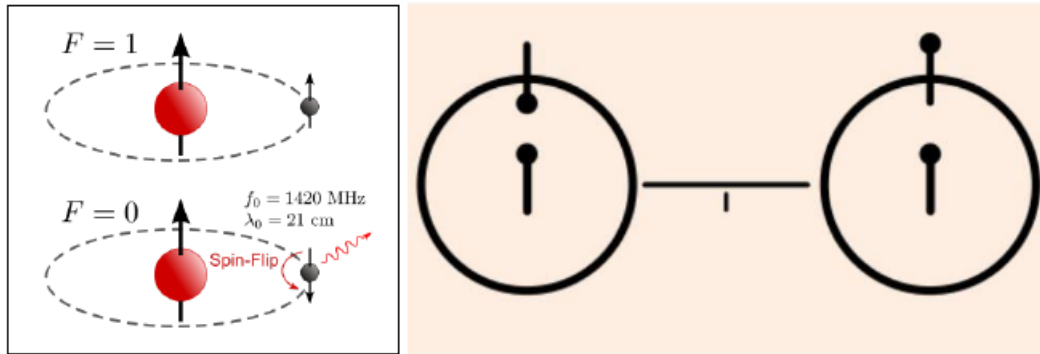


Figure 2.1.3: Left: In the upper image the proton and electron have equal spin i.e. parallel, but in the lower image the electron flips his spin from parallel to anti-parallel and a photon is emitted with a wavelength of 21-cm or 1420 MHz. **Right:** Illustration of 21-cm line transition from Voyager plaque, proving the importance of this line for the humankind.

The interstellar medium (ISM) is composed by atomic and molecular gas clouds, radiation, dust and magnetic fields (and others). It is practically the matter and radiation that exist inside a galaxy and between stars. Within the ISM exist the atomic and molecular gas clouds, which are parsec scale structures with different physical properties with respect to the empty space. Atomic clouds are principally composed by atomic Hydrogen making it observable in the 21-cm line.

With respect to the Hydroxyl (OH) molecule, it has a few transitions observable at different wavelengths. For the purpose of this work, only the four 18 cm ground states of OH at 1612, 1665, 1667, and 1720 MHz were studied. At these wavelengths, it is possible to characterize the magnetic fields of molecular cloud cores [Troland and Crutcher \(2008\)](#).

With the observation of both atomic and molecular lines it is possible to characterize the atomic and molecular density medium in molecular clouds.

2.1.2 Molecular Clouds

Individual clouds are separated into categories based on their optical appearance: diffuse, translucent, or dark, depending on the visual extinction AV through the cloud. These are enormous regions out of which stars form. Molecular Clouds are the densest regions of interstellar space, i.e., from $n \sim 100 - 10^3 \text{cm}^{-3}$ and inside densities $n \sim 10^4 - 10^7 \text{cm}^{-3}$ for the cores [Crutcher \(2012\)](#) [Krumholz \(2015\)](#). The typical sizes range from 10 - 100 pc, masses between $10^3 - 10^7 M_{\odot}$ and temperatures between 10 - 30 K. Inside these clouds where due to gravitational collapse the process of star formation occurs, however, the understanding of this process is very far away from being resolved.

Molecular clouds are the birthplace of stars, the study of star formation is possible by observing in the infrared spectrum and millimeter to centimeter spectrum. Optical and UV is also used to study molecular clouds, principally stars and other properties [Madau and Dickinson \(2014\)](#). Infrared observation gives information about the dust which is used to calculate temperature and magnetic field morphology within the clouds [André et al. \(2010\)](#). Sub/millimeter observations are used to study also temperature and magnetic fields within them but additionally the mass, density and kinematics. In the centimeter spectral range is also possible the study of magnetic fields but only in the low and intermediate density medium [Crutcher et al. \(1993\)](#) [Heiles and Crutcher \(2005\)](#) [Troland and Crutcher \(2008\)](#).

The following section talks about large molecular gas structures only, i.e., molecular clouds and filaments, which are of critical importance in understanding the process of star formation. Molecular gas is located in the disk of spiral galaxies, is abundant in star-forming galaxies like ours, and occurs over a very wide range of densities. Take up only 1 % of the volume of the Milky Way galaxy but represent approximately half the mass of it. It can be found in giant structures with very irregular morphology, these are giant molecular clouds, molecular clouds, molecular cloud complex (groups of molecular clouds), filaments (intrinsically related with molecular clouds), gas clumps, dense cores (inside molecular clouds and filaments) and in proto-planetary disks. [Figure 2.1.4](#) shows a map of CO emission for the Milky Way galaxy, which is intrinsically related with the quantity of molecular Hydrogen, the main component of the molecular gas, also, is possible to see that

the molecular gas is distributed along the disk spiral arms. This molecular gas distribution is commonly observed in spiral galaxies.

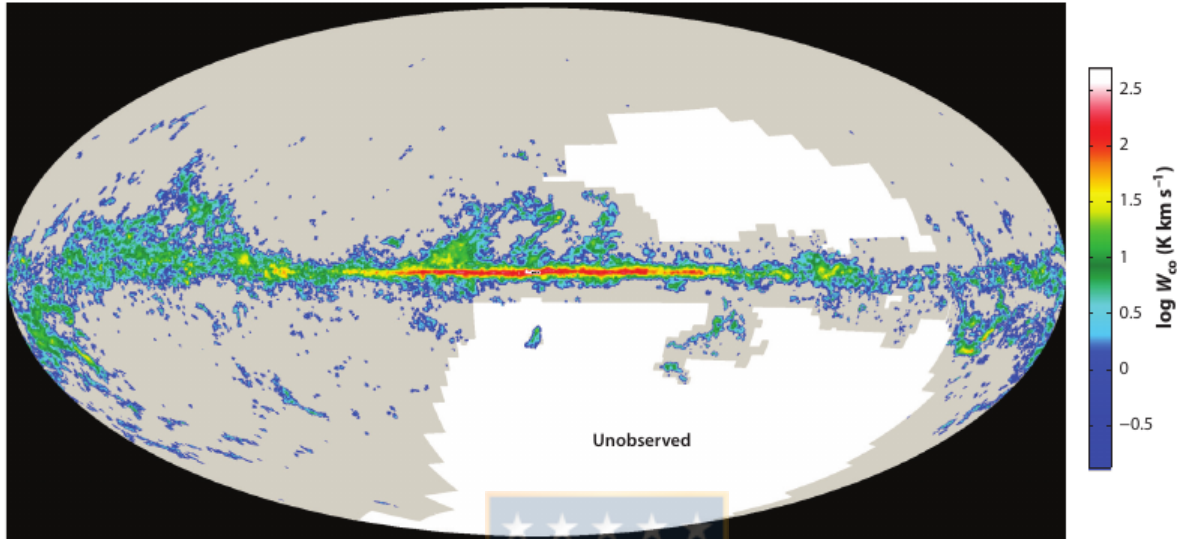


Figure 2.1.4: Image of ${}^2\text{CO}$ $J = 1-0$ emission constructed from the Center for Astrophysics campaign to examine the high-latitude sky survey. Image from [Heyer and Dame \(2015\)](#)

The mass of the H_2 gas in the Milky way is $1.0 \pm 0.3 \times 10^9 M_\odot$ (does not include the mass of associated helium) and most of the H_2 gas (60 -70%) is located inside the solar circle 2.1.5. however, to observe molecular structures astronomers must rely on tracers because, materials which make up only a small portion of a cloud, but which are easy to detect. Astronomers use several kinds of tracers when studying molecular clouds. Dust makes a good tracer (figure 2.1.6): particles embedded in molecular clouds can block light from background stars, revealing the cloud as a silhouette. When warmed by the radiation from nearby young stars, the dust can also glow in the far infrared and millimeter region of the spectrum. The $J = 1-0$ rotational transition of CO at a frequency of 115 GHz and line emission from other molecules in the millimeter band offers an accessible and valuable spectroscopic proxy to molecular hydrogen in high column density regime ($> 10^{21} \text{cm}^{-2}$). The choice of the CO molecule as a a molecular Hydrogen tracer is not random (obviously). Its low rotational transitions ($J_u \leq 4$) occur within the millimeter and submillimeter bands, which are accessible using ground-based telescopes. These transitions lie only 5-22 K above the ground state, enabling CO to probe the coldest regions in the ISM. Once the link between star formation

and molecular gas was established, both theoretical and observational efforts accelerated. The measurement of mass and others physical parameters in molecular gas structures is by the determination of the H_2 column density (molecular hydrogen gas column density, N_{H_2}). This parameter is generally determined from the application of the CO – H_2 conversion factor, X_{CO} Bolatto et al. (2013), such that $N_{H_2} = X_{CO}W_{CO}$ cm², in which W_{CO} is the ¹²CO surface brightness integrated over the velocity width of the cloud, $W_{CO} = \int T_B(v)dv$ K km s⁻¹, and $T_B(v)$ is the ¹²CO spectrum in units of brightness temperature. The CO – H_2 conversion factor is not universal, however, for the calculation of the molecular Hydrogen gas mass of the Milky Way mentioned before, X_{CO} was equal to 2×10^{20} molecules cm² (K km s⁻¹)⁻¹.

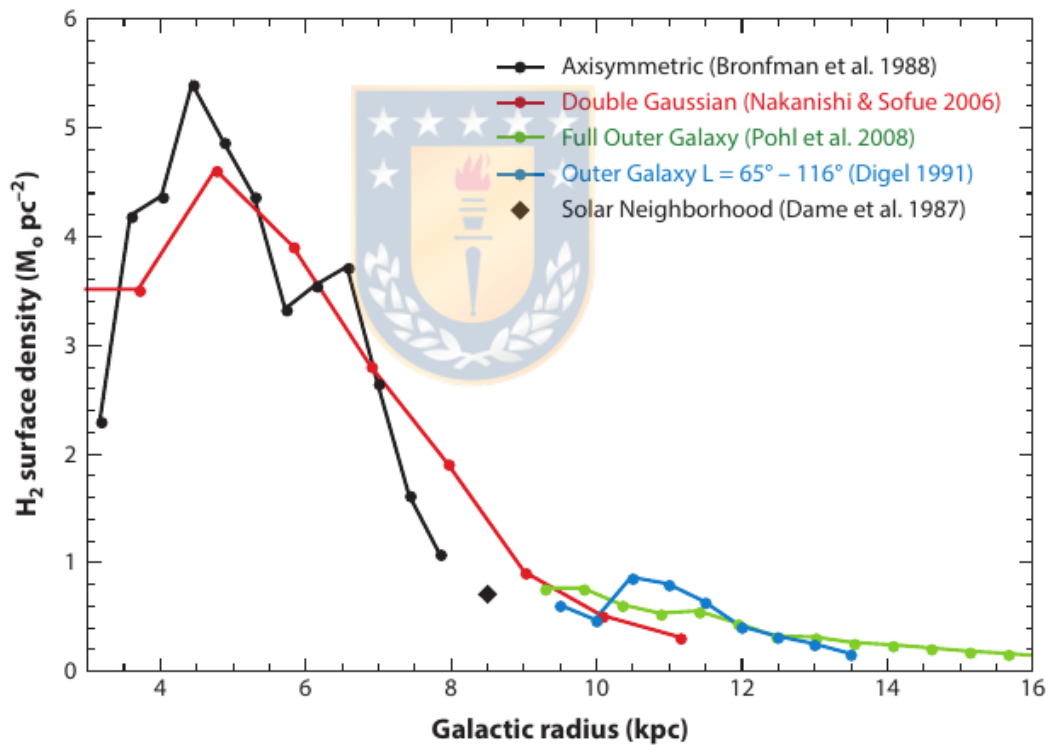


Figure 2.1.5: The H_2 mass surface density as a function of Galactic radius Credits. Image from Heyer and Dame (2015)

Molecular clouds (dust observation of Orion A 2.1.6) are formed primarily of hydrogen arranged in molecules consisting of two atoms: H_2 . Unfortunately for astronomers, hydrogen molecules are notoriously secretive. They do not interact with light in the visible part of the spectrum making them invisible to optical telescopes. In fact, under the conditions inside a molecular cloud. they don not emit or absorb much radiation at all, even in other regions of the electromagnetic

spectrum. However, as explained in the past section, the main tracer for this structures is the CO molecule.



Figure 2.1.6: The Orion A Molecular Cloud. The image is a composite of the wavelengths of 70 microns (blue), 160 microns (green) and 250 microns (red) and spans about 2.4×1.3 degrees. North is to the left and east is up. Credit: [Orion A](#) ESA/Herschel/Ph. André, D. Polychroni, A. Roy, V. Könyves, N. Schneider for the Gould Belt survey Key Programme

2.1.3 Molecular Filaments

Throughout the Milky Way, molecular clouds typically appear filamentary, and mounting evidence indicates that this morphology plays an important role in star formation process [Ragan et al. \(2014\)](#), [Palmeirim et al. \(2013\)](#) and many others authors consider this. Molecular filaments are very long structures of molecular gas with sizes ranging from 10 - 30 pc or more, e.g., giant molecular filament (GMF) found in M33 is approximately $\sim 50 - 70$ pcs in length, $\sim 5 - 6$ pcs in width (K. Tokuda et al 2019) and with $\sim 10^5 M_{\odot}$, or the seven GMF samples from [Ragan et al. \(2014\)](#) with lengths on the order of ~ 100 pc, total masses of $10^4 - 10^5 M_{\odot}$ and located in the first quadrant of the Milky Way galaxy.

Detailed studies of massive filaments and of their internal structure and dynamics are crucial to better understand the link between high-mass star formation and

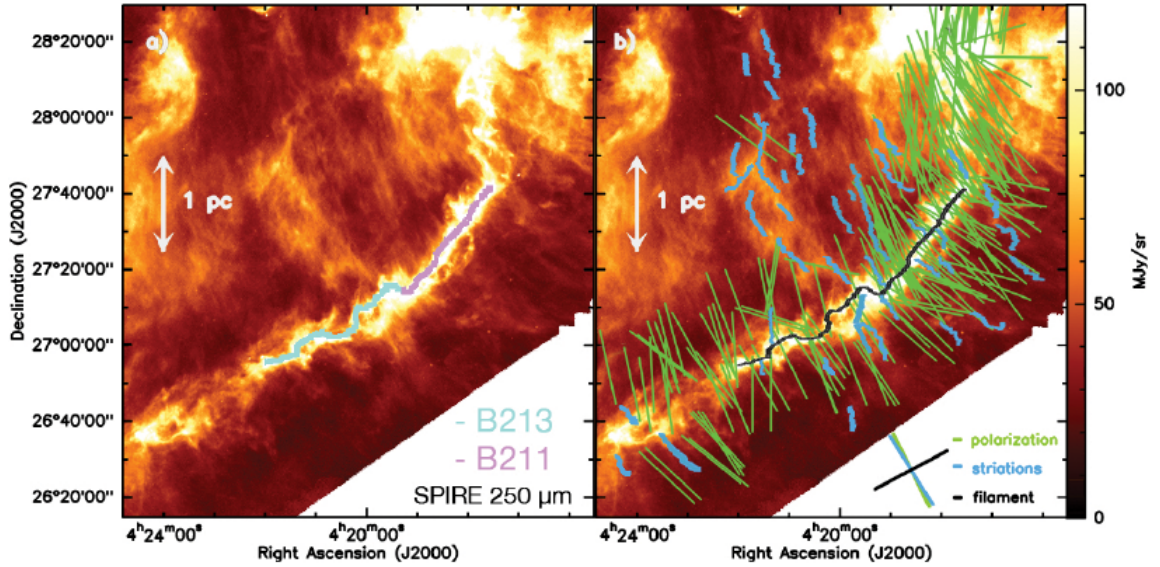


Figure 2.1.7: **Left:** Herschel/SPIRE 250 μm image of B211/B213 presented in light blue and purple respectively. **Right:** Display of optical and infrared polarization vectors from Heyer et al. (2008), Heiles (2000), and Chapman et al. (2011) tracing the magnetic field orientation in the B211/L1495 region, The green, blue, and black segments in the lower right corner represent the average position angles of the polarization vectors, low-density striations (structures perpendicular to the main filament), and B211 filament, respectively. Credits: [Palmeirim et al. \(2013\)](#)

cloud and cluster formation. Thanks to APEX Telescope Large Area survey of the Galaxy (ATLASGAL) [Schuller et al. \(2009\)](#) and the Herschel infrared Galactic Plane Survey (Hi-GAL) [Molinari et al. \(2010\)](#), have allowed for the compilation of catalogs of candidates filaments over the entire plane. These studies have shown that massive filaments are in general a few kiloparsec distant from us ([Leurini et al. \(2019\)](#) and reference therein). Moreover, the Herschel Gould Belt Survey [André et al. \(2010\)](#) produced excellent data to study nearby (150 to 700 pc) molecular filaments.

Additionally, molecular filaments present a typical width of ~ 0.1 pc, basing on the studies in [Arzoumanian et al. \(2011\)](#) where found that IC 5146, Aquila and Polaris molecular filaments are all characterized by a typical width of ~ 0.1 pc, suggesting that most of the interstellar filaments may share a similar characteristic width of ~ 0.1 pc, i.g., the work of [Palmeirim et al. \(2013\)](#) focused in Taurus B211/B213 filaments (located in the Taurus molecular cloud at a distance of

~ 150 pc) measured a width of ~ 0.1 pc (figure 2.1.7).

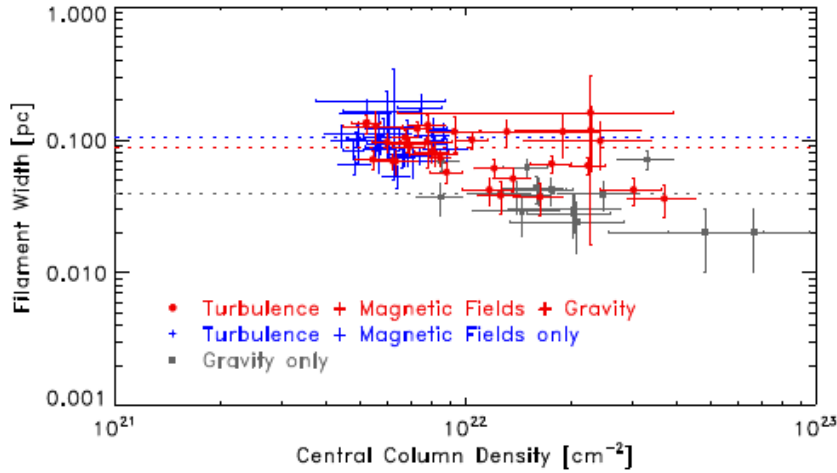


Figure 2.1.8: Filament width in function of column density for 3 different simulations in Federrath (2016). the horizontal dotted lines show the average filament width.

Moreover, in the work in Federrath (2016), where he performed three-dimensional high-resolution magneto-hydro-dynamical simulations that followed the evolution of molecular clouds and the formation of filaments and stars to understand the universality of interstellar filaments, obtained a universal filament width of 0.1 ± 0.02 pc. Figure 2.1.8 shows the width and column density values for different simulations made in Federrath (2016) where he considered a combination of different physical ingredients: gravity, turbulence, magnetic fields and jet/outflow feedback. Also, he observed that star formation activity does not affect the width of filaments and even more incredible is that when smoothing the simulation maps that he found to the Herschel SPIRE resolution obtained in Arzoumanian et al. (2011), he still found a filament width that is statistically indistinguishable from what he obtained with the full simulation resolution.

2.1.4 Mass to Magnetic Flux Ratio

Merely measuring the magnetic field strength does not allow us to determine immediately the importance of the magnetic field in a given star-forming region. Therefore, in magnetic field studies it is common to compare the magnetic energy density with that of other dynamical quantities such as gravity, velocity fields, turbulence, and outflow feedback. Magnetic field generally opposes collapse in molecular clouds, the common quantity quoted as a metric for the importance of

the magnetic field with respect to gravity is the *mass-to-flux ratio* M/Φ , where M is the mass of the object of interest and Φ is the flux of the magnetic field threading the object.

The resumed derivation [Krumholz \(2015\)](#) comes from the virial term for magnetic support and gravity inside a spherical molecular clouds, that is,

$$\mathcal{B} = \frac{\Phi_B^2}{6\pi^2 R} \quad \text{and} \quad \mathcal{W} = -\frac{3GM^2}{5R} \quad (2.1.1)$$

Where R is the radius of a uniform spherical cloud threaded by a magnetic field \mathbf{B} and M is the mass of the cloud. Then, comparing these two terms, it is found that

$$\mathcal{B} + \mathcal{W} = \frac{\Phi_B^2}{6\pi^2 R} - \frac{3GM^2}{5R} \equiv \frac{3G}{5G}(M_\Phi^2 - M^2) \quad (2.1.2)$$

where

$$M_\Phi = \sqrt{\frac{5}{2}} \left(\frac{\Phi_B}{3\pi\sqrt{G}} \right) \quad (2.1.3)$$

is defined as the magnetic critical mass. Since Φ_B does not change as a cloud expands or contracts (due to flux-freezing), this magnetic critical mass does not change either.

The implication of this is that clouds that have $M > M_\Phi$ always have $\mathcal{B} + \mathcal{W} < 0$. The magnetic force is unable to halt collapse no matter what. Clouds that satisfy this condition are called magnetically supercritical, because they are above the magnetic critical mass M_Φ . Conversely, if $M < M_\Phi$, then $\mathcal{B} + \mathcal{W} > 0$, and gravity is weaker than magnetism. Clouds satisfying this condition are called sub-critical.

For a sub-critical cloud, since $\mathcal{B} + \mathcal{W} \propto 1/R$, this term will get larger and larger as the cloud shrinks. In other words, not only is the magnetic force resisting collapse is stronger than gravity, it becomes larger and larger without limit as the cloud is compressed to a smaller radius. Unless the external pressure is also able to increase without limit, which is nonphysical, then there is no way to make a magnetically sub-critical cloud collapse. It will always stabilize at some finite radius. The only way to get around this is to change the magnetic critical mass,

which requires changing the magnetic flux through the cloud. This is possible only via ion-neutral drift or some other non-ideal Magneto-Hydro-Dynamic effect that violates flux-freezing.

However, it is more useful to discuss the dynamical status of an object by measuring the ratio λ of the observed mass-to-flux ratio to the critical mass-to-flux ratio:

$$\lambda = \frac{(M/\Phi)_{obs}}{(M/\Phi)_{crit}} \quad (2.1.4)$$

Clouds that are supported by the magnetic field and are not collapsing are deemed sub-critical ($\lambda < 1$), whereas those where gravity has overcome the resistance of the magnetic field are referred to as super-critical ($\lambda > 1$).

The measurement of this parameter is crucial to prove two extreme models of star formation, one is the strong field model (e.g., Mouschovias and Morton (1991), Mouschovias and Ciolek (1999)), which says that magnetic fields control the formation and evolution of the molecular clouds from which stars form, including the formation of cores and their gravitational collapse to form proto-stars. the other one is the weak field model (e.g., Padoan and Nordlund (1999), Mac Low and Klessen (2004)), which says that molecular clouds are intermittent phenomena, with short ($\sim 10^6$ yr) lifetimes. In this model, clouds form at the intersection of turbulent supersonic flows in the interstellar medium. Generally, clouds do not become gravitationally bound, and they dissipate. Star formation occurs only in the small fraction of the molecular gas that is sufficiently dense to be self-gravitating Elmegreen (2000). Magnetic fields may be present in this theory, but they are too weak to be energetically important. So, observational tests that do not unambiguously distinguish between the extreme cases may suggest that the more complex theories that include both physically important turbulence and magnetic fields may be favored.

So, if M/Φ is observed to be supercritical, particularly at lower densities, the magnetic support model is not viable. On the other hand, if it is observed to be sub-critical, magnetic fields would be too strong for the intermittent, turbulent theory to hold. The M/Φ parameter provides in principle a direct, simple, and definitive test to discriminate between the two theories of star formation.

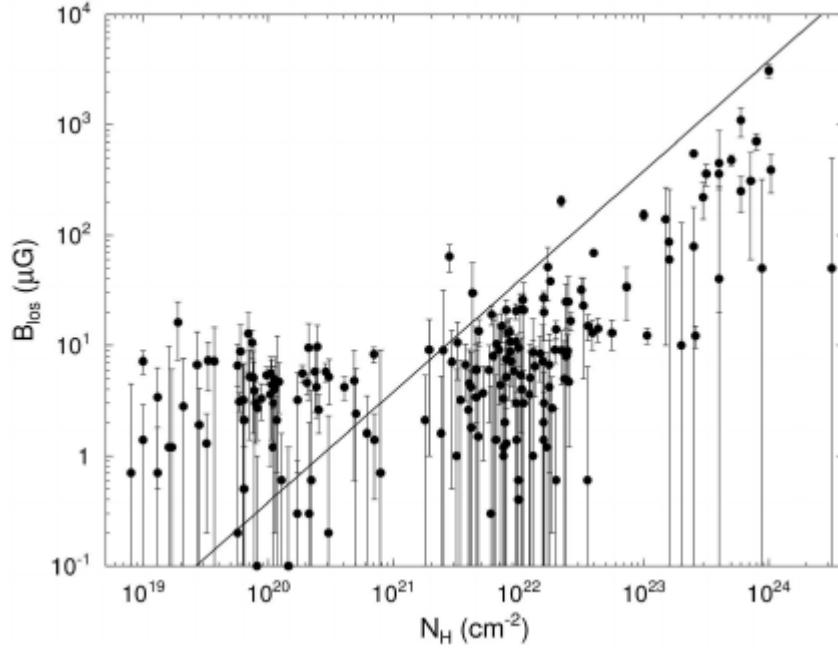


Figure 2.1.9: Dots above the line are sub-critical and below are super-critical. Image credits [Crutcher and Kemball \(2019\)](#).

Measurement of the mass to flux ratio in atomic and molecular clouds, e.g., [Crutcher et al. \(1999\)](#), [Troland and Crutcher \(2008\)](#) or [Falgarone et al. \(2008\)](#) have shown that the atomic clouds show a mass to flux ratio sub-critical and molecular clouds a super-critical one. Figure 2.1.9 shows HI, OH, and CN Zeeman measurements of B_{LOS} vs. $N_{\text{H1}} = N_{\text{HI}} + 2N_{\text{H}_2}$. The straight line is for a critical $M/\Phi = 3.8 \times 10^{-21} N_{\text{H}}/B$. Measurements above this line are sub-critical, those below are super-critical. Measurements of both HI and OH in star forming regions and atomic clouds are crucial for the understanding of these theories because both lines characterize the low and intermediate density medium and different ISM phases. Additionally, they can be observed with one unique L-band dual-polarization feed system.

2.2 Magnetic Field Diagnostic Tools

It is impossible to measure directly the magnetic field \mathbf{B} of celestial objects in situ, except on the surface and in the vicinity of the Earth and in very limited regions in the Solar System. Nevertheless, radiation from planets, stars, galaxies, galaxy clusters, and the cosmic microwave background (CMB) can be observed,

and, diagnose \mathbf{B} by looking at magnetic effects on the generation and propagation of radiation. There are essentially six different tracers of magnetic fields in a diffuse astrophysical medium:

- Dust grain polarization, caused by dust grains whose magnetic moments align along the magnetic field
- Synchrotron radiation, bearing information about the total strength of the magnetic field. Its linearly polarized component measures the strength and orientation of the ordered or uniform component of the magnetic field perpendicular to the line of sight.
- Faraday rotation, yielding information about the line-of-sight component of the magnetic field and its direction.
- Goldreich-Kylafis effect (method), causes certain molecular line emission (also absorption) to be weakly linearly polarized, e.g., in the presence of a magnetic field.
- David-Chandrasekhar-Fermi method uses the fact that turbulent motions should cause an observable scatter in what would otherwise be a well ordered mean magnetic field. The original, simplest form of the DCF formula yields an estimate of the plane-of-sky magnetic field strength.
- The Zeeman effect, yielding information about strong magnetic fields in dense gas clouds and about their direction. Thanks to this method it is possible to know magnitude and direction of the line-of-sight magnetic field component in star formation regions, i.e., molecular clouds and dense cores.

Among this six diagnostic tools, the Zeeman effect, is the only direct method capable to characterize the strength and direction of magnetic fields in both atomic and molecular interstellar medium. This makes the Zeeman effect the perfect option to characterize the magnetic field in regions with different size scales and densities. The Zeeman effect is the key to study the influence of magnetic fields in star formation regions. Sections below describe the mentioned magnetic field diagnostic tools and emphasize on the Zeeman effect.

2.2.1 Dust Grain Polarization

The alignment of dust grains in the galactic magnetic field naturally also leads to polarization of their continuum radiation, observed in the mm, sub-mm, or far-infrared regime. This method only gives the orientation of the plane-of-sky magnetic field component and not the strength, so, with this tool it can only be obtained information about the morphology of the magnetic field for structures obscured by dust. Figure 2.2.1 shows the orientation of many starlight polarization, which is basically the un-polarized emission of stars that enters to a dust cloud pervaded with magnetic fields and observing this dust re-emission, is possible to obtain the orientation of the magnetic field (measuring the angle of polarization). Also dust by itself emits thermal polarized emission and is this emission that is also observed and analyzed in molecular structures to disentangle information about the magnetic fields morphology.

2.2.2 Synchrotron Radiation

Synchrotron radiation is the main diagnostic tool to trace \mathbf{B} in the ISM and IGM (Inter Galactic Medium). It is produced by the relativistic electrons that have been energized in the turbulent ISM and IGM via shock waves, notably caused by supernova explosions in the former case, and by active galactic nuclei (AGN), by galactic wakes and by merging of galaxy clusters in the latter. While moving at relativistic speeds, the particles are subject to the Lorentz force, which forces them into helical paths. The corresponding acceleration makes them radiate synchrotron radiation, which has a characteristic frequency spectrum and is partially polarized. However for the study of Synchrotron is necessary the production of relativistic particles, but, this are null observed in HI regions or Molecular clouds, so, the study of this tools is not in the consideration of the project.

2.2.3 Rotation Measure (Faraday Effect)

Faraday effect happens when a linearly polarized radiation enters to a plasma regions, in this case the ISM, and when in contact with this plasma, the linear polarization angle is rotated a certain angle. This angle rotation is related with the plasma properties and also with the component of the interstellar magnetic field in the direction of propagation. Above is presented how this parameters are

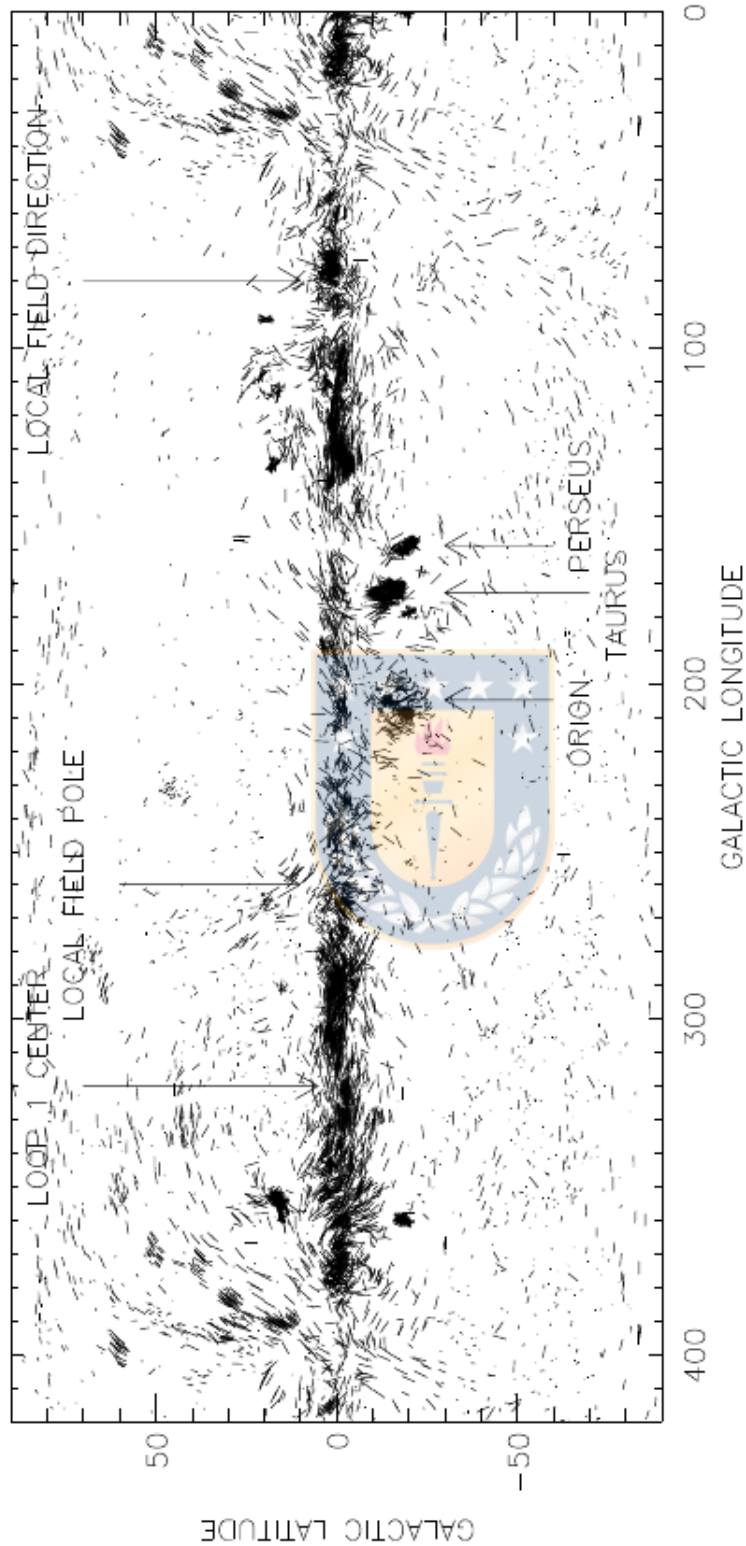


Figure 2.2.1: Starlight polarization of 8662 stars. The orientation of each star's polarization is indicated by a short line whose length L in great-circle degrees is $L = [4 < 2P]^\circ$, where P is the percentage polarization; for L , is plotted whichever of the two quantities is smaller. Image from [Heiles and Crutcher \(2005\)](#).

related each other,

$$\Delta\chi = \chi_0 + \phi\lambda^2 \quad (2.2.1)$$

where χ_0 is the linear polarization angle before enter to the plasma, λ is the wavelength and,

$$\phi = \frac{e^3}{8\pi^2\epsilon_0 m^2 c^3} \int_0^d n_e(s) B_{\parallel} ds \quad (2.2.2)$$

is the Rotation measure (sometimes referred as Faraday depth) and e is the charge of the electron, m is the mass of the electron, c is the speed of light, n is the density of electrons at each point s along the path and \mathbf{B}_{\parallel} is the component of the interstellar magnetic field in the direction of propagation at each point s along the path.

2.2.4 Goldreich-Kylafis Effect

Polarization of molecular-line emission is another tracer of the magnetic field in star-forming regions. Molecular and atomic lines are sensitive to magnetic fields, which cause their spectral levels to split into magnetic sub-levels. For some molecules, linear polarization can arise when an anisotropy in the radiation and/or velocity field yields a population of magnetic sub-levels that are not in local thermodynamic equilibrium (LTE); this is known as the Goldreich-Kylafis effect (1981).

The effect is strongest in the lowest rotational transitions of simple molecules such as CO, CS, HCN, SiO, or HCO⁺. Spectral-line polarization from the G-K effect can be parallel or perpendicular to the magnetic field. Due to the different optical depths of the parallel and perpendicularly polarized components in different locations on the sky, polarization from the G-K effect ultimately traces the plane-of-sky magnetic field orientation with an ambiguity of 90°.

The G-K effect is a powerful way to trace the magnetic field in regions where the brightness of the thermal dust emission is too low to detect polarization at the

few- percent level, either because the source is too distant or because the column density of dust is too low [Hull and Zhang \(2019\)](#).

2.2.5 Davis-Chandrasekhar-Fermi Method

In the early days of interstellar polarization studies, Chandrasekhar & Fermi (1953) suggested that analysis of the small-scale randomness of magnetic field lines could yield estimates of the field strengths. This method suggest that turbulent motions will lead to irregular magnetic fields [Crutcher \(2012\)](#). This method use as basis the Alfven's theorem or Alfven's frozen-in theorem, which says that under very cold temperatures the magnetic fields is frozen into the fluid and has to move along with it. At interstellar scales of temperature, molecular clouds are very cold (20 - 50 K), so, is possible to assume these conditions of magnetic field been frozen into the matter and flow. Also, to use this method is necessary four assumptions within the molecular cloud:

- There is a mean magnetic field
- The turbulence is in-compressible
- The turbulence is isotropic
- There is equipartition between turbulent and magnetic energy

With this four assumptions they showed that is possible to measure the magnitude of the plane-of-sky magnetic field component.

The method is as follows: Using the phase velocity of transverse Alfvén wave, $V_A = B/(4\phi\rho)^{1/2}$, the wave is described as:

$$y = A \cos[k(x - V_A t)] \quad (2.2.3)$$

where y is a displacement in the plane of the sky and perpendicular to the mean magnetic field. This gives:

$$V_A^2 \overline{\left(\frac{\partial y}{\partial x}\right)^2} = \overline{\left(\frac{\partial y}{\partial t}\right)^2} \quad (2.2.4)$$

where \overline{X} represents the time average. The rhs of the equation, which is the one-

dimensional velocity dispersion in y direction, seems to be equal to the velocity dispersion in the line-of-sight ΔV as:

$$\overline{\left(\frac{\partial y}{\partial t}\right)^2} = \Delta V^2 \quad (2.2.5)$$

The lhs of the equation is given with a dispersion of polarization direction $\Delta\phi$ (rad)

$$\overline{\left(\frac{\partial y}{\partial x}\right)^2} = \Delta\phi^2 \quad (2.2.6)$$

in which the lhs is measured by the wave-pattern of the Alfvén wave. Therefore, the magnetic field strength is given as:

$$B_{\perp} = (4\pi\rho)^{1/2} \frac{\Delta V}{\Delta\phi} \quad (2.2.7)$$

Applying the same method to the molecular cloud, Crutcher in [Crutcher et al. \(2004\)](#) obtained the magnetic field strength in the plane of the sky in three pre-stellar clouds as $\simeq 80\mu\text{G}$ (L183), $\simeq 140\mu\text{G}$ (L1544), and $\simeq 160\mu\text{G}$ (L43).

2.2.6 Zeeman Effect

The Zeeman effect is considered by many authors the only tool that provides direct measurements of magnitude and direction of magnetic fields in the galactic and extra-galactic interstellar medium, but most specific in molecular gas clouds [Crutcher and Kemball \(2019\)](#), [Crutcher et al. \(1993\)](#), [Troland and Crutcher \(2008\)](#).

2.2.6.1 Brief Historical Background

The Zeeman effect was discovered by Dutch physicist *Pieter Zeeman* in 1896 in a laboratory experiment. In his discovery paper, P. Zeeman suggested that the effect he had discovered could be important in measuring magnetic fields in astrophysics. Bolton & Wild (1957) worked on the possibility of measuring interstellar magnetic fields by the 21-cm Zeeman splitting, based on the measurement in Nafe & Nelson (1948) that, in the presence of a weak magnetic field, the 21-cm line is split into three components of frequency:

$$\begin{aligned}\nu_0 &= 1420.4058 \text{ MHz} \quad (\pi) \\ \nu_0 \pm \mu_B B/h &= 1.4 \text{ Hz}/\mu\text{G} \quad (\pm\sigma)\end{aligned}\tag{2.2.8}$$

Where π is the unshifted component linearly polarized along the field direction and $\pm\sigma$ components appear circularly polarized shifted relative to the π component.

The first indication of an interstellar Zeeman effect came from observations of polarization in OH masers (Microwave Amplification by Stimulated Emission of Radiation) by Weinreb et al. in 1965; although they suggested that the polarization might be due to the Zeeman effect, that interpretation was not certain because the standard pattern of the classical Zeeman effect was not seen in the polarized maser emission. Following intense observational work by several workers, *Gerrit L. Verschuur* (1968) (figure 2.2.2) first detected the Zeeman effect in the extended interstellar medium in the 21 cm hyper-fine line of HI. This discovery was of cardinal importance to directly prove the existence of magnetic fields in the ISM. However, the problem is that the splitting of the lines in frequency is very small, i.e., a few Hertz per micro-Gauss, nevertheless, astronomers found that the circular polarized intensity, represented by the Stokes V parameter, is proportional to the splitting and the line-of-sight magnetic field component and direction.

2.2.7 The Effect

Splitting of spectral lines into several component lines, each differing slightly in frequency, in the presence of an external magnetic field is called the Zeeman effect. The magnitude of the energy shift is directly proportional to the strength of the magnetic field. The resulting frequency shift is

$$\Delta\nu_z = \pm \frac{g\mu_B B}{h}\tag{2.2.9}$$

where g is the Landé g -factor, μ_B is the Bohr magneton, and h is Planck's constant. It was discovered in 1896 by Dutch physicist Pieter Zeeman in a laboratory experiment. In his discovery paper, P. Zeeman suggested that the effect he had discovered could be important in measuring magnetic fields in astrophysics. Bolton & Wild (1957) worked on the possibility of measuring interstellar magnetic fields using the 21-cm Zeeman splitting, based on the measurement in Nafe &

Nelson (1948) that, in the presence of a weak magnetic field, the 21-cm line is split into three components of frequency:

$$\begin{aligned}\nu_0 &= 1420.4058 \text{ MHz} \quad (\pi) \\ \nu_0 \pm \mu_B B/h &= 1.4 \text{ Hz}/\mu\text{G} \quad (\pm\sigma)\end{aligned}\tag{2.2.10}$$

Where π is the unshifted component linearly polarized along the field direction and $\pm\sigma$ components appear circularly polarized shifted relative to the π component.

The Zeeman effect is not readily visible in all molecular species: only those with an unpaired electron will exhibit strong Zeeman splitting. For species without an unpaired electron, the Bohr magneton in equation 2.2.9 must be replaced by the nuclear magneton. Since the magneton is inversely proportional to the mass of the particle, the nuclear magneton is about three orders of magnitude smaller than the Bohr magneton. Therefore, the Zeeman frequency splitting is approximately 1800 times smaller for species without an unpaired electron. This limits species available for Zeeman effect observations, and thus far only the 21 cm line of HI, the 18 cm, 6 cm, 5 cm, and 2 cm lines of OH, the 3 mm hyperfine lines of CN, and the 1.3 cm H₂O maser line have been successfully used for magnetic field observations. Note that the H₂O maser line does not have an unpaired electron, but has been a successful probe of strong magnetic fields in maser regions due its strong line strengths McMullin et al. (2007).

The Zeeman effect is the only tool that provides direct measurements of magnitude and direction of magnetic fields in the ISM, i.e., stars, molecular clouds, filaments, gas clumps, cores and possibly in proto-planetary disks.

Section 2.2.6 will continue with the explanation of Zeeman effect showing how it is possible to relate this effect with Stokes V parameter to measure the magnitude and direction of the line-of-sight magnetic field and results of single-dish and interferometric observations.

2.2.8 Measuring Magnetic Fields With the Zeeman Effect

It was presented in section 2.2 the different diagnostic tools for the characterization of galactic and extra-galactic magnetic fields. These diagnostic tools depend on different astrophysical effects in the medium and the incoming electromagnetic

POSITIVE DETERMINATION OF AN INTERSTELLAR MAGNETIC FIELD BY MEASUREMENT
OF THE ZEEMAN SPLITTING OF THE 21-cm HYDROGEN LINE



G. L. Verschuur
National Radio Astronomy Observatory,* Green Bank, West Virginia
(Received 17 July 1968)



Fields of the order of 2×10^{-5} G exist in the Perseus spiral arm in the direction of the radio source Cassiopeia A.

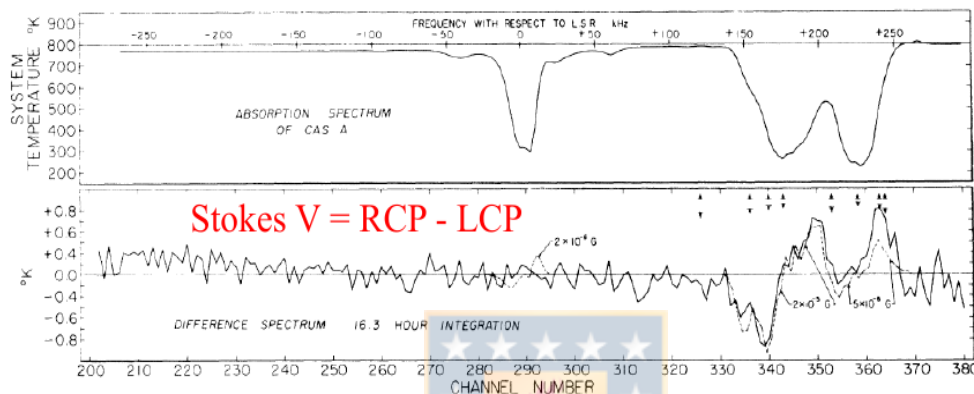


FIG. 1. The absorption spectrum of Cas A, together with the difference spectrum, right-hand minus left-hand polarization, incident on the feed representing 16.3 h of integration. Frequencies with respect to the local standard of rest are indicated. Arrowed bars represent expected peak-to-peak noise at various parts of the spectrum.

Figure 2.2.2: Spectrum detected by Verschuur (1968). Credits: [T. Robishaw](#), Zeeman splitting opportunities with the ngVLA - NRAO (2017)

wave. However, all these diagnostic tools measure the magnetic fields by detecting the polarization state of the electromagnetic waves. To understand it, it was necessary to research the different concepts of polarization and how radio-polarimeters works in single-dish and interferometers. Appendix [A2](#) and [A3](#) explains the concepts of polarization and radio-polarimetry, respectively. All of this was necessary to understand how Zeeman effect observations are carried out.

Zeeman effect is a quantum regime effect which affects the electron properties i.e. quantum numbers and basically is due to a B-field that splits one energy level into two or more, producing a circular polarized emission. The way that astronomers measure **B** strength and direction is thanks to this circular polarized emission, the difference of both sense of circular polarization i.e. Right CP minus Left CP is equal to the Stokes V parameter, which characterizes the quantity of circular polarization intensity (this can be negative or positive) and this parameter is proportional to the **B** strength. However, in the extended (non-masing) interstellar medium, the Zeeman splitting is generally much smaller than the line width, and

it is only possible to measure the magnitude and direction of the line-of-sight component B_{LOS} of \mathbf{B} . Moreover, only the molecules with unpaired electrons (paramagnetism) poses a more strong Zeeman frequency shift. However, Zeeman effect provides the only direct method for measuring \mathbf{B} strengths and direction in molecular clouds. In table 2.2.1 is presented the values of Z for different species, where Z is named Zeeman factor and it is different for each specie, also, this factor is frequency independent.

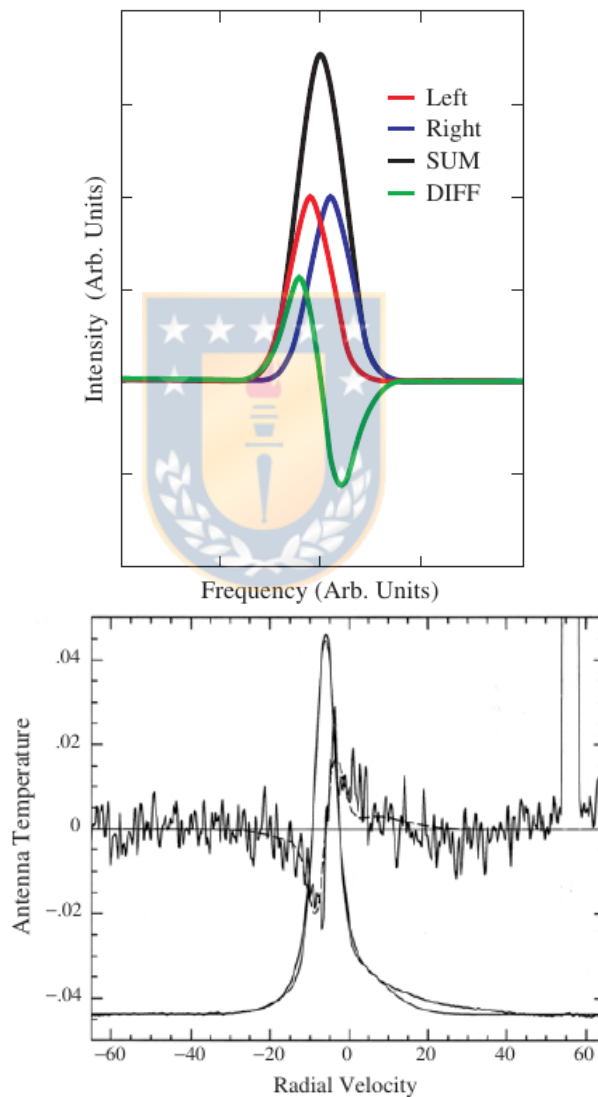


Figure 2.2.3: Zeeman effect for neutral Hydrogen: ideal and real Zeeman spectral line profile from Heiles (1989).

Equations below 2.2.11 from Crutcher et al. (1993) show the relation between polarization (Stokes parameter), radio polarimetry (sum and difference between correlated products) and Zeeman effect, i.e., magnetic field. Notice the second

Species	Transition	Frequency [GHz]	Z [Hz/ μ G]
HI	F = 1-2	1.42	2.8
OH	J = 3/2, F= 1-1	1.665	3.27
	J = 3/2, F= 2-2	1.667	1.96
	J = 3/2, F= 2-1	1.72	1.31
CN	J = 1/2 - 1/2, F = 1/2 - 3/2	113.14	2.18
H ₂ O	F = 6 ₁₆ - 5 ₂₃	22.23	0.003
CH ₃ OH	J _N = 5 ₁ - 6 ₀	6.668	-0.00114

Table 2.2.1: Most used lines in Zeeman observations. $Z = 2\Delta\nu_z$. For the full table see Crutcher & Kemball (2019) [Crutcher and Kemball \(2019\)](#)

order spectral derivative dependence of Stokes Q and U, which reduces the signal amplitude even more than in the Stokes V parameter. It is because of this that is difficult or impossible to measure these two Stokes parameters which are related with the other components of the magnetic field.

$$\begin{aligned}
 I &= RR + LL = XX + YY \\
 V &= RR - LL = XY - YX \propto \frac{dI}{d\nu} Z B \cos\theta \\
 Q &= RL + LR = XX - YY \propto -1/4d^2 I / d\nu^2 Z B (\cos\phi - \sin\phi) \\
 U &= LR - RL = XY + YX \propto -1/4d^2 I / d\nu^2 Z B \sin\phi
 \end{aligned} \tag{2.2.11}$$

where θ is the angle between the B_{los} and B and ϕ is the position angle of the component of the B-field in the plane of the sky (B_{pos}). So in conclusion, due to the second order derivative dependence of Stokes Q and U, is quite difficult to obtain the total B-field. Is important to clarify that the final relations of equation 2.2.11 depend on the shape of Stokes I spectrum and also are used to fit into the real detected spectrum. The shape of Stokes I and then the capability to obtain Stokes V and measure B_{los} , depend of a few parameters. In [Brauer et al. \(2017\)](#) they analyzed turbulence velocity, gas density, gas temperature, \mathbf{B} and velocity fields to see how this parameters affect the Zeeman analysis method. They found that the uncertainty of the analysis method increases, if both the gas velocity and \mathbf{B} show significant variations along the line of sight and the density has almost no impact on the uncertainty of the analysis method, unless it reaches values than those typically found in molecular clouds ($n_H \gg 10^7 \text{cm}^{-3}$).

The measurement of Zeeman splitting in spectral lines-both in emission and

absorption can provide direct estimates of the magnetic field strength and direction in atomic and molecular clouds, both in our own Milky Way and in external galaxies. This method will probe the magnetic field in the warm and cold neutral components of the interstellar medium.

2.2.9 HI and OH Zeeman Effect Observational Results

A good review where is possible to find chronological information about Zeeman effect observations is in [Crutcher and Kemball \(2019\)](#) were authors summarized the state of Zeeman effect observational results in star forming regions. Through the years, the most observed lines are the 21-cm line of HI, the 18-cm, 6-cm, 5-cm and 2-cm Λ – doublet lines of OH molecule and the 3-mm $N = 1 \rightarrow 0$ lines of CN molecule. Exception are the 1.3-cm H₂O maser line, due to very strong line strengths and strong fields in H₂O maser region and the 4.5-cm CH₃OH molecular line. Also, other promising species are C₂H, SO, C₂S, C₄H, CH and CH⁺ [Troland and Crutcher \(2008\)](#).

The three species with Zeeman detections (excluding masers) do make it possible to measure B_{los} over the wide range of densities in the ISM from diffuse HI clouds to molecular cores. HI in emission samples both the warm neutral and the cold neutral diffuse medium, with densities ranging roughly from 1 to 100 cm^{-3} . HI in absorption toward molecular clouds can sample densities of $\approx 10^2 - 10^4 cm^{-3}$, about the same densities that the ground-state 18-cm lines of OH sample. Finally, with a critical density of $\approx 10^6 cm^{-3}$, the 3-mm lines of CN in emission samples densities of $\approx 10^5 - 10^6 cm^{-3}$. Observations of this atomic and molecular lines are presented in figure [2.2.4](#).

Zeeman splitting of the 21-cm line observations presented by Heiles in [Heiles \(1997\)](#) is considered as a "smoking gun" in Orion A filament (the largest nearby star-forming such structure) by [Stutz and Gould \(2016\)](#). This work showed that this structures are enveloped in a helical magnetic field, which would be generated primarily by currents moving along the filaments. Figure [2.2.5](#) shows the results of 217 position observations in a $\sim 200deg^2$ in the Orion/Barnard loop region using the 26 m telescope of the Hat Creek Radio Observatory.

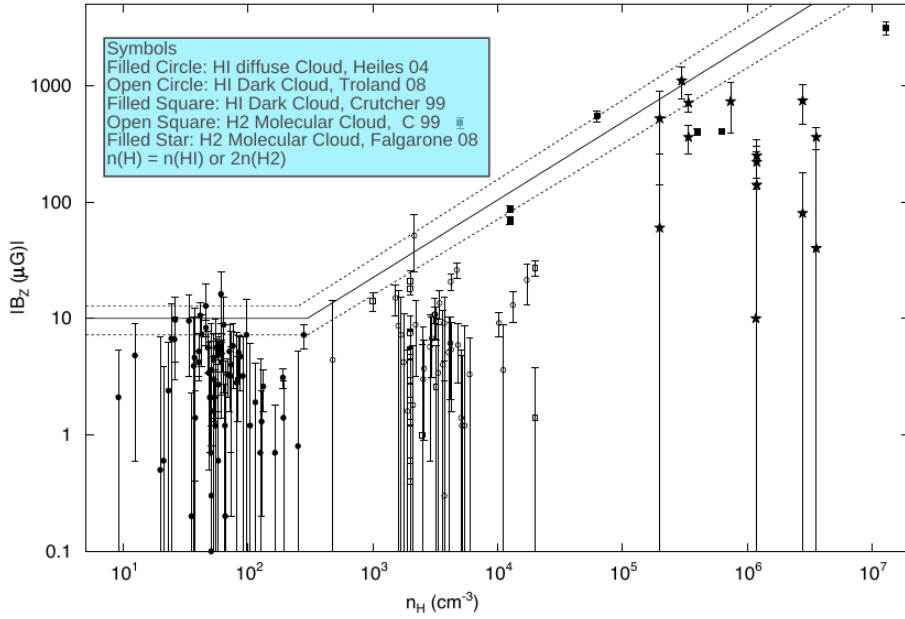


Figure 2.2.4: B_z or B_{los} from different regions in the Milky Way in function of the volume density, where $n(\text{HI})$ is the density of HI and $2n(\text{H}_2)$ is the volume density of molecular Hydrogen. Notice how B_z is approximately constant from 1 to 100 cm^{-3} densities and evolve exponentially as $B_z \propto n^{2/3}$ for higher densities and elements. Image from [Crutcher et al. \(2010\)](#). Legend for this work.

2.2.9.1 Interferometric Observations of Magnetic Fields

The first millimeter interferometric observation with the purpose to measure magnetic fields within the ISM was made by the BIMA (Berkeley-Illinois-Maryland Association), now, the observation of dust polarization are leading the interferometric observation of polarization in proto-planetary disk observation [Hull and Zhang \(2019\)](#), however, Zeeman effect observation in this regions are starting to grow up.

The number of interferometric observations for Zeeman effect are very low and the answer could be that single dish results are quite good, however, moving to small structures i.e. filaments, clumps, cores, and proto-stellar disk systems, the resolving power decays and the time dependence increases because the integration time for Zeeman observations are high. In [Troland and Crutcher \(2008\)](#) required ~ 500 hours of observation with the Arecibo telescope to complete an extensive survey of magnetic fields strengths toward 34 dark cloud cores in order to test models of star formation.

In figure [2.2.6](#) is presented a VLA cycle-a observation of Zeeman effect towards

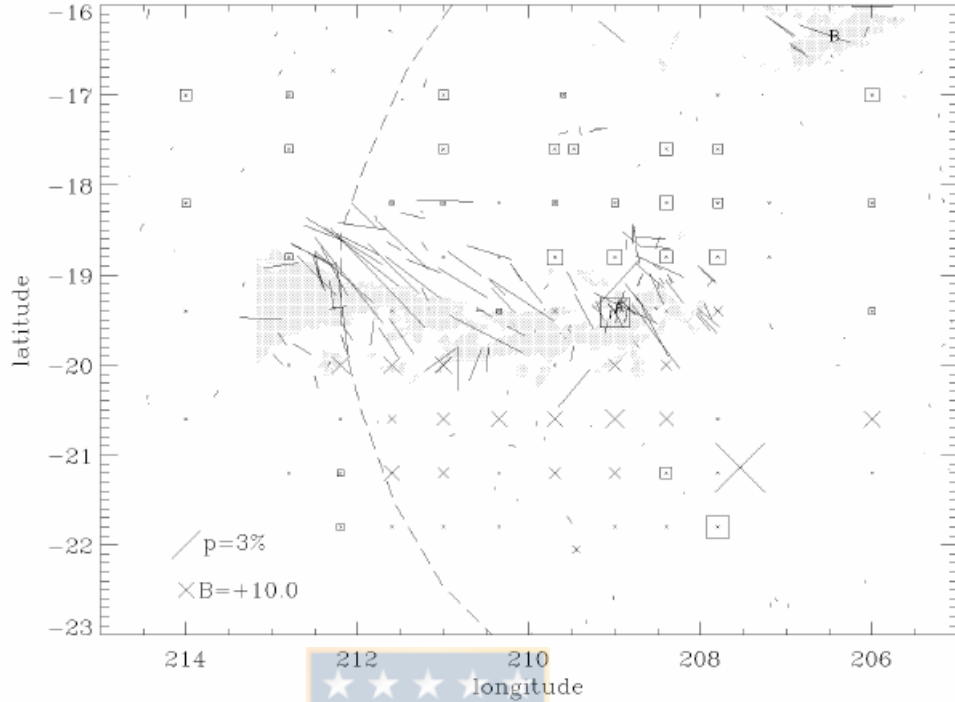


Figure 2.2.5: Zeeman-splitting detections for the line-of-sight magnetic field component in the Orion/Barnard Loop. Positive fields are represented by crosses and negative fields by squares. The lines are stellar polarization data, references within Heiles (1997). Image from Heiles (1997).

NGC2024 (Orion B) made by Crutcher (1999) Crutcher et al. (1999). The absorption spectrum of this image is at the position of the peak in the line-of-sight magnetic field. This peak B_{LOS} position is $\alpha(1950) = 05^{\text{h}}39^{\text{m}}09^{\text{s}}$ and $\delta(1950) = -01^{\circ}56'30''$. The right image shows how B_{LOS} varies from 0 to the northeast of the northern molecular ridge to almost $100 \mu\text{G}$ to the southwest. A published map of linearly polarized dust emission shows a relative minimum in percentage polarization near the B_{LOS} maximum, which suggests that the variation in B_{LOS} may be due to the field being mainly in the plane of the sky to the northeast but having a significant line-of-sight component to the southwest. Moreover, in this study it was also observed HI at absorption, observing that the magnitude of B_{LOS} mapped in HI was lower than in OH, but the morphologies of the field mapped in OH and HI agreed very well. Concluding that this may be a result of the different densities that the HI Zeeman effect samples, slightly different (lower densities) than does the OH.

Another observations with the VLA came from Sarma et al. (2013) who observed

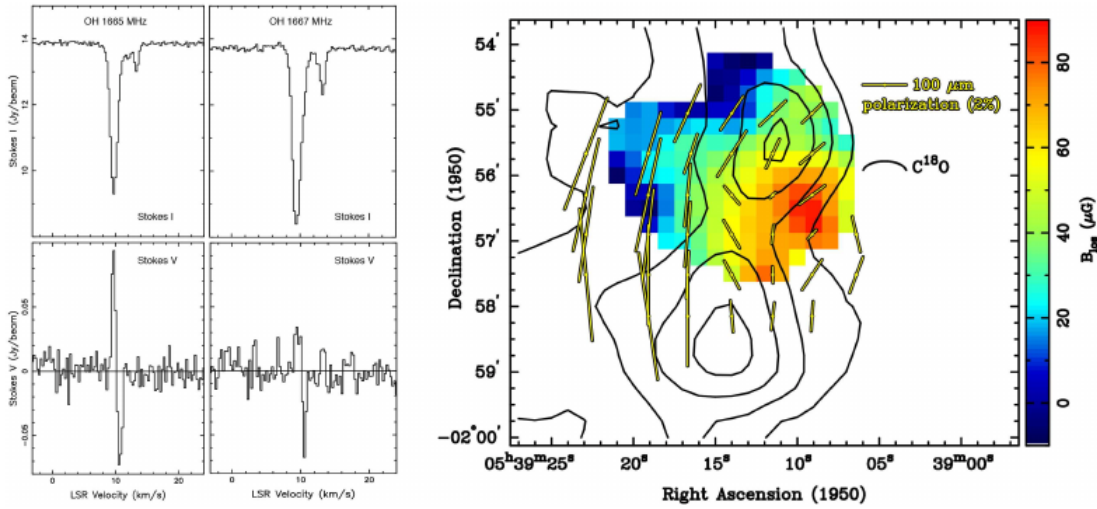


Figure 2.2.6: OH Zeeman Stokes I and V profiles toward NGC2024 at the peak B_{LOS} position from VLA mapping (Crutcher et al., 1999a). Right: Map of B_{LOS} (color) from OH Zeeman. Contours are C^{18}O intensities and yellow line segments are dust polarization directions (Hildebrand et al., 1995). The magnetic field in the plane of the sky is perpendicular to the dust polarization, hence roughly along the minor axis of the molecular cloud defined by C^{18}O (horizontal in the figure). Image from Crutcher et al. (1999).

the S88B region with VLA configurations B and C (11. km and 3.4 km, respectively). Without going into so many details of this work, they observed OH (1.665 and 1.667 GHz) in absorption with a bandwidth (BW) of 0.2 MHz and 128 frequency channels, thus giving a spectral resolution in each channel of 0.28 km/s. they observed the source for 6.7 hr with B-config and 8.9 hr with VLA C configuration. Additionally, the same author in Sarma et al. (2000) observed the Zeeman effect in HI and OH lines with the VLA (observations between 1993 and 1996). They targeted each line separately. HI observations were with a BW of 0.78 MHz and 128 frequency channels thus giving a resolution or channel spacing of 1.26 km/s and time on source of 12.6 hr. Additionally, OH was observed with a BW of 0.19 MHz and 128 frequency channels thus giving a resolution of 0.27 km/s and a source time of 4.3 hr.

Additionally, recent interferometric observations of Zeeman effects using ALMA was made by W. H. T. Vlemmings et al (2019) Vlemmings et al. (2019). Here, they observed TW Hya, which is a star of type K7 at 60 pc from us with a solar radii of $1.11R_{\odot}$ and surrounded by a 230 au proto-planetary disc with almost face-on geometry. They presented a calculation of the exact Zeeman splitting for

the CN hyperfine components in the ALMA band 3, 6, and 7 frequency range. However, Zeeman effect results at sub-mm and mm spectral range are very scarce in comparison with single dish results. The conclusion by the authors was that the observations indicate an excellent polarization performance of ALMA, but fail to detect significant polarization. Moreover, a more recent study of the circumstellar disk AS 209 observation of CN Zeeman effect in [Harrison et al. \(2021\)](#) detected dust polarization of the disk, but, they did not detect any polarized emission in the CN lines. It is clear that Zeeman effect observation is very time demanding due to the low circular polarization intensity in the ISM and the high spectral sensitivity dependence. Nevertheless, efforts in Zeeman effect observations are crucial because they are the only tools to measure the strength and direction of galactic and intergalactic magnetic fields.

2.3 Aperture Synthesis

2.3.1 Interferometry and Aperture Synthesis

For progress in astronomy, it is particularly important to measure the positions of radio sources with sufficient accuracy to allow identification with objects detected in the optical and other parts of the electromagnetic spectrum [Thompson et al. \(2017\)](#). Angular resolution in astronomy is extremely important. It describes the ability of radio telescope, to distinguish small details of an celestial source. Its calculus is approximately λ/D in units of radians, where λ is the observed wavelength and D is the diameter of the telescope. In optical and infrared astronomy ($0.4 \mu m - 300 \mu m$), high angular resolution is not complex to achieve due to the small observed wavelengths. Here, the limitations are the atmospheric turbulence and composition. In radio astronomy, observed wavelengths are in the orders of millimeters to a few meters, then, big antennas are needed to achieve a decent angular resolution of a few arc-minutes. For example, the Effelsberg telescope, with a diameter of 100 meters has an awesome collecting area, but its angular resolution is poor; at 21 cm wavelength, it is approximately about 7 arc-minutes. These huge structures are difficult to keep in accurate alignment and are subject to huge forces from wind and collapse due gravity.

Using interferometry technique, i.e., adding the signal of two or more antennas to measure the phase and amplitude of the incoming celestial signal allow

implementation of aperture synthesis. A direct measurement of an interferometer is the interference pattern between two given antennas. This pattern is related to the sky brightness observed by the antennas. The recorded complex value called visibility is then a Fourier transform of the sky brightness, the quantity which observations aim to recover [199 \(1999\)](#), [Thompson et al. \(2017\)](#). Additionally, the angular resolution will be approximately λ/B_{max} in units of radians, where λ is the observed wavelength and B_{max} is the maximum separation between a pair of antennas.

The radio astronomical technique of aperture synthesis, in which high-resolution images are produced from interferometer arrays, has been a scientifically productive tool for astronomers for decades [Marr et al. \(2011\)](#) and is still growing. From derivation of the theoretical concept in the 1950s to the creation of working instruments in the early 1960s, aperture synthesis was quickly recognized as a significant advancement for astronomy. Sir Martin Ryle shared the Nobel Prize for Physics in 1974 “for his observations and inventions, in particular of the aperture synthesis technique”. The best resolution attained with single radio antennas has historically been of order 20 arc-seconds, while that achieved with aperture synthesis can be four orders of magnitude better.

The u,v coverage is the sampling of points in the u,v plane which is perpendicular to the source direction. The quality of aperture synthesis images is usually determined by the density and distribution of u,v points in the u,v plane. These points are formed by the 2-d projection of the various interferometer baselines in the u,v plane [Thompson et al. \(2017\)](#). The u,v coverage is not a mask on the image itself, but is a mask on the Fourier transform of the image. It shows where on the Fourier plane the image has been sampled. It is a bit like putting the u,v coverage mask over the aperture of an optical telescope. The u,v plane coverage play a role in the sampling function, which is sampled through this plane and is equal to 1 where exist a measurement and 0 where does not exist. The inverse Fourier transformation of the sampling function is equal to the dirty beam or point spread function of the array. This project is focused in the u,v plane coverage and the point spread function for 5 different arrays at different observation time and source declination.

2.4 About the Bibliographic Revision

During the first months of this work, some concepts appeared immediately as requirements to understand how magnetic fields are characterized in the Universe using radio-astronomical observations. Basically, all the diagnostic tools used to obtain information about magnetic fields within the galactic and extra-galactic sources, depend critically of the electric field polarization state [A2](#). This is because it can not be directly measured the magnetic field of celestial objects in situ, except on the surface and in the vicinity of the Earth and in very limited regions in the Solar System. Nevertheless, radiation from distant stars and pulsars, gas clouds, galaxies, galaxy clusters, and the cosmic microwave background (CMB) can be observed, and, diagnose the magnetic fields by looking at magnetic effects on the generation and propagation of radiation. In summary, cosmic magnetic fields observations in radio-astronomy requires the understanding of polarimetry. Regarding these information, It was extremely necessary to understand what is polarization, how is described and worked in the radio-astronomy frame. Due to the large amount of information in this part of the project, it was decided to add this information in the appendix of this thesis. The appendix is organized as follows

- Appendix [A2](#) describes polarization in the radio-astronomy frame,
- Appendix [A3](#) summarizes radio-polarimetry theory i.e., basics matrices operation used in radio-astronomy to measure the Stokes parameters, physical quantities which are intrinsically related with the state of polarization, and,
- Appendix [A4](#) describes the Radio Interferometric Measurement Equation (RIME), a matrix-based mathematical model that describes the response of a radio interferometer in observation of polarization.

Chapter 3

Methods and Execution

3.1 Dual Polarization Instrument Approach

In section 2.2 it was made clear that the only way to characterize galactic and extra-galactic magnetic fields is by detecting the polarized radiation from the source and its surroundings. The scientific radio-polarimetric interferometers are designed to produce correlated products, i.e., XX, YY, XY, YX or RR, LL, RL and LR (see appendix A). These products are crucial to obtain a full source polarization characterization (see appendix A2.1 and references therein). In Sec. 2.2.6, Stokes V measures the circular polarization intensity and is related with the magnitude and direction of B_{LOS} . The only way to obtain V is with the difference between right and left circular polarization. Based on the last, a dual polarization system is required for Zeeman observations and the majority of polarization observations.

However, something not trivial is what type of feed system implement, i.e., linear or circular feeds. Linear feed systems are sensitive to linear polarization, i.e., X and Y electric field component. On the other hand, circular feed systems are sensitive to circular polarization, i.e., R and L electric field component. This choice will affect the whole system designed and response, even the polarization errors are different from one system and other Heiles (2002) Robishaw and Heiles (2021).

The design of the dual-polarization system was carried out by first understanding the mathematics behind polarimetry and the different type of elements and

antennas.

3.1.1 Primordial Requirements

Due to the nature of the Zeeman effect splitting, it is detectable by the difference of the circular right and left polarization intensity, which is equal to Stokes V proportional to the magnetic field that caused that splitting. In principal, to obtain the last parameter, is necessary a system capable to obtain both polarization. For a linear-dual polarization system which is sensitive to horizontal and vertical polarization is required a correlator to obtain both circular polarization states. On the other hand, circular dual-polarization system does not need a correlator to obtain both circular polarization states. The explanation given previously for both system is in the report of the first semester, which was based in the reviews of Heiles (2002) and in Robishaw and Heiles (2021). Due to the extensive description of the dual polarization frame work, this information in appendix A.

One principal requirement is a dual-polarization system. Looking into the chain of elements that form the system, there is necessary elements with low instrumental polarization. For the two antennas which form the system and illuminate the reflector, are required antennas with a broad radiation pattern capable to illuminate the majority of the reflector and to be separated each other a considerate distant to avoid mutual coupling. Besides, for the proposed array is crucial the implementation of a correlator, so, the understanding of this part is critical.

With respect to the proposed lines to observe, HI has a rest frequency of ~ 1.42 GHz ($\lambda = 21$ cm). OH has two close transitions to HI, 1.665 GHz and 1.667 GHz (~ 18 cm), where the first one has the strongest Zeeman splitting factor (see table 2.2.1). Taking into consideration Doppler effect, Doppler broadening and spectral distance between each line, the proposed instrument requires to be of broad-band, i.e., a wide bandwidth (spectral window) containing both lines, and, narrow channels (resolution).

3.2 Antenna Array

3.2.1 Sensitivity

For this investigation only analytical projection of the sensitivity was performed. This approach was with Python code based on the theoretical sensitivity equation from appendix A5 and showed in Eq. 3.2.1 for full bandwidth and 3.2.2 for spectral line sensitivity. Here, sensitivity and integration time were calculated by changing different parameters that could affect these values. It was adopted a 3 meters dish diameter antenna, 8 antennas, dual-polarization, T_{sys} values ranging from 150K to 500 K (with preference to worst case scenario), 0.5 to 300 MHz bandwidth. This projections were based only on theoretical equations from below

$$\Delta S = \frac{4\sqrt{2}kT_{sys}}{\epsilon_q\epsilon_a\pi D^2\sqrt{n_p}[N(N-1)/2]\Delta\nu\Delta t}, \quad (3.2.1)$$

where k is the Boltzman constant in Jy/K, T_{sys} is the system temperature, ϵ_q is the correlator efficiency, ϵ_a is the antenna efficiency, D is the antenna diameter, n_p is equal to 2 for dual-polarization observations, N is the number of antennas, $\Delta\nu$ is the bandwidth and Δt is the total observation time.

$$\Delta S = \frac{2kT_{sys}\sqrt{c}}{\epsilon_q\epsilon_a A_p\sqrt{n_p}[N(N-1)]\nu_{GHz}\Delta v_{km/s}\Delta t} \quad (3.2.2)$$

For the above equation, Δv is the line resolution expected using the following equation

$$L_{sr} = \frac{\Delta\nu}{N_{ch}}L_w = \Delta v, \quad (3.2.3)$$

where L_{sr} is the line spectral resolution, N_{ch} is the number of channel to use and L_w is the line width. So, using this equations it is possible to define Δv for Eq. 3.2.2 with a prior definition of the spectral configurations required for a great spectral line resolution.

3.2.2 Overview of the Antenna Array Simulations

To prove the observation capabilities of the proposed arrays, it was performed observation simulations and image cleaning with the Common Astronomy Software Applications package McMullin et al. (2007) (CASA version 5.6.3). Two principal tasks within CASA were used: `simobserve` to produce uv data sets and `tclean` to invert and deconvolve images with selected imaging algorithm. Additionally, others useful tools within CASA and the Astropy Astropy Collaboration (2022), Numpy Harris et al. (2020) and Matplotlib Hunter (2007) Python scientific and graphic modules were used to support the simulations and analysis process. The aim of the simulation is to quantify the synthesized beam performance with 5 different antenna array configurations by changing the total observation time and source declination.

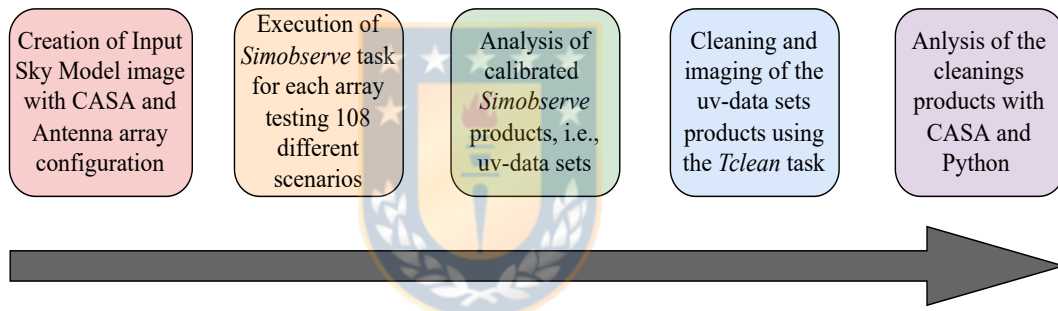


Figure 3.2.1: CASA workflow. Gray arrow indicates the simulations and analysis order.

Figure 3.2.1 shows the workflow followed for the observation simulations with the CASA package. It started with the study and later creation of two essential inputs: A sky-model image (CASA image format) (Sec. 3.2.2.2) observed during the simulations and the antenna array configuration position files (Sec. 3.2.2.3). Additionally, a voltage pattern for the primary 3-meters antenna response was required and created with the CASA tool `vpmanager`. This last was necessary because CASA did not have an antenna response for the 3-meters antenna and without this CASA could not generate uv data sets. Next, it was run `simobserve` task with the arguments from Table 3.2.2. A total of 108 observation simulations per configuration were performed, i.e., 12×9 (total observation time \times source declination). Then, `simobserve` uv data sets results were analyzed. Next, it was performed the cleaning with 3 different weighting schemes; Natural, Briggs (R=0.5) and Uniform, with a total of 324 image results per configuration. Moreover, 2

different iteration number were used, 0 iterations to obtain only dirty images and 1000 iterations for clean images. Mask images were used for specific cleaning boxes at different source declination. At last, it was performed analysis of the image and uv data set results.

3.2.2.1 Simulation Mechanics

The CASA package is a set of astronomical data reduction tools and tasks that can be run via the IPython interface to Python. Considering this, it was used Python modules and scripts to run tasks and tools during the simulations and image analysis process. For this stage, it was employed the `simobserve` task. In summary, this task simulates interferometric or total power measurement sets (uv data sets) for later cleaning. It is currently optimized for JVLA and ALMA, although many observatories are included, however, it is possible to add new observatories and antenna configurations.

Additionally, the CASA package has been used for similar works during a series of technical memos related to the next generation Very Large Array (ngVLA) [Carilli \(2016a\)](#), [Carilli \(2016b\)](#) and [Carilli \(2017\)](#)¹. Other example work is presented in [Deo and Kale \(2017\)](#) where the authors simulated observations using CASA to study the imaging response of extended source for the Giant Metrewave Radio Telescope (GMRT) and the Upgrade-GMRT.

Considering the previously mentioned, the CASA package was chosen to achieve the project's objectives among a limited set of software for aperture synthesis simulations. For this work, it was designed and created new antenna configurations (process described in Sec. 3.2.2.3). The `simobserve` task required inputs (arguments) to work. Below are described the more crucial ones:

- **project**: It is the name of the directory where the created measurement set will be created and located. Crucial. String.
- **skymodel**: It is the image to be observed by the array. It can be a fits or CASA image. It also can be a data cube. Crucial. String. File.
- **inbright**: It is the new scale surface brightness of brightest pixel in units of Jy/pixel. Crucial. String.

¹[ngVLA memo web page](#)

- **indirection**: Direction of the center of the image in equatorial coordinates. It is important to use observable declinations by the proposed array. Crucial. String.
- **incell**: It is the new cell/pixel size, i.e., the angular value of one pixel in the skymodel image. 1/4 or 1/5 of the beam is a good choice. (`simutil.approxBeam` gives the approximate beam size at zenith from the 90th percentile baseline length). Crucial. String.
- **incenter**: It sets the new frequency of center channel, i.e., observation frequency, e.g., 1.42 GHz or 1.665 GHz. Crucial. String.
- **inwidth**: It sets the new channel width, e.e., 0.8 MHz, etc. String.
- **integration**: It is the sampling time, different from total observation time. Crucial. String.
- **mapsize**: Angular size of the map to observe. Crucial. String.
- **obsmode**: Type of observation mode, interferometric or single dish. Crucial. String.
- **totaltime**: It is the total time of observation. Crucial. String.
- **antennalist**: It is the interferometer antenna position ".cfg" file. Configuration files already comes in CASA but can also be created. Crucial. String. File
- **sdantlist**: It is the single dish antenna position file. Irrelevant
- **thermalnoise**: It adds thermal noise with two options: `tsys-atm` or `tsys-manual`. Crucial. String.

Between all these arguments, `skymodel` and `antennalist` are files that must exist in the main simulation directory and within CASA tables, respectively. Sections 3.2.2.2 and 3.2.2.3 describe the process of sky model image and antenna array configuration creation, respectively.

3.2.2.2 Input Sky Model Image

The allowed images in CASA are FITS (Flexible Image Transport System) and CASA image type. For this simulation it was used CASA image format due to

errors with the FITS image format. Additionally, the most important to highlight is that these images have a header and data. This header contains keywords which describes structures and/or data that follow it in the image. The data refers to the value of each pixel in the image. For this simulations it was used 4D images, i.e. RA, DEC, Flux and Freq. Figure 3.2.2 shows the input sky model image used during this work.

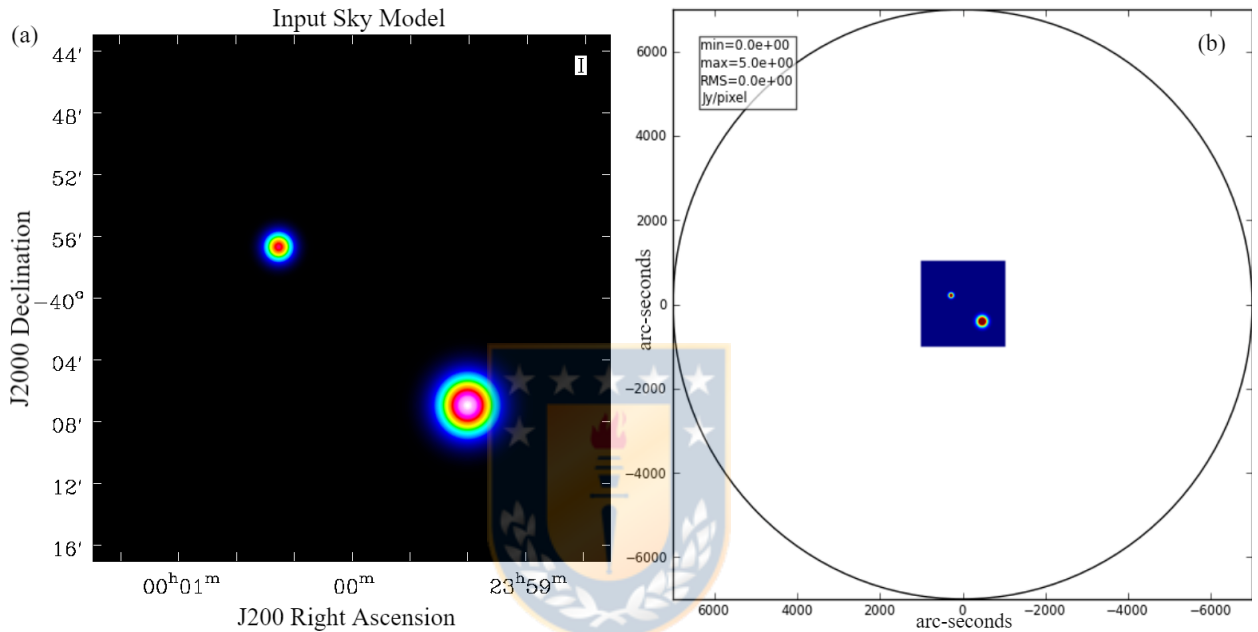


Figure 3.2.2: (a) Input sky model image created with CASA package. The image has a size of 512×512 pixels and is sampled at 4 arc-seconds per pixel. Image is presented with `imview` CASA task. (b) Sky coverage during the simulated observations

During the process of sky model image selection, it was chosen a few filamentary structures from the Herschel Gould Belt Survey (HGBS) public data [André et al. \(2010\)](#). However, the nature of the ISM at the observed wavelengths in this survey ($70\mu m - 500\mu m$) is different to the proposed to observe at 18 cm (1.665 GHz) and 21 cm (1.42 GHz). According to [Heiles and Crutcher \(2005\)](#) and [Troland and Crutcher \(2008\)](#), the diffuse HI medium characterize the Cold Neutral Medium and Warm Neutral Medium and is the matrix within which many molecular clouds reside. Additionally, OH is mainly observed in dark cloud cores within molecular clouds. Both lines are observed in atomic and molecular regions.

For this reason, these images were not employed for the final simulations but they were used to test the simulation mechanics parameters during preliminary results.

Due to the difficulty to find a great candidate to use a sky model image, it was proposed to create a basic synthetic model image, i.e., two Gaussian sources with different scale sizes at a few pixels separation.

Using the Common Astronomy Software Applications (CASA) package, it was created the input sky-model image showed in Fig. 3.2.2. This image is used as a synthetic celestial source to be observed with the proposed antenna array configurations. It has 2 Gaussian sources with different pixel size and separated a few pixels to test the angular resolution of the proposed array configurations. Image coordinates were left to 00h00d00.0s and -30d00m00.0s for graphic purpose only. Brightness pixel flux for the created image was left to 1 Jy/pixel. For the aims of this investigation, this value did not have to much consideration because only the synthesized beam performance was studied.

3.2.2.3 Creating and Adding an Antenna Array Configuration in CASA

Another crucial parameter and basically the basis of this work was the antenna configuration file. This file contains the coordinates points, elevations, diameters and names of each antenna in the configuration. Three types of coordinates system can be used, UTM (Universal Transverse Mercator) Northing and Easting, local XYZ and IRTF (International Terrestrial Reference System) XYZ, all in meters. Additionally, the elevation and diameter must be also in meters. The antenna name is not critical, however, it helps to identify the antennas graphically. Finally, the rows that start with the "#" symbol in the configuration file (im:cfgfile) are referred as the header keywords. The most important are the `coordsys` referring to the used coordinate system (UTM, LOC or XYZ), `datum` is the used datum, in this case WGS84 (World Geodetic System 1984) and `observatory` is the name of the respective observatory related with the antenna configuration, e.g., ALMA, VLA, ngVLA, etc.

CASA reads these configuration files and use them in the simulations. For this work, it was created all the configuration files from scratch. All tested antenna configurations where designed based on the feasibility, geography and permissions of the location. Below is described the process of antenna configuration file creation:

1. It was chosen the antenna locations and then found the geodetic coordinates (GCS Latitude and Longitude) using the Google Maps application². The adopted elevation for each antenna was 150 meters based on measurements using the web application calcmaps³ and supported with the Google Earth software⁴. Then, all the coordinates position (Lat-Lon-El only) for each configuration design were saved into an ascii file to be opened latter in CASA. It is important to use the North and West notation, i.e., -N for south and -W for east.
2. The longitude, latitude and elevation were converted into International Terrestrial Reference System (ITRF) XYZ coordinates using CASA tools. It was adopted the World Geodetic System 84 (WGS84) for the reference XYZ coordinate system. WGS84 includes correction for the Earth as a oblate spheroid, and is the standard for the GPS system, and for CASA. In this system, the Z axis is along the Earth's rotation axis, passing through the Earth's center of mass, and the X axis is a line passing through the Earth's center of mass and zero longitude and latitude. This conversion was done with the method `simutil.long2xyz` within `simutil`⁵ CASA tool utility class. It was employed CASA tools in order to maintain consistency with the CASA norms, given that the array evaluation is done in CASA. This required the latitude (N) and Longitude (W) in radians, elevation of each antenna in meters and the datum to be WGS84 (World Geodetic System 1984). After running this method, the XYZ products were saved into a text file with the ".cfg" extension, e.g., "configuration-A.cfg".
3. Inside the .cfg text file was added in column 4 the dish diameter equal to 3 and in column 5 the antenna's names (A01,...,A08). This last did not affect the simulations but it helped to identify each antenna graphically. Above this columns it was added header information, the used ITRF XYZ coordinate system and the Center Of The Array (COFA) in North and West coordinates. Header information was critical because without it CASA could not interpret the antenna configuration position.
4. These configuration files were saved into the "simmos" directory within

²<https://www.google.cl/maps/>

³<https://www.calcmaps.com/map-elevation/>

⁴<https://www.google.com/intl/es/earth/>

⁵<https://casa.nrao.edu/casadocs/casa-6.0/simulation/simutil>

CASA folder, however, they also can be saved into the main simulation directory. To save them into the "simmos" directory it was done using the "cp -r" command. However, as mentioned before, the configuration files can also be in the main simulation working directory.

5. After the configuration file was created and saved it was crucial to add the observatory name in the CASA table "Observatories". First, it was made a copy of the "Observatories" table (using cp -r since the table is a directory with sub-directories), and saved into the main simulation's directory. Moreover, it was necessary to create a file (in the main simulation directory) designated " /.casarc" with the following syntax: `measures.observatory.directory: /PATH TO THE MAIN SIMULATION DIRECTORY`. This was done because the used CASA version (5.6.3) does not allow to edit the original observatories table⁶.
6. Finally, using the task `browstable`⁷ it was possible to open and add the name of the observatory in the observatories copy table. Table 3.2.1 shows the used parameters for the created observatory.

Name	Type	Long	Lat	Height	X	Y	Z	Source
SCALPI	WGS84	-73.025	-36.841	150	0	0	0	Nima

Table 3.2.1: Parameters for the created observatory added in the observatories copy table in CASA. The provisional name for this observatory is SCientific and Academic L-band dual Polarization Interferometer (ScALPI).

The name ScALPI is the acronym for SCientific and Academic L-band dual Polarization Interferometer. This provisional name synthesizes the two focus that the instrument is proposed to aim, scientific and academic purposes. Additionally, It synthesizes the proposed dual-polarization mode and spectral band coverage where the desired lines to observe (HI and OH) are.

⁶More information about this step can be found in https://casaguides.nrao.edu/index.php/Antenna_List

⁷<https://casa.nrao.edu/casadocs/casa-5.4.0/data-examination-and-editing/browse-a-table>

3.2.2.4 Executing Simobserve Task

Before running `simobserve` it was necessary to create a primary beam response for the 3 meters primary antenna. This was done using the `setpbairy`⁸ function of the `vpmanager`⁹ tool within CASA which makes a primary beam antenna table response. It was created a response of a 3 meters dish diameter with 0.4 meters blockage diameter and linked to the created observatory table (see table 3.2.1) to use this response. Not doing this part `simobserve` will produce a severe error and not generate the sky-equation, i.e., no uv data sets for imaging.

After all the arguments were filled out, `simobserve` was executed. The only parameters that changed it were: pixel scale, declination (image direction), configuration file, scan time, total time, frequency of observation and channel width. Two different pixel scale was used, X arcsec equivalent to 1 pc at 150 pc and y arcsec equivalent to 1pc at 500 pc approximately. The used distance are from Taurus MC and Orion A MC, respectively. The width of 1 pc does not represent the inner and denser regions of a filament, but the outermost region yes. Declination from -10 to -90 (with 10 degrees separation) were used. A scan time of 30 seconds were used with a total time of 1 to 12 hours (with 1 hr separation) for observation. 1.665 GHz was the used frequencies and 300 MHz of bandwidth. A total 108 (9×12) simulations for each array were performed. Table 3.2.2 summarizes the arguments used with `simobserve`. It is important to clarify that only one sky-model image was used during the simulations and not a data-cube image. This is the reason why the Bandwidth used with `simobserve` was 100 MHz (see table 3.2.2). Not multi-frequency synthesis was simulated during this work.

The 108 simulations per configuration were done using a Python iterative script. After `simobserve` ended, it created a directory with the name assigned in the `project` argument, e.g., if `project = "simmo-1"`, the created directory name was "simmo-1". The `simobserve` outputs were:

- `project.[conf].ms` Table with the simulated measurement set, i.e., uv data sets
- `project.[conf].quick.psf` CASA image of the synthesized beam (Dirty

⁸<https://casa.nrao.edu/docs/casaref/vpmanager.setpbairy.html>

⁹<https://casa.nrao.edu/docs/casaref/vpmanager-Tool.html>

Primordial MS generation parameters (<code>simobserve</code> task)	
Argument	Value
Sky model (input image file)	Two separated Gaussian sources
Cell size ("/pixel)	4 and 7 arc-sec/pixel
Right ascension	00h00m00.0s
Declination	-10 deg to -90 deg (10 deg separation)
Frequency (GHz)	1.665 and 1.42
Bandwidth (MHz)	100
antenna list	Antenna configuration file
Scan time (seconds)	30
Total observation time (hr)	1 hr. to 12 hr. (1 hr step)

Table 3.2.2: Primordial `simobserve` arguments chosen for each (5) antenna configuration observation simulation. A total of 9 different declination and 12 total observation time were simulated for each antenna configuration, i.e, 108 results per configuration.

PSF)

- `project.[conf].skymodel` CASA image of the re-scaled skymodel
- `project.[conf].skymodel.flat` Flattened CASA image of the skymodel
- `project.[conf].ptg.txt` ASCII text listing the mosaic pointing
- `project.[conf].observe.png` PNG image showing elevation plot, antenna configuration, uv-coverage and PSF
- `project.[conf].skymodel.png` PNG image of the skymodel overlaid with the mosaic pointing

where `[conf]` refers to the name of the used configuration file in the simulation.

Finally, after `simobserve` completed all the simulations, the uv data sets were analyzed for later image cleaning with `tclean` task.

3.2.3 Image Cleaning

For inversion and imaging it was used `tclean` task. It was implemented Natural, Briggs ($R = 0.5$) and Uniform weighting schemes to evaluate the angular and sensitivity response of the configuration at different conditions. It was used the standard gridding option for the process of convolutional re-sampling of the measured visibilities onto a regular uv-grid prior to an inverse FFT (Fast Fourier Transform). For spectral mode it was used MFS mode for flat images (only one

output image). The deconvolver used was Hogbom for simple cases. It was used 0 iterations during cleaning to make dirty image and PSF and 1000 iterations to clean the image. For cell size it was used approximately 1/5 - 1/8 of the synthesized beam angular size for a better sampling. Table 3.2.3 summarizes the principal arguments used for each cleaning process.

Argument	Value
Image size (pixel)	Approx. the primary beam (256×256)
Cell size (")	1/5 to 1/8 of the PSF FWHM
Deconvolver	Hogbom
Weighting Scheme	Natural, Briggs (Robust, $R = 0.5$) and Uniform
Iteration number	0 and 1000
Mask	Mask image for specific region cleaning
antennas	All 8 antennas
UV-range	UV coverage to use (all)
Gridder	Standard (one FOV)

Table 3.2.3: Principal `tclean` arguments used for image cleaning. PSF FWHM stands for Point Spread Function Full Width at Half Maximum.

`textttclean` outputs are described below:

- `image-name.psf`: Point Spread Function
- `image-name.pb`: Primary Beam
- `image-name.residual`: Residual Image (or initial Dirty Image)
- `image-name.model`: Model Image after deconvolution
- `image-name.image`: Restored output image
- `image-name.image.pbcor`: Primary Beam corrected image
- `image-name.mask`: Deconvolution mask
- `image-name.sumwt`: A single pixel image containing sum of weights per plane
- `image-name.weight`: Image of un-normalized sum of PB-square (for mosaics and A-Projection)

A total of 324 (108 `simobserve` results \times 3 weighting schemes) different results for each array were obtained for dirty products and others 324 for

cleaning products.



Chapter 4

Results

4.1 The Dual Polarization Design Method

The research converged to the study of the stepped septum polarizer. It is a waveguide device, whose function is to transform linearly polarized electromagnetic wave at the input into circularly polarized EM wave with excellent axial ratio at the output and vice versa Samek (2002).

To calculate the stepped septum feed polarizer dimensions it was used the Zdenek Samek (OK1DFC) Samek (2002) set of equations ^{1 2}. These equations are used in the majority of the design for stepped septum polarizer

¹Zdenek Samek [web page](#) were the transformation equations were found and studied

²Direct [link](#) to Zdenek Samek transformation equations.

$$\begin{aligned}
A &= 0.338\lambda \\
B &= 0.597\lambda \\
C &= 0.86\lambda \\
D &= 0.961\lambda \\
E &= 1.6\lambda \\
F &= 0.08\lambda \\
G &= 0.178\lambda \\
H &= 0.301\lambda \\
I &= 0.491\lambda \\
J &= 0.626\lambda \\
K &= \lambda \\
L &= 0.19\lambda \\
M &= 0.185\lambda \\
N &= \sqrt{J^2 + K^2} = \sqrt{0.626^2\lambda^2 + \lambda^2} = \sqrt{1 + 0.626^2}\lambda \\
\alpha &= \arctan(J/K) = \arctan(0.626\lambda/\lambda) = \arctan(0.626) \quad ,
\end{aligned} \tag{4.1.1}$$

were λ is the wavelength in millimeters. The total length of the wave-guide, i.e., $E + K$, is equal to 2.6λ . Figure 4.1.2 is a side view of the stepped septum with each parameter from Eq. 4.1.1.

Table 4.1.1 contains the dimensions for each parameter in the stepped septum polarizer. The dimension parameters for the 1420 MHz design is 1.1725 times larger than the 1665 MHz design. Additionally, this sketch only takes into account the dimensions of the wave-guide part of the feed horn antenna and not the type, e.g., conical or corrugated. Moreover, square or circular wave-guide are possible to design with this stepped septum ³ polarizer.

For this project, it is required to have only one optic and receiver system with wide-bandwidth for both frequency lines (HI and OH). However, both lines can not be observable in parallel for spectral line observations. Section 4.2.1 discuss this in more details. In summary, the system requirements are a wide-bandwidth feed and receiver operating in a prime focus optical configuration with a 3-m

³Notes from [Septum Polarizers and Feeds](#), Paul Wade and W1GHZ, 2003

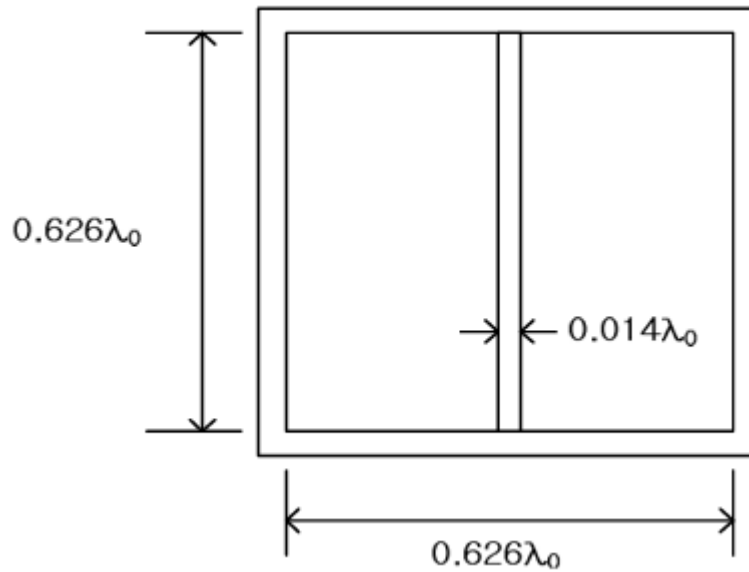


Figure 4.1.1: Stepped septum polarizer front view. Image from [Kim et al. \(2012\)](#).

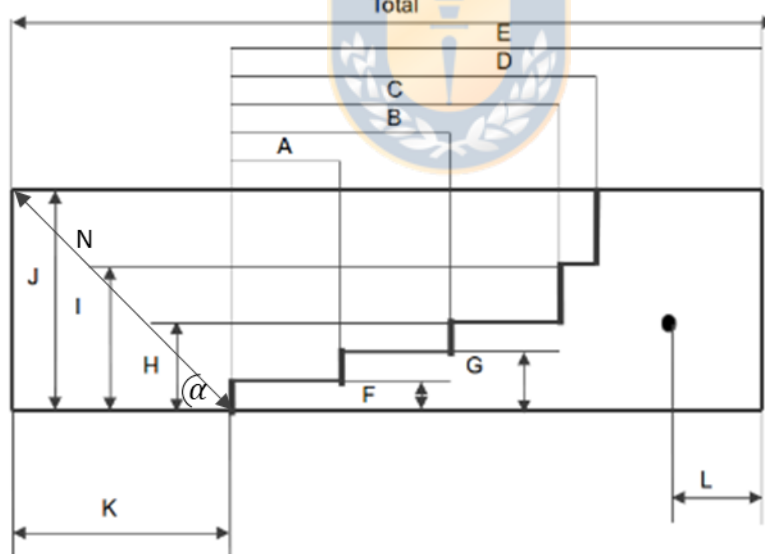


Figure 4.1.2: Stepped septum draw with each parameter. K is the distance from feed output to septum and L is the distance from probe to rear wall. The angle α is equal to the arctan of 0.626, which is equal to 32.047 degrees. Image credits [Lucas Teske](#).

single dish radio telescope. Both frequency range, 1420 MHz and 1665 MHz, respectively, must be covered by the system. Moreover, the system must provide dual-polarization products, which has been achieved with a stepped septum

polarizer [Wade \(2003\)](#), [Galuscak \(2004\)](#) and [Samek \(2002\)](#), but for Earth-Moon-Earth [Hazdra et al. \(2006\)](#) and amateur radio at 23 cm, 13 cm, 6 cm and others lines. A stepped septum polarizer for 21-cm HI and 18-cm OH lines was not found in the literature.

Frequency (MHz)	1420	1665
Wavelength (mm)	211.268	180.1802
Parameter	Length value (mm)	
A	71.4	60.9009
B	126.1268	107.5676
C	181.6901	154.955
D	203.0282	173.1532
E	338.0282	288.2883
F	16.9014	14.4144
G	37.6056	32.0721
H	63.5915	54.2342
I	103.7324	88.4685
J	132.2535	112.7928
K	211.2676	180.1802
L	40.1408	34.2342
M	39.0845	33.333
N	249.2493	212.5726
Total Length	549.2968	468.2652
Thickness	2.957752	2.521428

Table 4.1.1: Dimensions for each parameter from Fig. 4.1.2 using Eq. 4.1.1.

These results will be used in the future to design and for electromagnetic frequency simulations of the system, e.g., ANSYS HFSS. Additionally, a back end software designer would be necessary in the future work.

4.2 Antenna Array Configuration Results

4.2.1 Necessary Bandwidth and Channels

According to the instructions in the NRAO website ⁴, the line width of a species is based on a rule of thumb, i.e., 1 MHz in frequency corresponds approximately to x km/s for the wavelength line to x mm, e.g., 7 mm has a line width of approximately 7 km/s ⁵, so the 21 cm and 18 cm lines have 210 km/s and 180 km/s line widths,

⁴<https://science.nrao.edu/facilities/vla/docs/manuals/obsguide/modes/line>

⁵Another easier example is that 1 MHz = 1 km/s @ 300 GHz

respectively. Hence, the spectral resolution in km/s will be the better that x km/s can be resolved, this, in order to identify any shift effect on the line, e.g., Doppler-broadening or Zeeman effect. The expression to for the spectral line resolution is

$$\frac{BW}{N_{ch}} \times LW = L_{sr} \quad (4.2.1)$$

where BW is the bandwidth, N_{ch} is the number of frequency channels, LW is the line width and L_{sr} is the line spectral resolution. From this expression, the line width depends only of the targeted line wavelength, i.e., of the source. Additionally, L_{sr} is proportional to BW and inversely proportional to N_{ch} , therefore, it is expected to have this ratio smaller for a good spectral line resolution.

Now, if the system requires performance to consider the 2 lines, a bandwidth of at least 300 MHz must cover our system, now, for a resolution of a few km/s, e.g., 2.1 km/s, the number of channels must be from:

$$N_{ch} = (300 * 210)/2.1 = 30000 \quad (4.2.2)$$

Namely, each channel will be 300/30000 of 10 kHz resolution or 2.1 km/s of spectral resolution. As an example, ALMA delivers data cubes of up to 7680 channels and the width of these channels ranges from 3.8 kHz - 15.6 MHz, but the BW can not exceed 8 GHz (for continuum imaging the maximum is 7.5 GHz). Another example would be observations with the VLA, e.g., [Sarma et al. \(2013\)](#) who observed the S88B compact HII region with the VLA configurations B and C. Without going into more details of this work, they observed OH (1.665 and 1.667 GHz) in absorption with a bandwidth of 0.2 MHz and 128 frequency channels, thus giving a channel spacing of 0.28 km/s. Importantly, they observed the source for 6.7 hr with B-config and 8.9 hr with C-config. Additionally, the same author in [Sarma et al. \(2000\)](#) observed the Zeeman effect in HI and OH lines with the VLA (observations between 1993 and 1996). They looked at each line separately: HI observations with a bandwidth of 0.78 MHz and 128 frequency channels thus giving a resolution or channel spacing of 1.26 km/s ($0.78/128 \times 210$) and a time on source of 12.6 hr. Additionally, they observed OH with a bandwidth of 0.19 MHz and 128 frequency channels thus giving a resolution of 0.27 km/s and a time

on source of 4.3 hr.

These results suggest that observations of OH and HI in Zeeman are carried out separately in order to achieve a better spectral line resolution, since the number of frequency channels required to obtain a resolution of 1.2 km/s at a bandwidth of 300 MHz would be about 50000 frequency channels. Therefore, if only is desire to observe both lines separately, the bandwidth can be reduced and so can the number of frequency channels. Thus, lower bandwidth means higher resolution and higher number of channels also means higher resolution, in principle.

Now, the instrument's sensitivity and RMS are $\propto 1/\sqrt{BW}$, so a small bandwidth would not benefit the system's sensitivity and rms capabilities. To compensate for this, the integration time should be increased by a factor equivalent to what was taken from the bandwidth, i.e., if the original BW was A MHz and the integration time was T seconds, but A decreased by 0.01, then now T must increases by a factor of 100.

To resume this part of the investigation, it is proposed to observe both lines, HI and OH, in a spectral line mode by separate, i.e., only observe one line at the time.

4.2.2 Sensitivity

Results presented below are just theoretical projections of continuum and line sensitivity. It was first calculated the System Equivalent Flux Density (SEFD) of one antenna, i.e., a measurement of the weakest source of radio emission that can be detected. For these calculations, the system temperature T_{sys} and the aperture efficiency η_a were not know, however, a nominal value of 0.6 for η_a can be adopted. The SEFD was expressed in function of these two parameters. Defining the Boltzmann constant in Jy/K (1.38×10^3 Jy/K) and the antenna diameter $D = 3$ (m), the SEFD expressed in function of system temperature T_{sys} and antenna efficiency η_a was

$$SEFD = \frac{2 \times 1.38 \times 1000 T_{sys}}{\eta_a \times 4\pi(D)^2} = 390.46 \frac{T_{sys}}{\eta_a} [Jy] \quad (4.2.3)$$

From Eq. 4.2.3 it is possible to notice that the SEFD scales linearly with respect to T_{sys} and inversely with respect to η_a , the aperture efficiency of the antenna.

According to the equation described in A5, the system temperature is the sum of the receiver temperature, sky temperature, ambient temperature and also depends of the pointing elevation. Additionally, η_a ranges between 0 (worst) to 1 (best), making a big impact in the final result. A low T_{sys} and $\eta_a \sim 1$ is the perfect scenario for SEFD and therefore for the final continuum and line sensitivity. For the following calculation it was defined 5 different systems temperatures.

Analysis of the continuum and line sensitivity equation showed that the used bandwidth in both are different. Continuum sensitivity uses the whole bandwidth, mostly because we are not interest in one line specifically. However, line sensitivity equations uses the bandwidth over the number of channels. Also, the velocity in the line sensitivity equation is the product of the spectral line observation considerations, i.e., line-width, total bandwidth and number of spectral channels. high spectral line resolution requires small bandwidth, however, good spectral line sensitivity is lost with this condition. Figure 4.2.1 shows the theoretical spectral line sensitivity for the OH line at 1.665 GHz for different integration time, sensitivity and bandwidth. The top left image has the same spectral configuration used in Sarma et al. (2013) but with different number of antennas and antenna diameter. In this work, the reached line sensitivity was of 1.7 mJy/Beam. Clearly, the results for this work are very far from reaching these values of sensitivity.

Additionally, it was calculated the spectral lines sensitivity for HI line based on the spectral line parameters from Sarma et al. (2002) and Sarma et al. (2000). Figures 4.2.2 and 4.2.3 show the theoretical spectral line sensitivity for the HI line at 1.420 GHz for different integration time, sensitivity and bandwidth.

In both works the reached line sensitivity was of a few mJy/Beam, clearly, the results obtained for the proposed antenna array configuration is very far from a milli-Jansky spectral line sensitivity value. However, this is because the number and size of the antennas, 8 and 3 m, respectively, employed during these calculations, are different compared to Sarma et al. (2013), Sarma et al. (2002) and Sarma et al. (2000). These works observed with the VLA, which have 27 antennas of 25 meters in diameter.

Replacing only the values of antenna diameter and number of antennas in the sensitivity equation 3.2.1 (omitting the others parameters for practical purposes) with the general values of the VLA and the proposed array number and diameter

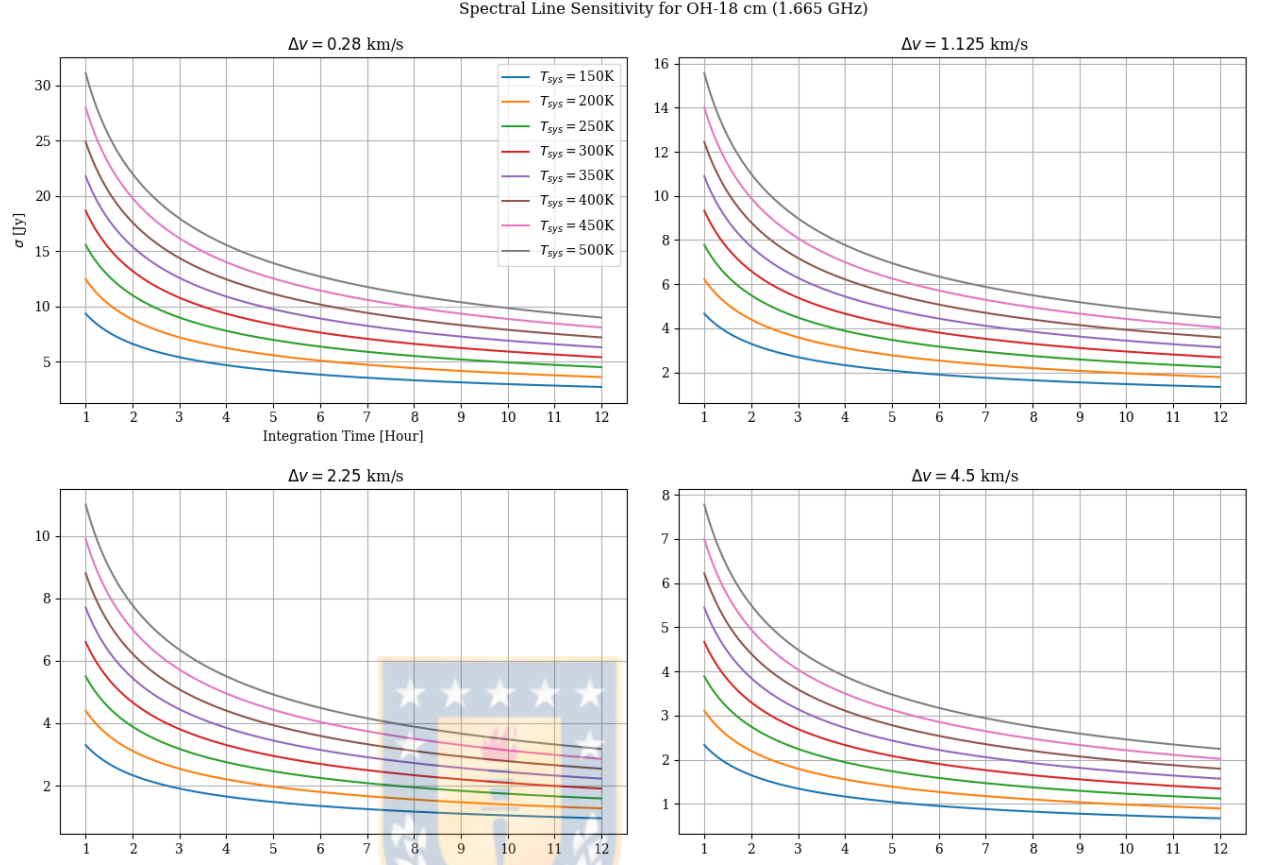


Figure 4.2.1: Theoretical spectral line sensitivity of OH line. General calculations parameters are 8 antennas of 3 meters in diameter, dual-polarization and 50 % of correlator and antenna efficiency, respectively. 8 different system temperature and 4 different bandwidth were tested. Top left graph has the same spectral configurations as in [Sarma et al. \(2013\)](#). Top right has 0.8 MHz, bottom left 1.6 MHz and bottom right 3.2 MHz bandwidth, respectively.

(8 and 3 m, respectively), gives the following results

$$\sigma_{VLA}/\sigma_{work} = \frac{1/(25^2)/1/(\sqrt{27 * 26})}{1/(3^2)/1/(\sqrt{8 * 7})} = \frac{6.0389 \times 10^{-5}}{0.0148} \sim 0.0041, \quad (4.2.4)$$

were σ_{work} is the sensitivity for the array presented in this work and σ_{VLA} is the sensitivity of the VLA. It is possible to see in the final results in 4.2.4 that $\sigma_{work} \gg \sigma_{VLA}$. To reach the value of σ_{VLA} without changing the antenna diameter of the proposed array, it will be necessary the enormous number of 1841 antennas. If the antenna diameter is change to 5 meters, it will be necessary 662 antennas in total, i.e., $\sim 1841 \times (3/5)^2$. This number is still a big number of antennas to place in.

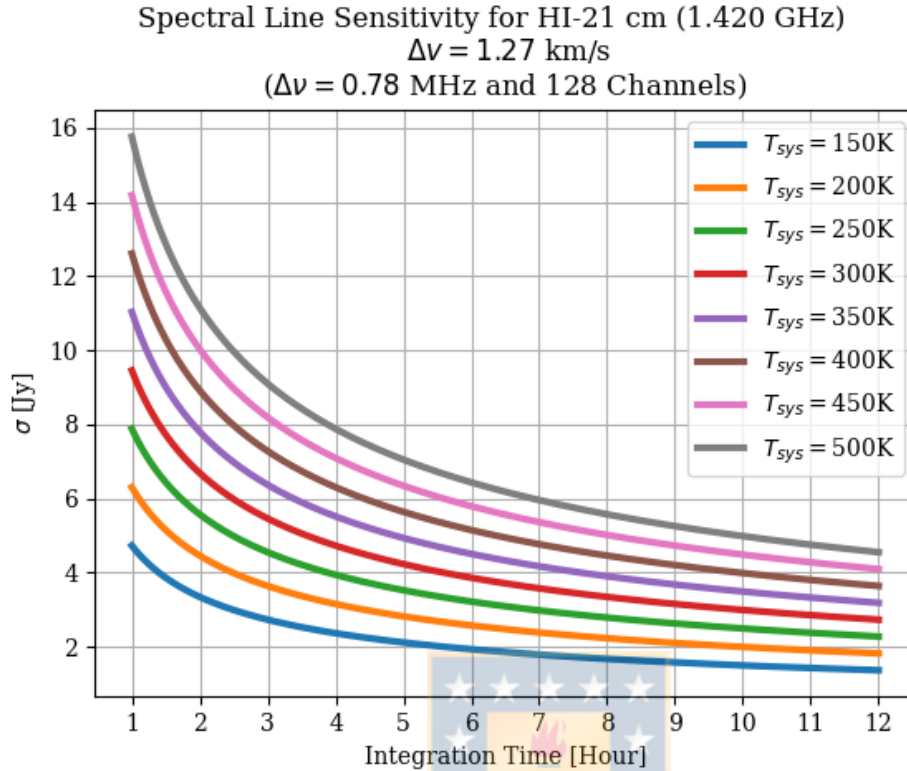


Figure 4.2.2: Theoretical spectral line sensitivity of HI line. General calculations parameters are 8 antennas of 3 meters in diameter, dual-polarization and 50 % of correlator and antenna efficiency, respectively. 8 different system temperature tested. Spectral parameters are from [Sarma et al. \(2000\)](#).

To improve the sensitivity, it will be necessary to reduce as much as possible the system temperature and increase the integration time. In addition, loss of spectral resolution and increasing the bandwidth may be an option to improve the system sensitivity without increasing the number and size of antennas.

4.2.3 Array Positions

For this work, it was designed and evaluated the synthesized beam performance of 4 semi-random antenna array configurations. Each array with a total of 8 antennas of 3 meters. During the preliminary simulation and analysis process, besides the 4 principal array configurations, a few different configurations were designed and evaluated. Finally, a 5th configuration was designed and evaluated along with the others 4 configurations. The proposed names for the 5 configurations were

- WLK (Fig. 4.2.4): It refers to WenuLafquen. It is the most compact

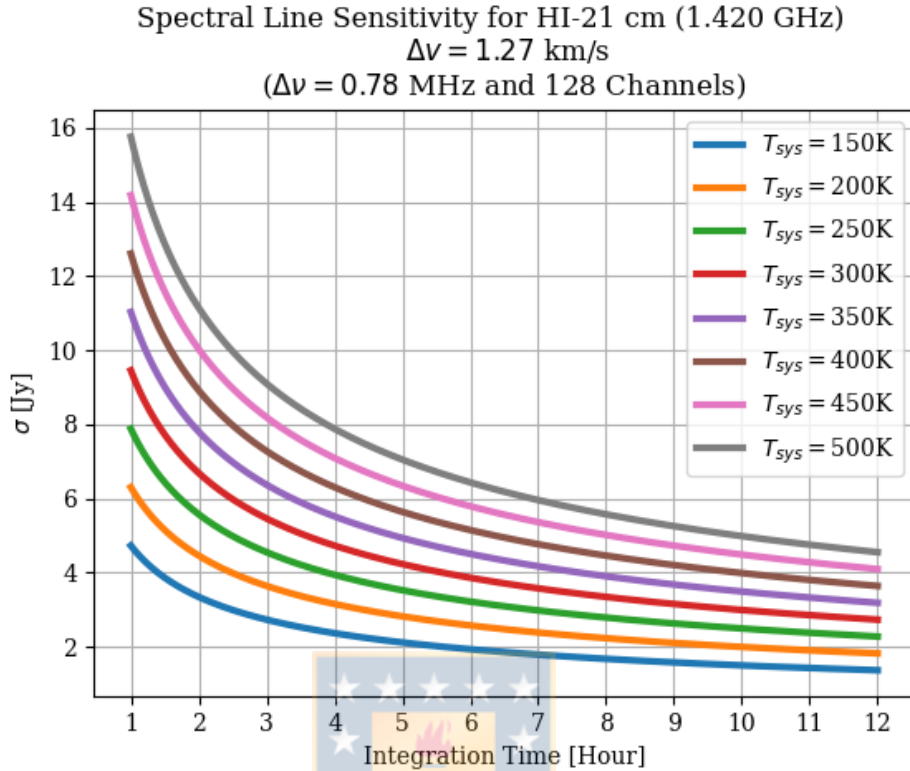


Figure 4.2.3: Theoretical spectral line sensitivity of HI line. General calculations parameters are 8 antennas of 3 meters in diameter, dual-polarization and 50 % of correlator and antenna efficiency, respectively. 8 different system temperature tested. Spectral parameters are from [Sarma et al. \(2002\)](#).

proposed configuration with each antenna location near the WenuLafquen area.

- E-CONF-A (Fig. 4.2.5): It refers to Extended Configuration A. It has 2 antennas located away from the area of WenuLafquen.
- E-CONF-B (Fig. 4.2.6): It refers to Extended Configuration B. It has 3 antennas located away from the area of WenuLafquen.
- E-CONF-C (Fig. 4.2.7): It refers to Extended Configuration C. It has 4 antennas located away from the area of WenuLafquen.
- MW-C+D (Fig. 4.2.8): It refers to the modify WLK configuration plus E-CONF-C and E-CONF-D (only of 5 antennas). It has 5 antennas located away from the area of WenuLafquen.

The antenna positions for each configuration were based on the feasibility and

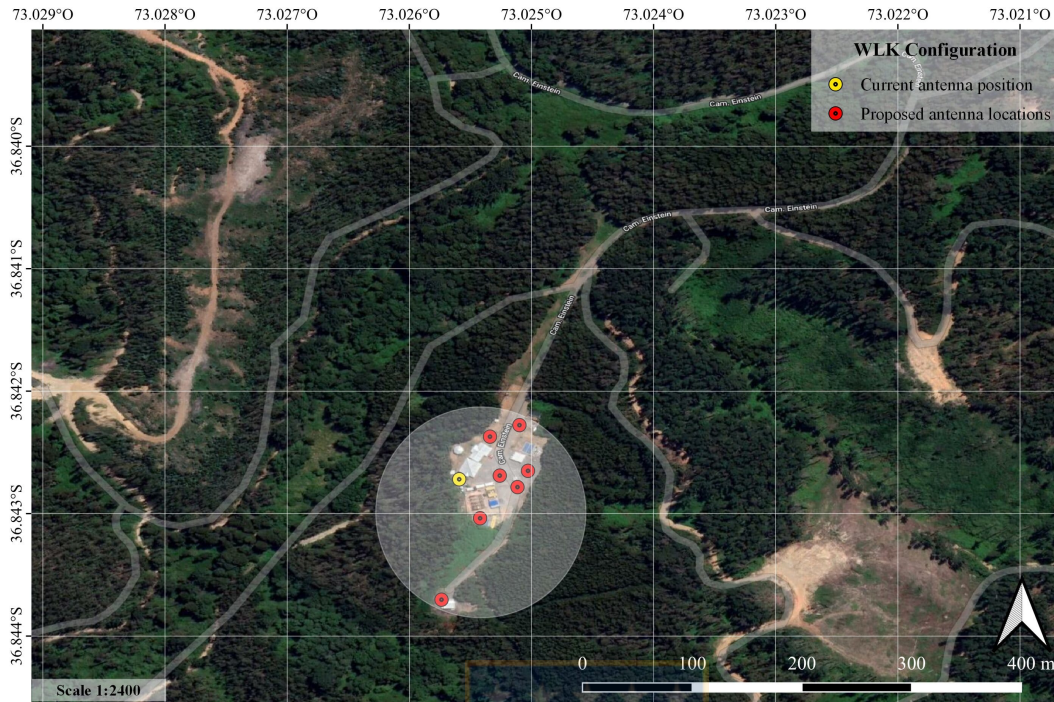


Figure 4.2.4: Antenna position for the WLK array configurations. White circle has a radii of 169 meters which corresponds to the maximum antenna separation distance. Maps generated with the open and free code Quantum Geographic Information System (QGIS version 3.16.13) using Google Maps Hybrid as layer map. White arrow points North and antenna symbols are not to scale.

the topography of the WLK site. The choice for the antenna positions in the central part (WenuLafquen) is due to the current existence of concrete pads and to not interfere with the surroundings. With respect to the antennas located in the exterior part, the chosen places were without trees around and in belonging to the University. With respect to the last, only configuration E-CONF-C and MW-C+D has one antenna outside of the University area. Table 4.2.1 displays the resolution and the scale at which severe attenuation of large-scale structure occurs for each proposed configuration. This table shows the maximum and minimum antenna separations, the approximate synthesized beam size (full width at half-power; the resolution element) for each line, and the maximum recoverable scale of detectable emission. Nevertheless, this are only approximation calculated with the `simutil` method within CASA called `approxBeam`. This method returns the approximate beam size at zenith from the 90th percentile baseline length. Additionally, the maximum angular scale structure that may be recoverable from observations with an interferometer depends on the minimum separation between antennas. The

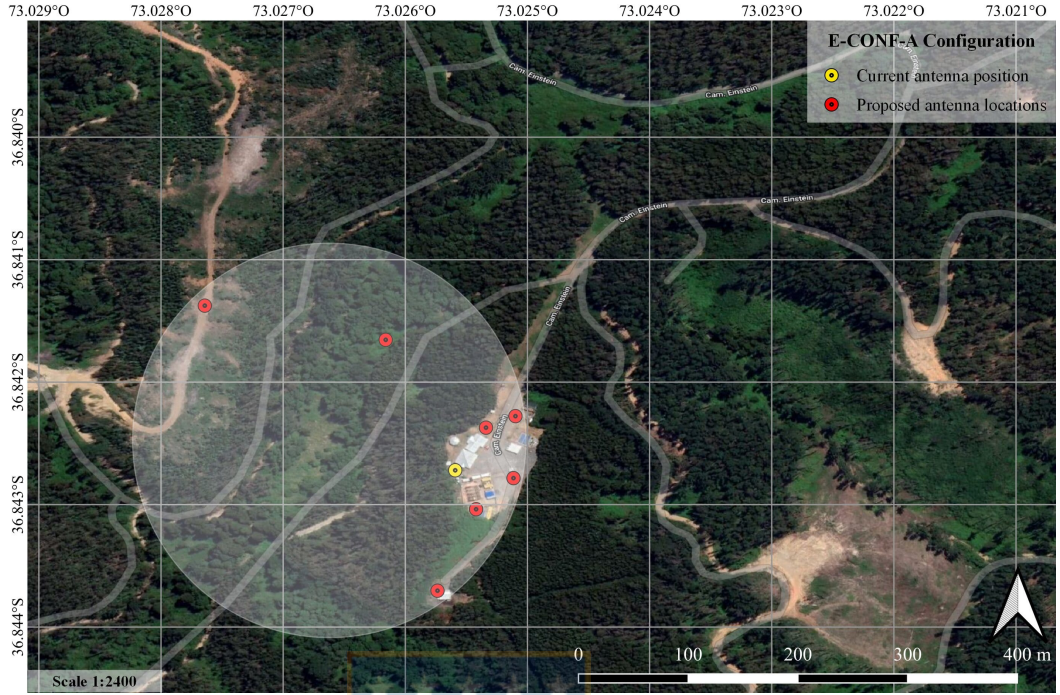


Figure 4.2.5: Antenna position for the E-CONF-A array configurations. White circle has a radii of 287 meters which corresponds to the maximum antenna separation distance. Maps generated with the open and free code Quantum Geographic Information System (QGIS version 3.16.13) using Google Maps Hybrid as layer map. White arrow points North and antenna symbols are not to scale.

expression ⁶ is

$$\theta'_{MRS} = \left(0.6 \frac{\lambda}{B_{min}} \frac{180}{\pi} \times 60 \right) , \quad (4.2.5)$$

where B_{min} is the minimum antenna separation distance. This value represents the maximum recoverable scale to be resolved by the configuration in angular scales.

4.2.4 Simulation Results

Before driving an observation, it is crucial to justify the source observability, i.e., the source elevation trough time of observation. For the proposed configuration location, it is desire to observe at a elevation over 30° . Figure 4.2.9 summarizes the elevation curves for each source declination at transit observation only (hour angle equal to 0 hour). These plots were relevant since they warned of an error in

⁶This equation is from the [ALMA early science primer](#) document.

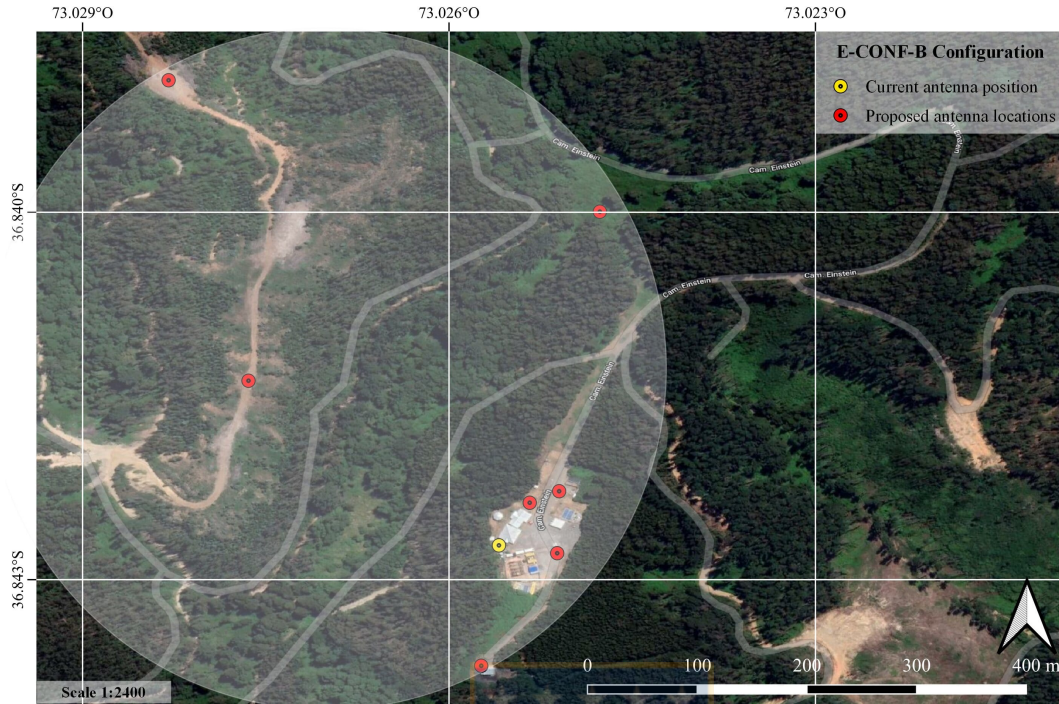


Figure 4.2.6: Antenna position for the E-CONF-B array configurations. White circle has a radii of 579 meters which corresponds to the maximum antenna separation distance. Maps generated with the open and free code Quantum Geographic Information System (QGIS version 3.16.13) using Google Maps Hybrid as layer map. White arrow points North and antenna symbols are not to scale.

Configuration properties

Configuration	WLK	E-CONF-A	E-CONF-B	E-CONF-C	MW-C+D
$B_{max}(m)$	169	287	579	665	509
$B_{min}(m)$	15	15	22	37	59
Freq.	Synthesized Beamwidth θ_{HPBW} (arcmin)				
1.420 GHz	5.2	3.2	1.5	1.3	1.7
1.665 GHz	4.5	2.6	1.3	1.1	1.4
Freq.	Maximum Recoverable Scale θ_{MRS} (arcmin)				
1.420 GHz	35	35	24	14	15
1.665 GHz	30	30	20	12	12

Table 4.2.1: Theoretical resolution properties of the 5 proposed configurations. B_{max} is the maximum antenna separation, B_{min} is the minimum antenna separation, θ_{HPBW} is the synthesized beam width (FWHM), and θ_{MRS} is the maximum recoverable scale visible to the array. $\theta_{HPBW} \propto \lambda/B_{max}$ and $\theta_{MRS} \propto \lambda/B_{min}$, both in radians.

the location of the antennas during the first stage of this work. X axis in each image are relative hours. Changing the source right ascension only moved the curves plots in the X axis (time).

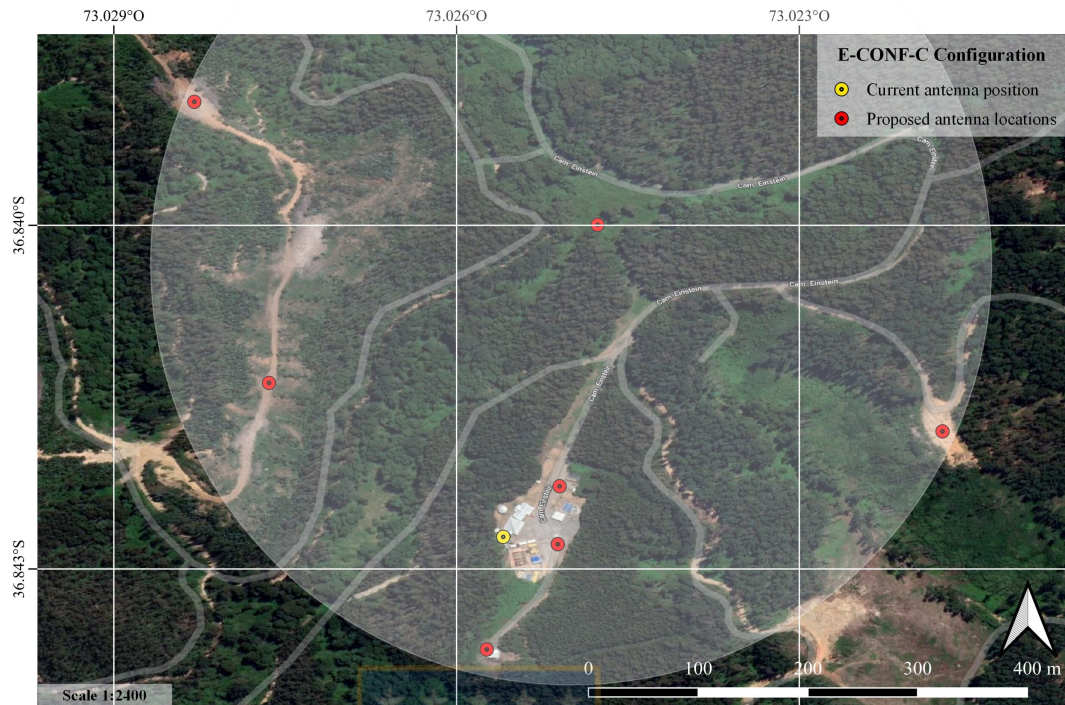


Figure 4.2.7: Antenna position for the E-CONF-C array configurations. White circle has a radii of 665 meters which corresponds to the maximum antenna separation distance. Maps generated with the open and free code Quantum Geographic Information System (QGIS version 3.16.13) using Google Maps Hybrid as layer map. White arrow points North and antenna symbols are not to scale.

These elevation source curves revealed that at -40° to -80° is possible to have full observability for a 12 hour observation. Additionally, for 1 hour to 8 hours it is possible to have full source observability for all the tested declinations. Comparing these results with the online object visibility tool STARALT⁷ it was possible to know that September has a observability similar to the curves in Fig. 4.2.9 for the tested source coordinates. It is important to clarify that CASA elevation curve plots are only a hypothetical scenario and not a real one. However, they are in agree with the results of STARALT.

In the following section are presented the results of the CASA simulations; the uv plane coverage, synthesized beams performance for each antenna configuration.

4.2.4.1 UV-coverage and Dirty Beams

As expressed in Sec. 2.3.1, an array during different integration times, source declination and used bandwidth will produce different coverage in the u, v plane. Additionally, the array configuration and geographic location will produce different



Figure 4.2.8: Antenna position for the MW-C+D array configurations. White circle has a radii of 509 meters which corresponds to the maximum antenna separation distance. Maps generated with the Quantum Geographic Information System (QGIS version 3.16.13) using Google Maps Hybrid as layer map. White arrow points North and antenna symbols are not to scale.

coverage. For the proposed array latitude of 36.841° (S), it was expected to have and excellent coverage at source declination of -40° . other declination are intermediate in behavior. Figures 4.2.10 and 4.2.11 show the u,v plane coverage (in meter units) for the 5 tested configuration arrays at different source declination (-10° to -90°) during 2 hour and 12 hour synthesis observation simulation, respectively.

It is possible to observe the big impact that have the observation time and antenna position in the u,v plane coverage for all the configurations. From -50° to -90° source declination the u,v plane present a great coverage. Only WLK configuration presents considerably null spaces in the u,v plane and slightly oriented to the N-E direction. The others configurations (E-CONF-A, B and C) presents a u,v plane coverage slightly oriented to the N-W direction. Analyzing these results, and the antenna positions of the first 4 proposed antenna array configurations was possible to design the MW-C+D configuration. MW-C+D u,v plane coverage results revealed a well sampled u,v plane.

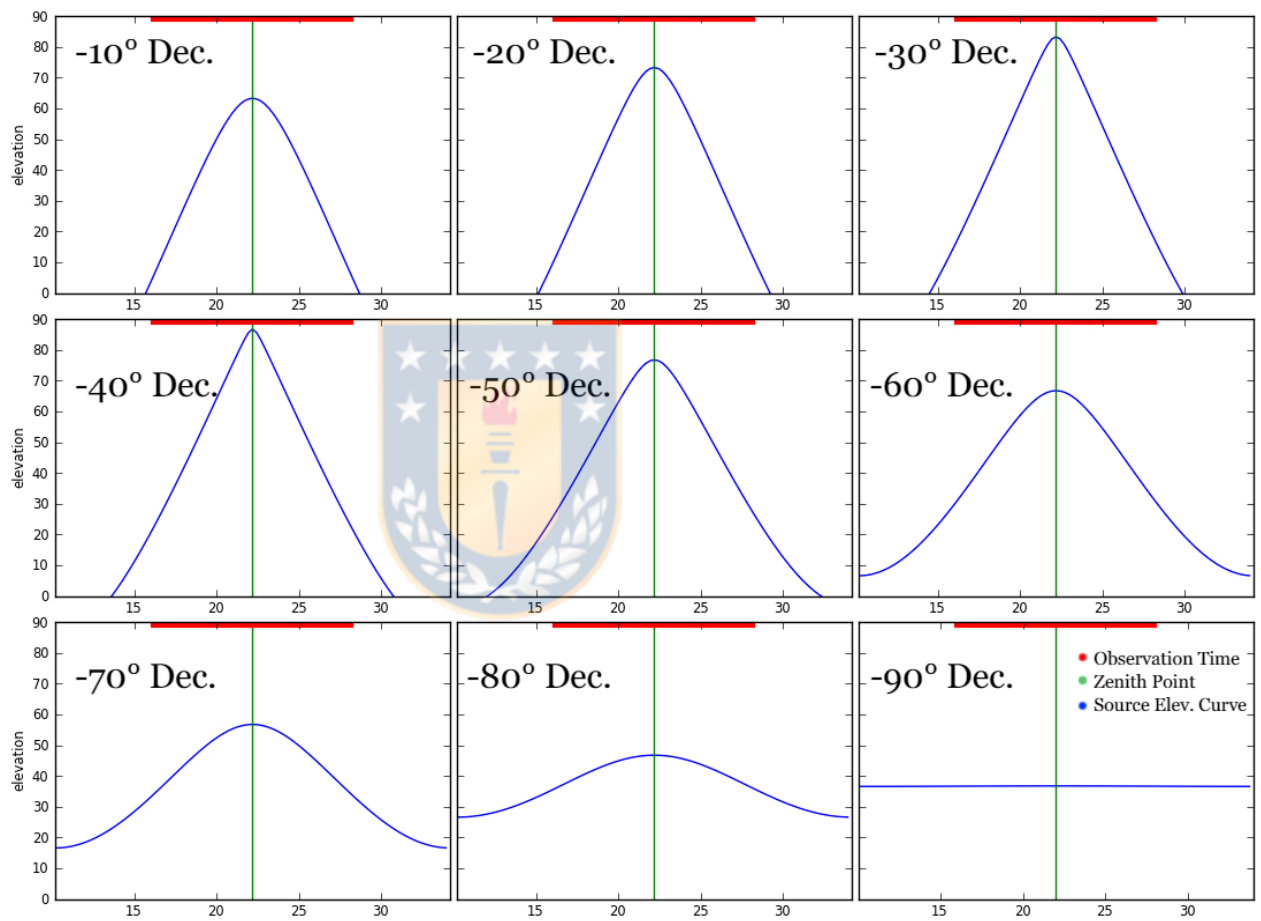


Figure 4.2.9: Elevation curves for the 9 different tested source declination at 36.841° (S) latitude and 73.025° (W) longitude. Observation time (red line) is for a total of 12 hours. X axis in each images are relative hours.

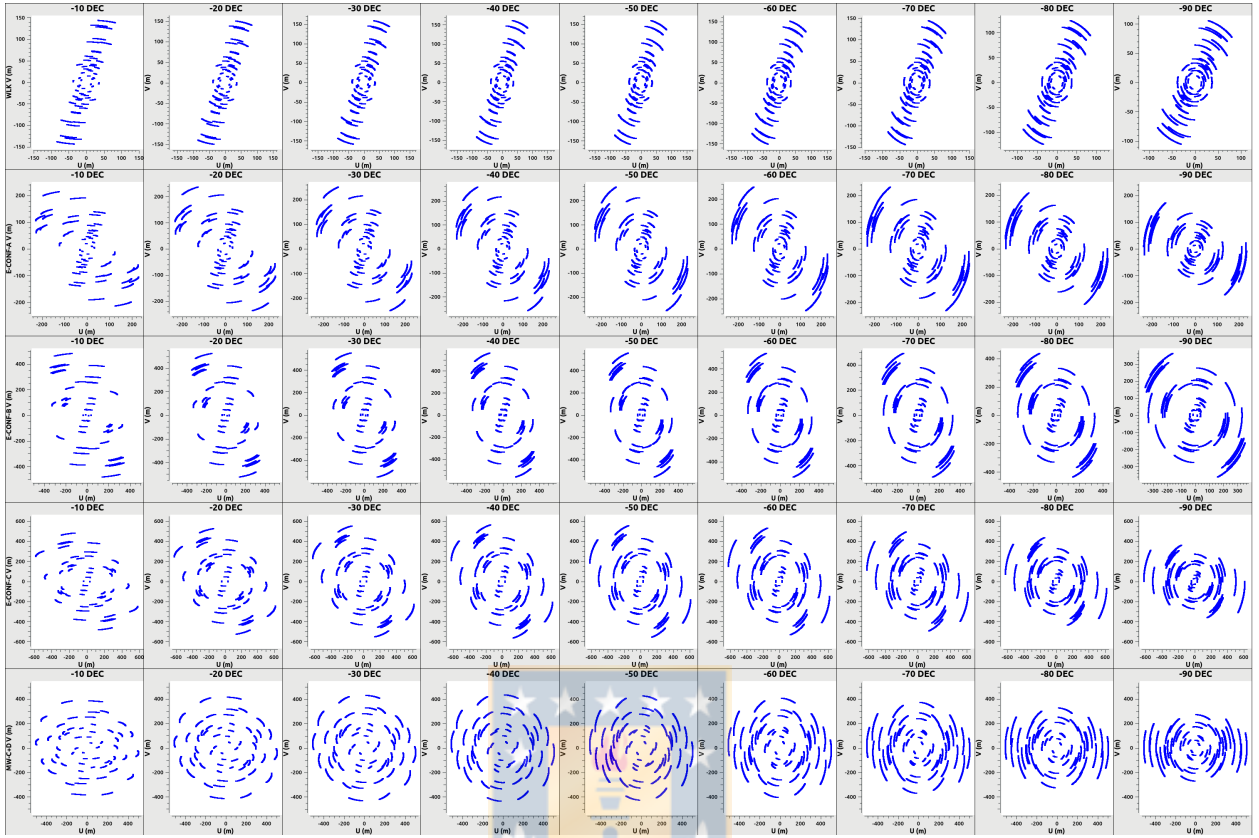


Figure 4.2.10: U, V plane coverage for 2 hour synthesis simulation results. From top to bottom are WLK, E-CONF-A, E-CONF-B, E-CONF-C and MW-C+D configuration, respectively. Left to right columns are declination from -10° to -90° . Plots created with CASA task `plotms`.

These results does not show the u,v plane coverage performance of the arrays in bandwidth synthesis observations, however, it is enough to produce results of the synthesized beam dimensions and shape. Figures 4.2.12 and 4.2.13 show the synthesized beams for 1 and 12 hour synthesis simulations at -10° source declination for all the configurations and employed weighting schemes. It is possible to observe the reduction of side lobes (noise peaks) when increasing the integration time. Additionally, the sampled major and minor beam width reduce in size when increasing the integration time. Natural weighting produced the widest synthesized beam and side lobes. Uniform weighting produced smallest synthesized beams and low side lobes, however, negative amplitude close to the sampled beam is observed. These negative amplitude values can remove flux to the final cleaned image.

Figure 4.2.14 shows the synthesized beams from the results of 12 hour integration

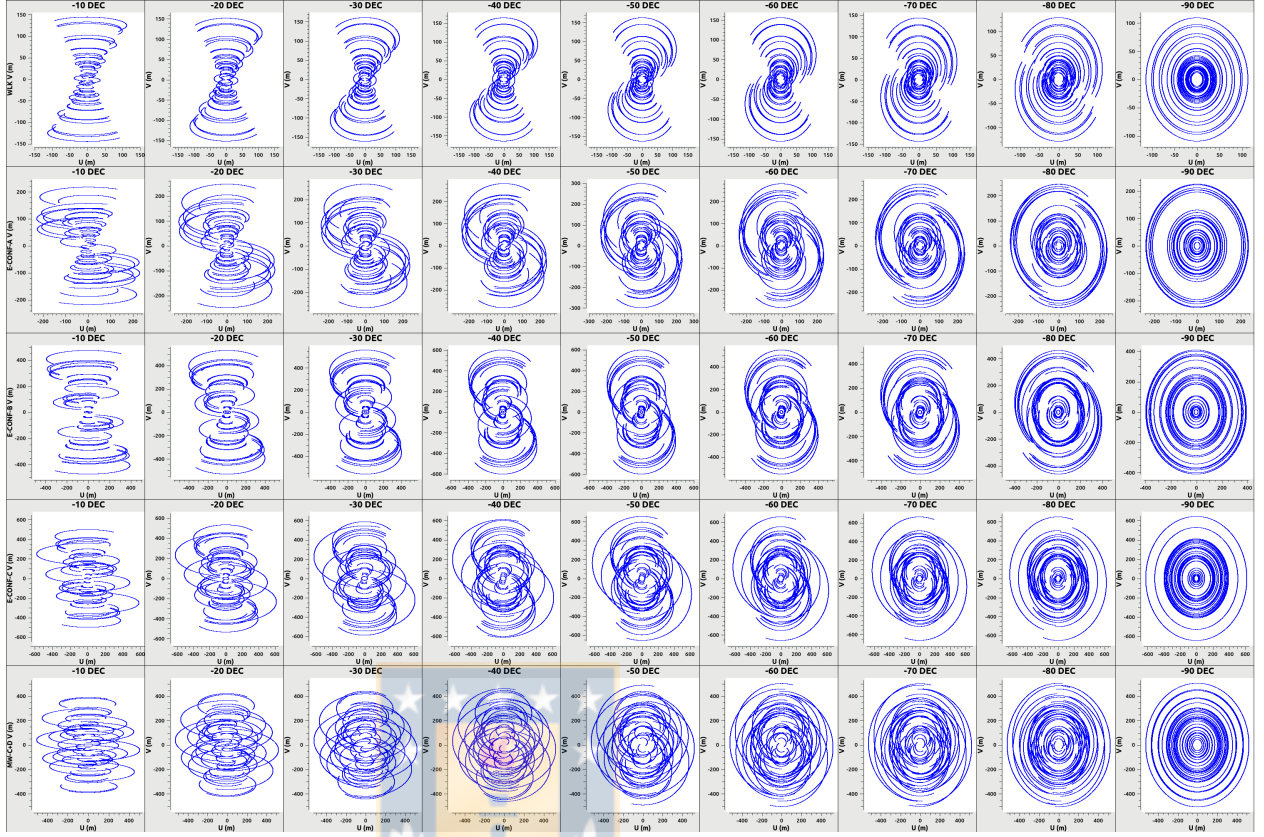


Figure 4.2.11: U, V plane coverage for 12 hour synthesis simulation results. From top to bottom are WLK, E-CONF-A, E-CONF-B, E-CONF-C and MW-C+D configuration, respectively. Left to right columns are declination from -10° to -90° . Plots created with CASA task `plotms`.

time at a source declination of -80° . These images test the impact in increasing the integration time and the targeted celestial coordinates of the source.

Additionally, a size comparison analysis where applied to the fitted Full Width at Half Maximum (FWHM) of the Point Spread Function (PSF) results. Figure 4.2.15 shows a set of histograms plots of the size comparison of the FWHM for all the proposed configurations with Natural weighting scheme. It is possible to observe the big size difference of the WLK FWHM with respect to the other configurations. The smallest FWHM was achieved with the E-CONF-C configurations, however, it is only 0.83 times smaller than the MW-C+D configuration. Thus MW-C+D configuration is ~ 1.2 times bigger than E-CONF-C PSF, which is not a big difference with respect to the others configurations. Also, MW-C+D configurations has antennas closer to the core region of the WenuLafquen observatory.

In addition to the analysis presented above, Fig. 4.2.16 shows a size comparison

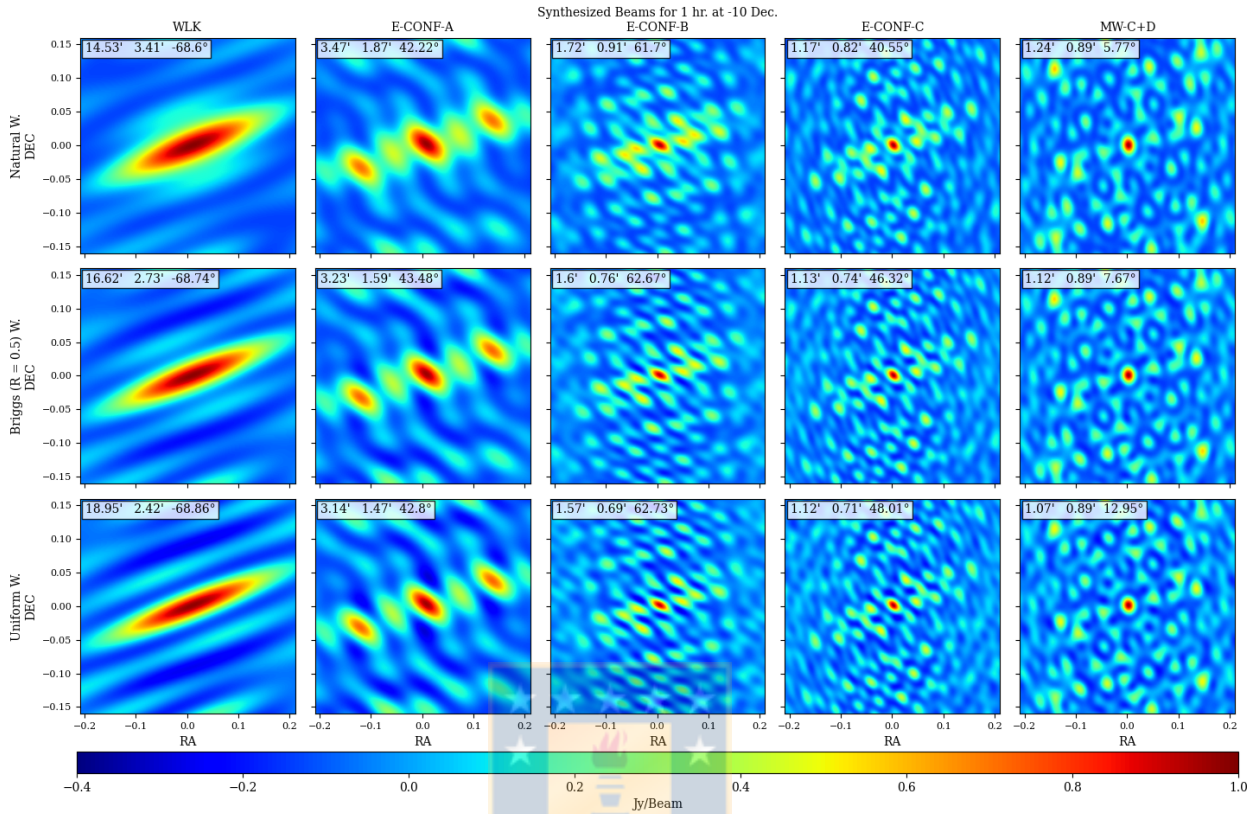


Figure 4.2.12: All configurations cleaned synthesized beams for 1 hour aperture synthesis simulation at 1.665 GHz for the image model at -10° declination. Top to bottom rows are Natural, Briggs and Uniform weights, respectively. Top left rectangle shows the θ_{maj} , θ_{min} and position angle, respectively. Each image has the same scale. Minimum synthesized beam values were left to -0.4 to 1 $Jy/beam$ to color-scale all images.

of the fitted FWHM for Natural weighting between Briggs and Uniform weighting

4.2.4.2 Major and Minor Beam Width

The Point Spread Function (PSF) is the response of an optical system to a point source. In radio-astronomy, it is often referred as synthesized beam and is the results of the inverse Fourier transform of the sampling function (u,v plane coverage). CASA results revealed two useful values to study the PSF performance, the sampled major and minor beam widths. Figure 4.2.17 shows a draw of the beam with the major and minor beam widths and the position angle. The position angle is 0 to 90° in the red arrow direction and 0 to -90° in the other direction.

Figure 4.2.18 shows scatter plots of the major beam versus integration time color weighted by source declination. The results of each configuration and employed

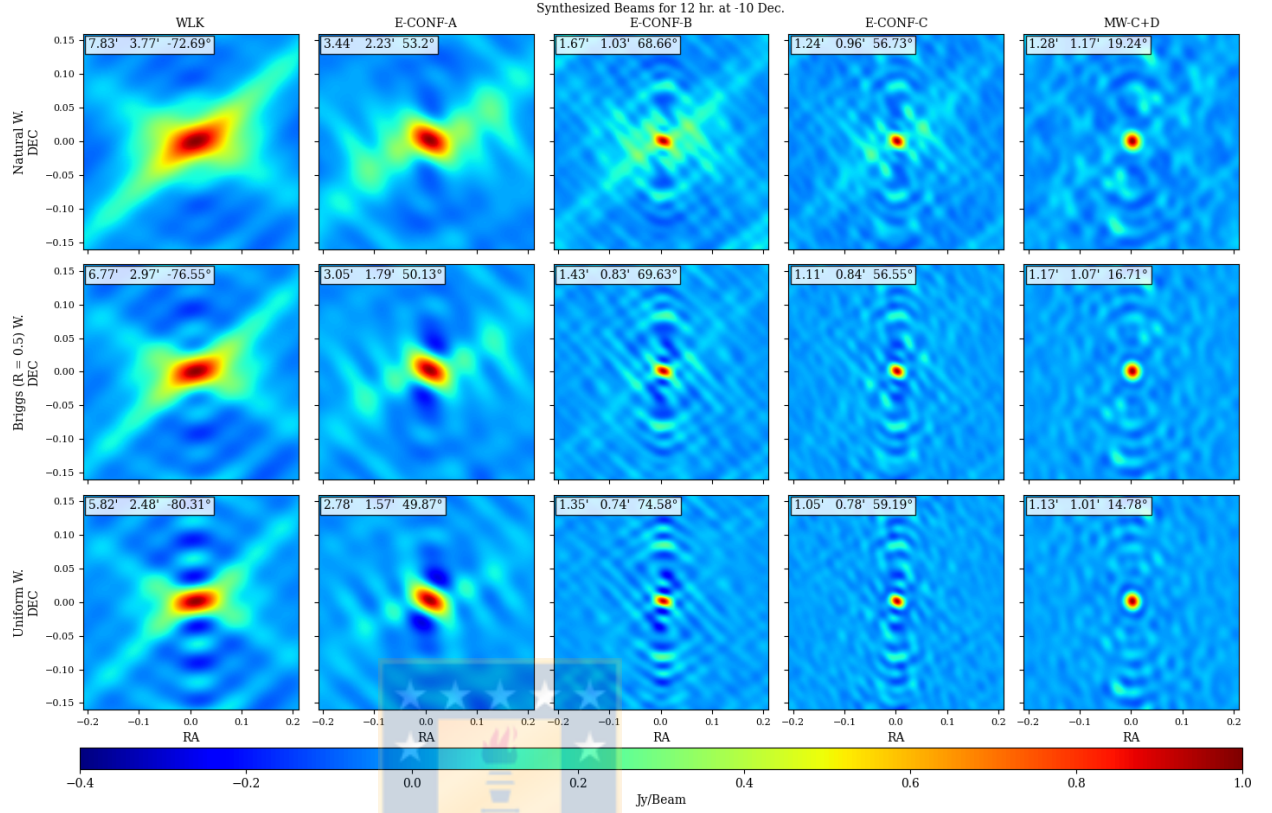


Figure 4.2.13: All configurations cleaned synthesized beams for 12 hour aperture synthesis simulation at 1.665 GHz for the image model at -10° declination. Top to bottom rows are Natural, Briggs and Uniform weights, respectively. Top left rectangle shows the θ_{maj} , θ_{min} and position angle, respectively. Each image has the same scale. Minimum synthesized beam values were left to -0.4 to 1 $Jy/beam$ to color-scale all images.

weighting scheme is presented for comparison reasons. WLK configuration has the biggest major beam widths that has a notorious decrease when the integration time increase. Additionally, it is possible to notice that for the other configurations, the major beam widths decrease at higher integration time, however, they do not present any notorious order like the results of WLK. Another observation is that at higher source declination and short integration time the major beam width is larger than low declination.

With respect to the weighting schemes results, at short integration times the major beam width for WLK configuration is smaller when using Natural weighting than when using Briggs or Uniform weighting. However, when increasing the integration time this change and Uniform weighting results have smaller major beam widths. For the other configuration results, the major beam width is

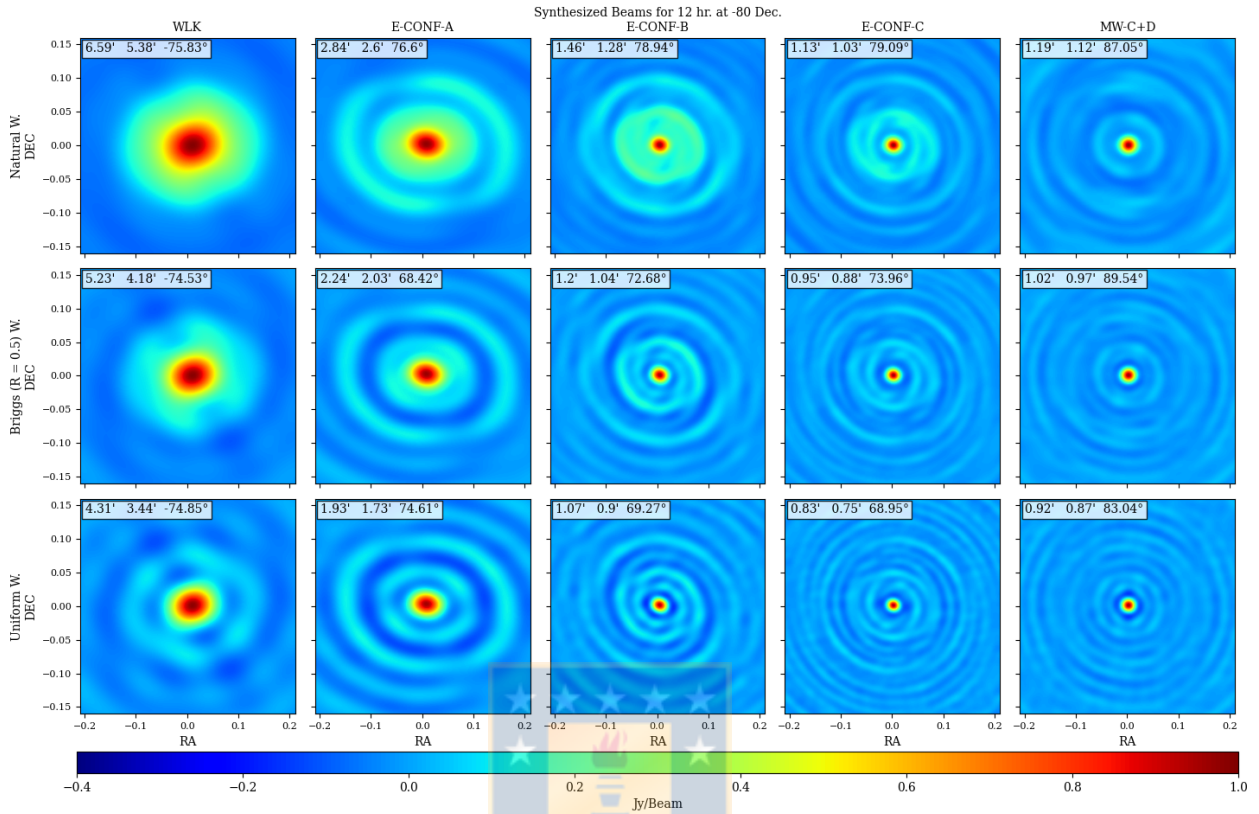


Figure 4.2.14: All configurations cleaned synthesized beams for 12 hour aperture synthesis simulation at 1.665 GHz for the image model at -80° declination. Top to bottom rows are Natural, Briggs and Uniform weights, respectively. Top left rectangle shows the θ_{maj} , θ_{min} and position angle, respectively. Each image has the same scale. Minimum synthesized beam values were left to -0.4 to 1 $Jy/beam$ to color-scale all images.

smaller for Uniform weighting and higher when using Natural weighting. The most notorious observation is the impact that have the integration time in the major beam width size.

Additionally, Fig. 4.2.19 shows the same that in Fig. 4.2.18 but for the minor beam width results. Al contrary to the results described above, the minor beam width increase in size when increasing the integration time. Additionally, the source declination has a big impact in the majority of the simulated scenarios. For MW-C+D configuration at low source declination the minor beam width is higher. For the others configurations (WLK, E-CONF-A,B and C) the minor beam width is higher at higher source declination. Again, it is notorious the impact of the integration time in the minor beam width.

With these results it was possible to study the impact of the integration time and



Figure 4.2.15: Histogram plots of the FWHM size comparison for Natural weighting scheme. 50 bins were used. j sub-index corresponds to the configuration in the numerator and k sub-index corresponds to the configuration in the denominator.

source declination in the synthesized beam. At higher integration time the major beam width decrease and the minor beam width increase in size. Additionally, values below 5 arc-minutes were achieved for the majority of the configuration. Only WLK configuration has sizes above 5 arc-minutes and below 18 arc-minutes in short to intermediate observation times.

4.2.4.3 Synthesized Beam Eccentricity

A quality factor for the Point Spread Function to analyze each configuration performance was the eccentricity (ϵ). It takes into account the major and minor beam width results from Sec. 4.2.4.2. The eccentricity metric measures the distortion from circular symmetry. The expression used to calculate the eccentricity was

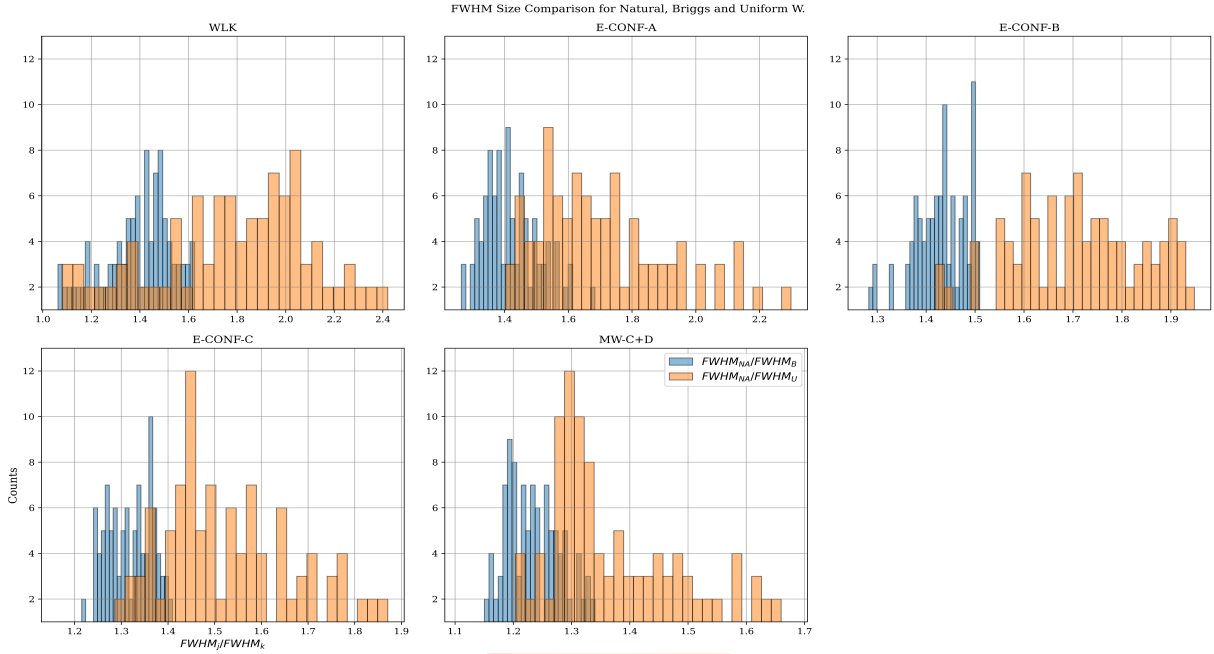


Figure 4.2.16: Size comparison of Natural/Briggs (blue) and Natural/Uniform (orange) fitted FWHM. 30 bins were used. j sub-index correspond to Natural weighting in the numerator and k sub-index corresponds to Briggs or Uniform weighting in the denominator.

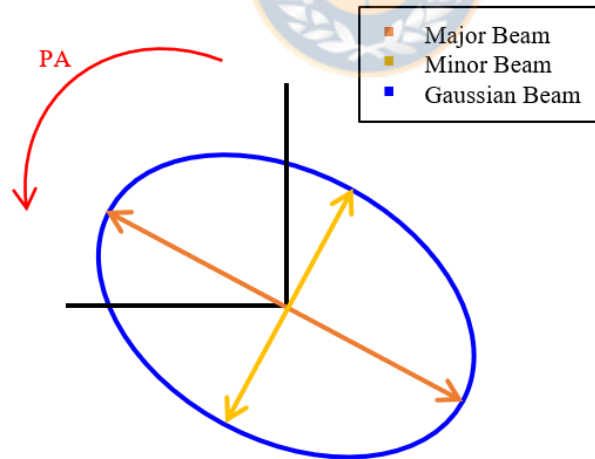


Figure 4.2.17: 2D Gaussian beam shape. P.A. means position angle.

$$\epsilon = \frac{\sqrt{\theta_{maj}^2 - \theta_{min}^2}}{\theta_{maj}}, \quad (4.2.6)$$

where θ_{maj} and θ_{min} are the major and minor synthesized beam widths, respectively. Figure 4.2.20 is a graphical representation of the evolution of the eccentricity for

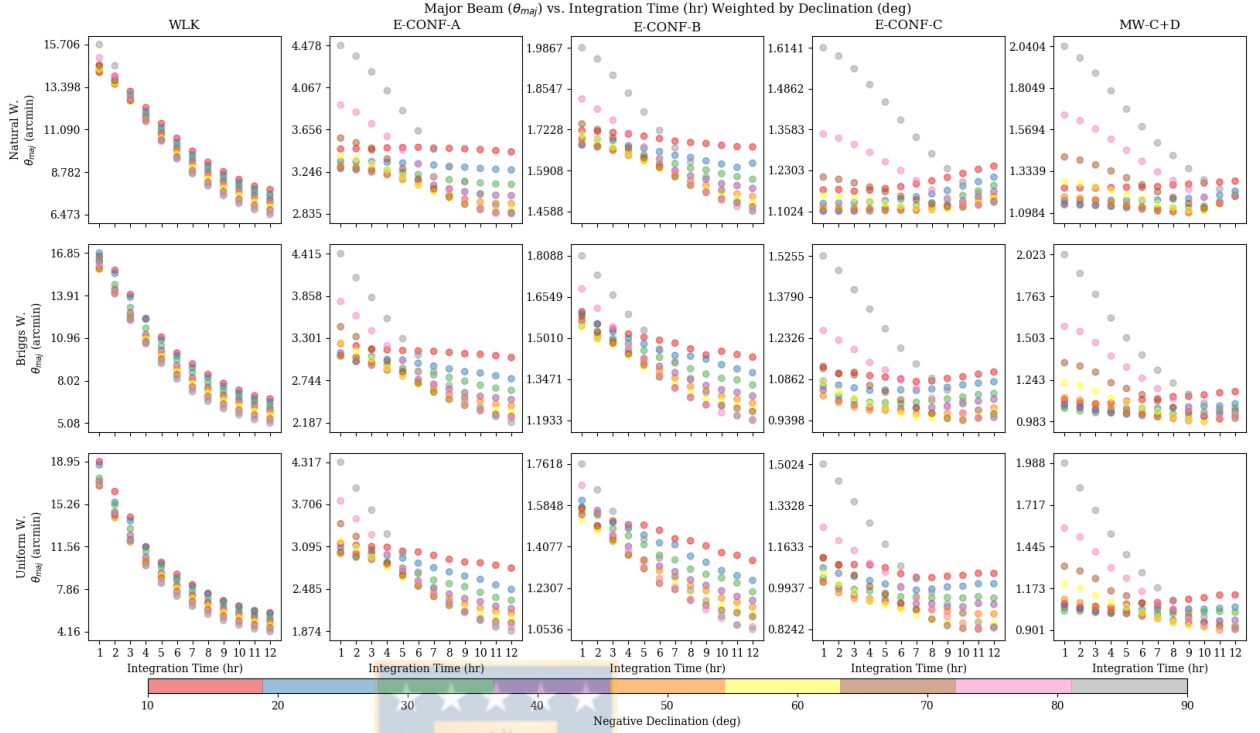


Figure 4.2.18: Major synthesized beam θ_{maj} (arcmin) evolution at 12 different integration time weighted by 9 different source declination for each configuration. First row shows the dirty major beam results, second, third and fourth rows present the Natural, Briggs (Robust = 0.5) and Uniform weighted beam, respectively. Y-axis labels in each sub-graphic start and end with the minimum and maximum value of θ_{maj} .

each array and weighting scheme. The most relevant results are the decrease of eccentricity at long integration time. Additionally, for WLK, E-CONF-A and E-CONF-B the eccentricity decrease at higher declination. However, for E-CONF-C and MW-C+D the eccentricity is higher at higher declination but at a certain points decrease rapidly to lower values close to 0.

An histogram of the fitted FWHM eccentricity is shown in Fig. 4.2.21 for each configuration and used weighting scheme. In this figure it is possible to observe that only MW-C+D array configuration has a uniform distribution eccentricity.

4.2.4.4 Dirty v/s Clean Image

Although this work did not have as an objective the study of the imaging results but only the uv-data sets and synthesized beam. Here, it is also presented a visual comparison results of the cleaned images. The analyzed results of the dirty and

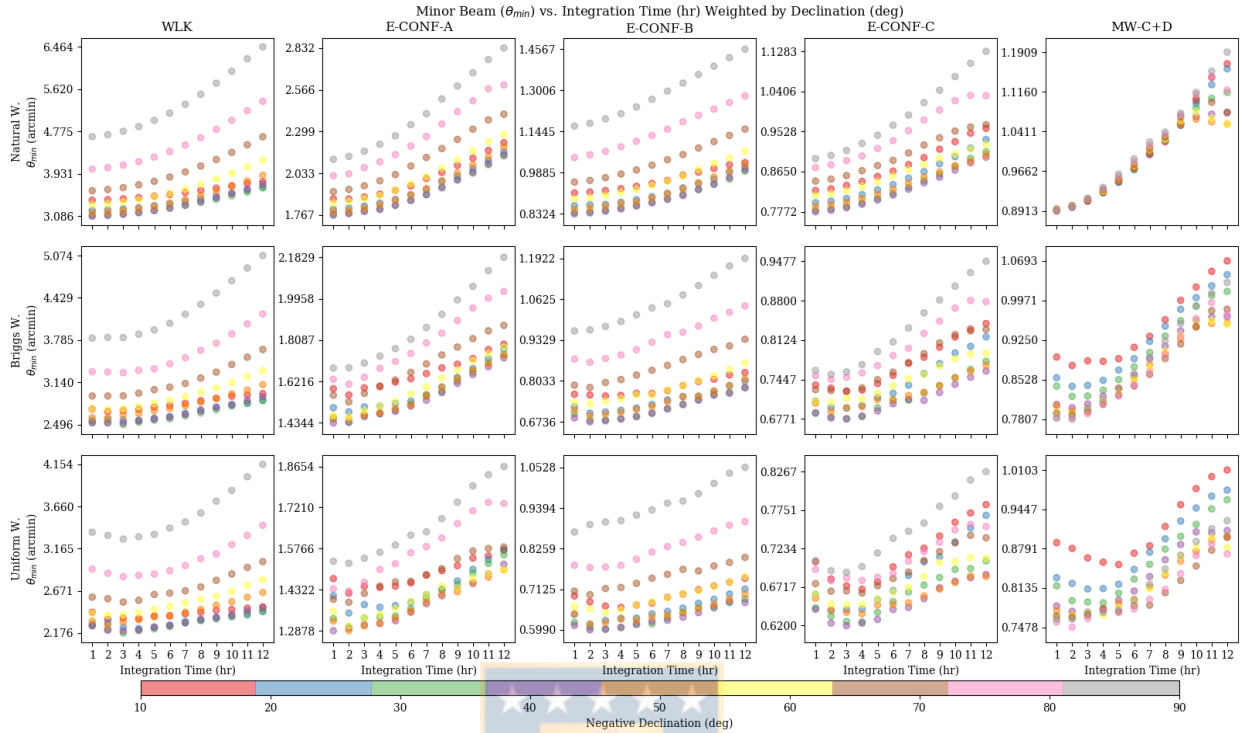


Figure 4.2.19: Minor synthesized beam θ_{min} (arcmin) evolution at 12 different integration time weighted by 9 different source declination for each configuration. First row shows the dirty major beam results, second, third and fourth rows present the Natural, Briggs (Robust = 0.5) and Uniform weighted beam, respectively. Y-axis labels in each sub-graphic start and end with the minimum and maximum value of θ_{min} .

clean images for the 5 semi-random antenna array configurations showed that when the source has a angular size of bigger than the largest angular size scale showed in table 4.2.1, the array can not resolve it and fringe patterns appears more drastically than for a source with a angular scale of a few arcmins in size, larger structure are “resolved out” and cannot be recovered.

Figure 4.2.22 shows a dirty image (a) and clean image (b) comparison at -10 deg declination after 1 hour observation using MW-C+D configuration 4.2.8. In this Fig. it is possible to notice the impact of the high side lobe levels in the dirty image and clean image. High synthetic noise is observed in Fig. (a). and in Fig. (b) both source are distinguishable from the background.

For comparison, Fig. 4.2.23 shows a dirty image (a) and clean image (b) comparison at -80 deg declination after 12 hour observation using MW-C+D configuration 4.2.8. In this Fig. it is possible to notice a reduction of noise in dirty image

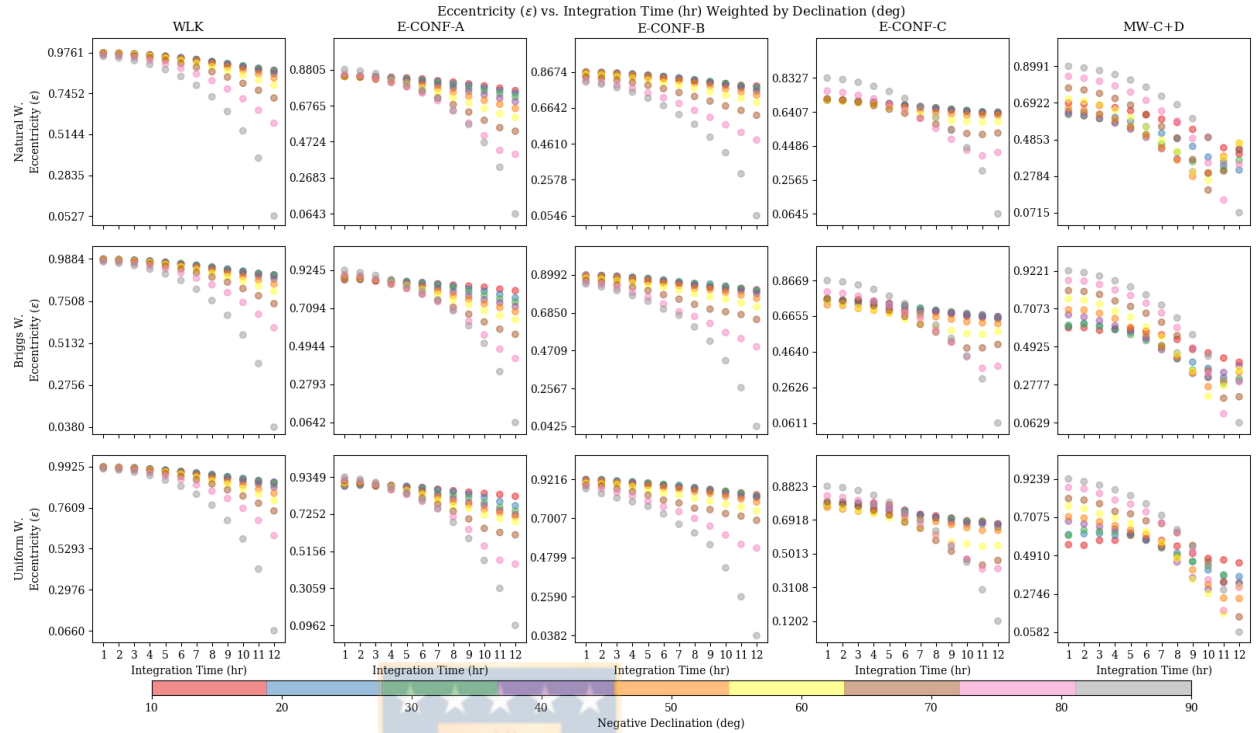


Figure 4.2.20: Eccentricity (ϵ) evolution at 12 different integration time weighted by 9 different source declination for each configuration. First row shows the dirty major beam results, second, third and fourth rows present the Natural, Briggs (Robust = 0.5) and Uniform weighted beam, respectively. Y-axis labels in each sub-graphic start and end with the minimum and maximum value of ϵ .

showed in Fig. (a). After a 500 cleaning iterations, the 2 sources are well resolved.

Additionally, Fig. 4.2.24 shows a dirty image (a) and clean image (b) comparison at -10 deg declination after 1 hour observation using WLK configuration 4.2.4. This result have the same source declination and observation time that in Fig. 4.2.22, however, it is possible to observe a less noise image in both dirty and clean images.

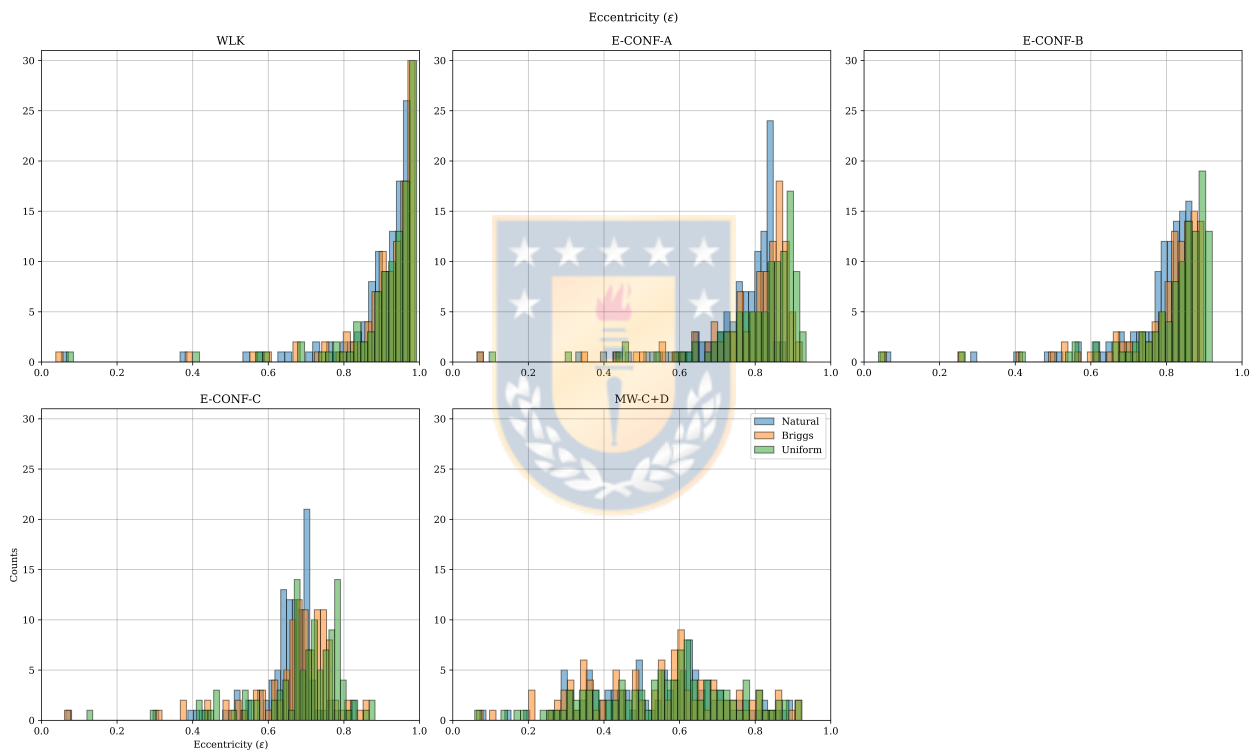


Figure 4.2.21: Histograms of the fitted beam width eccentricity for all the configurations for each weighting schemes used during the imaging process.

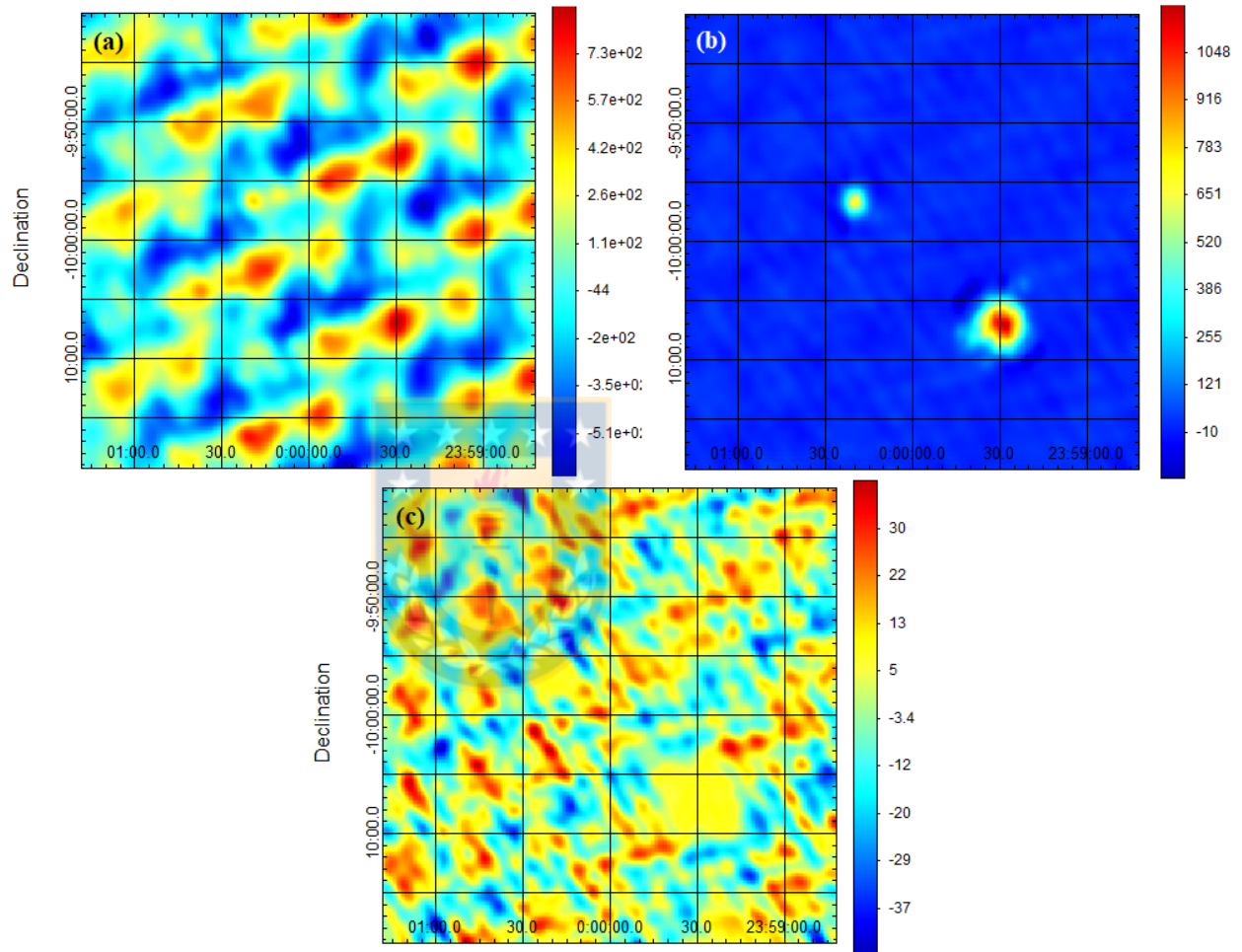


Figure 4.2.22: (a): Dirty image, i.e., real image data convolved with the Uniform weighting synthesized beam. Zero cleaning iterations applied on this image data. (b): Clean image, i.e., cleaned image after 500 iterations with the Hogbom cleaning algorithm [Högbom \(1974\)](#). (c): Residual map after cleaning. Simulations results are from the sky-model image at -10 deg in declination and 1 hour of observation only using MW-C+D configuration [4.2.8](#).

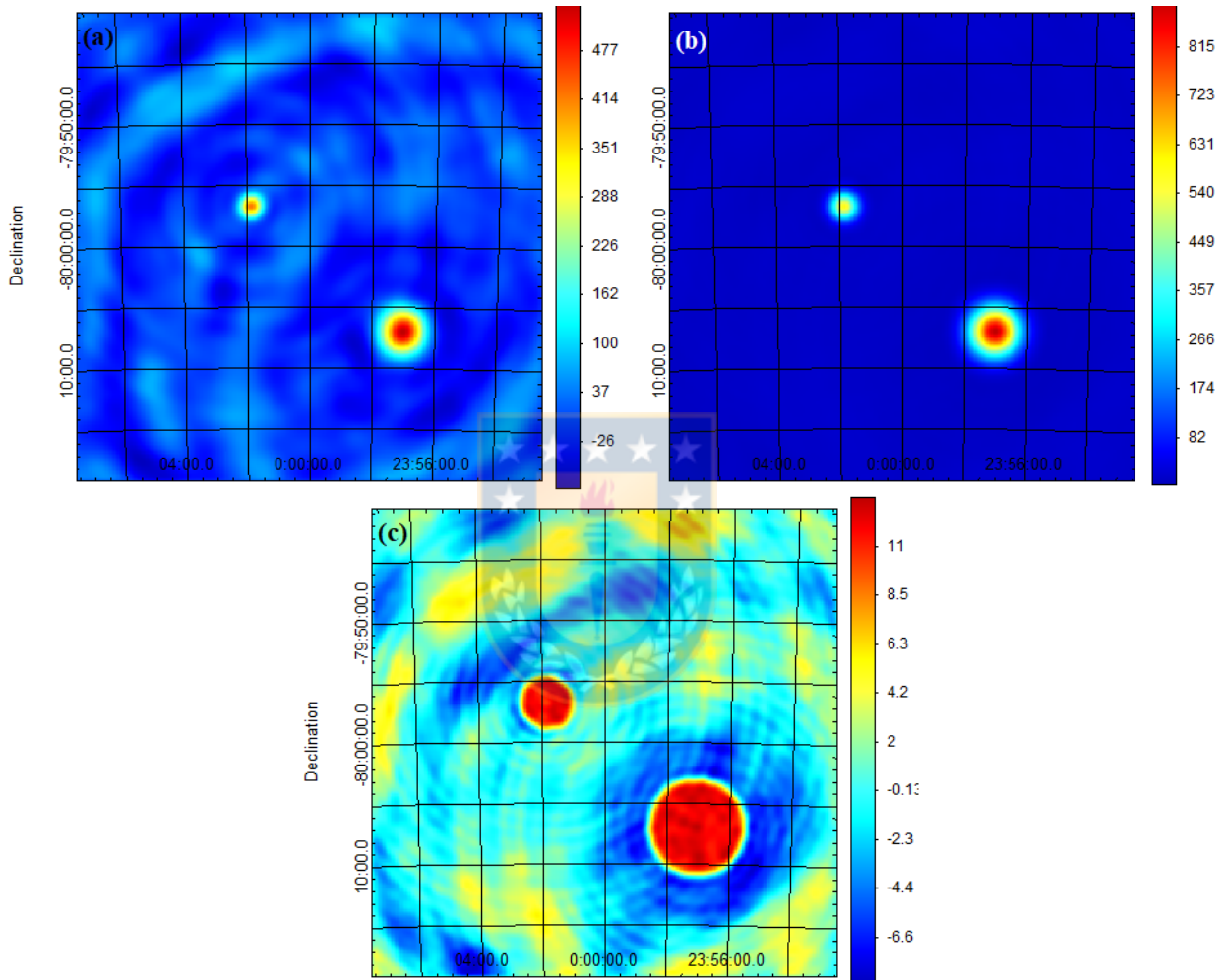


Figure 4.2.23: (a): Dirty image, i.e., real image data convolved with the Uniform weighting synthesized beam. Zero cleaning iterations applied on this image data. (b): Clean image, i.e., cleaned image after 500 iterations with the Hogbom cleaning algorithm. (c): Residual map after cleaning. Simulations results are from the sky-model image at -80 deg in declination and 12 hour of observation only using MW-C+D configuration 4.2.8.

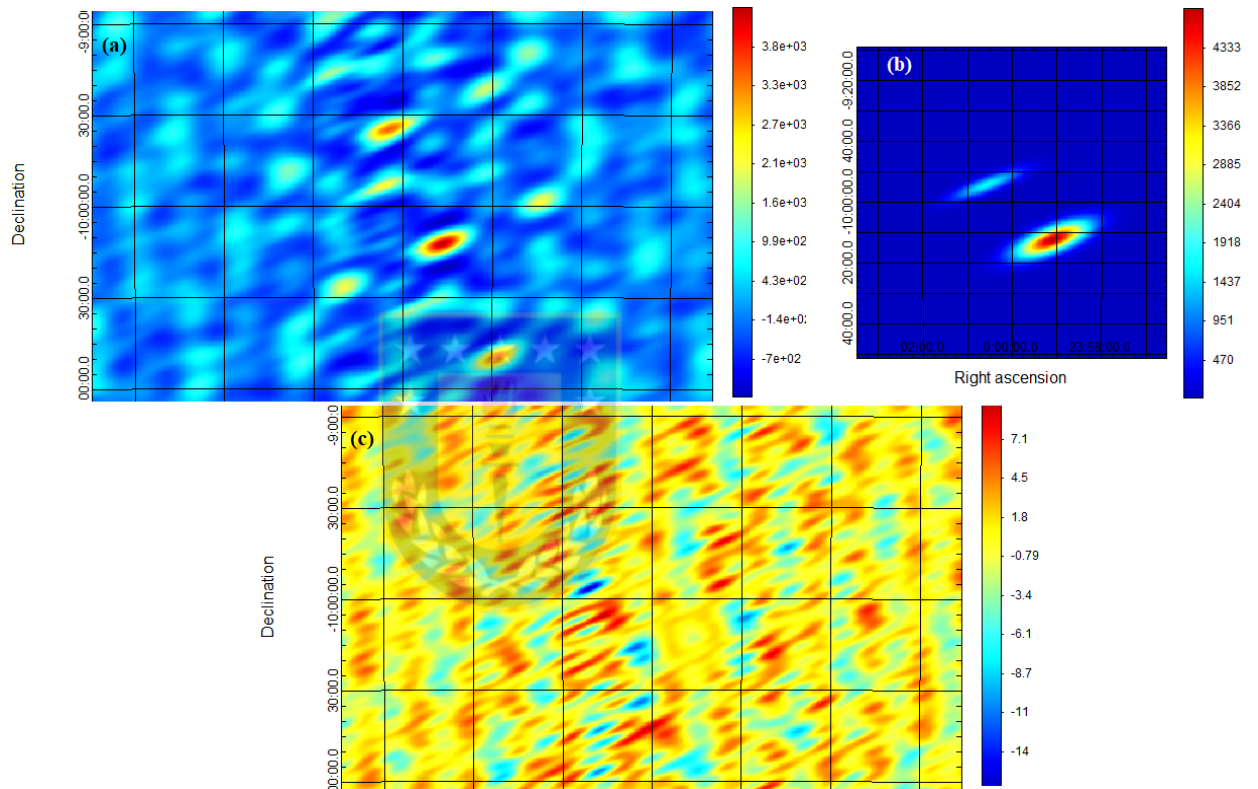


Figure 4.2.24: (a): Dirty image, i.e., real image data convolved with the Uniform weighting synthesized beam. Zero cleaning iterations applied on this image data. (b): Clean image, i.e., cleaned image after 500 iterations with the Hogbom cleaning algorithm. (c): Residual map after cleaning. Simulations results are from the sky-model image at -10 deg in declination and 1 hour of observation only using WLK configuration 4.2.4.

Chapter 5

Discussion and Conclusion

In this thesis it was presented the conceptual design of a scientific and academic dual-polarization interferometer with arc-minute resolution for galactic interstellar medium studies in a future. The proposed location is at 2 km (South-East) approximately from the astronomy department at the Universidad de Concepción. It was created and evaluated 5 antenna array configurations of 8 total 3 meters antennas. The evaluation of position, baselines, u,v plane range, Point Spread Function and eccentricity were studied through simulations using the Common Astronomy Software Applications (CASA) package. Additionally, a projection of the sensitivity of the array is presented. Also, the investigation and possible candidate of a L-band dual polarization feed antenna were presented.

5.1 Array Design Conclusions

Concerning to the employed CASA package for aperture synthesis simulation, it had a great performance with respect to the evaluated parameters. The possibility to add an own configurations and facilitates tools to create them were extremely helpful. Additionally, the possibility to edit and evaluate many parameters trough the observation simulation and later image cleaning made CASA the perfect choice for this investigation. The theoretical sensitivity results (values) were uncertain with respect to the calculation equations within CASA. However, the evolution of sensitivity had the expected decreasing curves for the different weighting schemes. In summary, the CASA package had a great performance for this conceptual design work.

Among the 5 different proposed arrays, WLK configuration has clearly the poorest angular resolution and eccentricity results. With respect to the synthesized beam widths, i.e., θ_{maj} , θ_{min} and position angle, it is obviously caused by the distance and position of each antenna and array orientation. Unfortunately, antenna position for this configuration is the most close to the center of operation qualifying it as the most possible to built. Configuration E-CONF-A and E-CONF-B had also a certain degree of elongation and side lobes. E-CONF-C configuration has the most extended baseline distance, whatsoever, MW-C+D configuration was designed by the analysis of the UV-Coverage of WLK configuration, E-CONF-C and a compact configuration referred as E-CONF-D. Among the 5 configurations, MW-C+D has an almost circular PSF.

Additionally, a more deep sensitivity approach supported with aperture efficiency calculations for the 3 meters single dish antenna and full characterization of the expected system temperatures at different conditions is crucial. However, it was observed in the sensitivity theoretical projections that the small diameter and number of antennas are very influential factors. Moreover, the targeted line and bandwidth play a crucial role in the final value. High sensitivity is extremely time demanding for these number of antennas, antenna diameter and targeted frequencies. In summary, with these first sensitivity projections, the antenna array configuration requires long observation times and the best antenna performance to achieve mJy sensitivities.

Among the 5 proposed and evaluated configurations, WLK is the most feasible to implement with respect to the position of the antennas. It has the 8 antennas in places were almost exist concrete to build them and the wiring could not be huge a problem due the proximity to the WenuLafquen operation facilities. However, only 155 meters is the most extended aperture achievable, i.e., a 5.68 arcmin maximum angular resolution with a uniform weighting scheme in the best observational scenario. A in situ work it is necessary to make a topographic study of the proposed area. This, to to make a more realistic map of the area and analyze the current area conditions.

In summary, it is possible to achieve a few arc-minutes angular resolution with a 8-antennas array at the WenuLafquen observatory and surroundings. However, the number of antennas and the area limit the configuration layout, by only resulting in semi-random configuration designs to evaluate. High observation times are the

best options in the moment to achieve arc-minutes resolutions. Source declination from -35° to -80° are the best to observe, observable during the majority of the observation time.

The development of a instrument of this magnitude is necessary to teach young astronomy students the modern radio-astronomy era that has been growing. New massive radio-astronomy observatories for aperture synthesis observations are being built around the world, e.g., next-generation VLA or Square Kilometer Array.

5.1.1 Future Work

In the future, it is intended to focus the work in the dual polarization feed system receiver for the 1.42 GHz and 1.665 GHz observation lines. During this work, a few hours of investigation were destined in designing and simulating a wave-guide with a stepped septum polarizer. It was used the ANSYS High Frequency Simulation Software (HFSS) to use with respect to the 1.42 GHz (21 cm) frequency line, it is produced by the atomic Hydrogen and detectable in the whole Universe at different temperatures.

Additionally, an array configuration optimization algorithm to optimize the synthesized beam performance could add more robustness to the project. This algorithm could be focused in minimizing the synthesized beam side lobes and finding the configuration with best angular resolution and largest angular scale performance. A starting point for this work could be the AIPS task CONFI based on the work by Kogan et al. A topographic analysis could be required to define the configuration operation range.

Continuing, Radio Frequency Interference is a disturbance caused by various sources emitting around our targeted frequencies that affect our data, introducing noise. Often RFI is stronger than the science data, and hinders signal we are after. an RFI analysis of the WLK observatory surrounding is required to evaluate the possible signal interference (noise) in the observable frequencies. The impact of RFI on astronomical observing depends on the configuration and wavelength, where RFI is primarily a problem within the low frequency bands. Also, extracting astronomy data from frequency channels in which the RFI is present is much more difficult.

Finally, data processing refers to the analog to digital process to obtain the data and reproduce real source information. This last was left as future work.



Bibliography

- (1999). *Synthesis Imaging in Radio Astronomy II*, volume 180 of *Astronomical Society of the Pacific Conference Series*.
- André, P., Men'shchikov, A., Bontemps, S., Könyves, V., Motte, F., and Schneider (2010). From filamentary clouds to prestellar cores to the stellar IMF: Initial highlights from the Herschel Gould Belt Survey. *Astronomy and Astrophysics*, 518:L102.
- Arzoumanian, D., André, P., Didelon, P., Könyves, V., Schneider, N., Men'shchikov, A., Soubie, T., Zavagno, A., Bontemps, S., di Francesco, J., Griffin, M., Hennemann, M., Hill, T., Kirk, J., Martin, P., Minier, V., Molinari, S., Motte, F., Peretto, N., Pezzuto, S., Spinoglio, L., Ward-Thompson, D., White, G., and Wilson, C. D. (2011). Characterizing interstellar filaments with Herschel in IC 5146. *Astronomy and Astrophysics*, 529:L6.
- Astropy Collaboration (2022). The Astropy Project: Sustaining and Growing a Community-oriented Open-source Project and the Latest Major Release (v5.0) of the Core Package. *Astrophysical Journal*, 935(2):167.
- Bolatto, A. D., Wolfire, M., and Leroy, A. K. (2013). The CO-to-H₂ Conversion Factor. *Annual Review of Astron and Astrophys*, 51(1):207–268.
- Brauer, R., Wolf, S., Reissl, S., and Ober, F. (2017). Magnetic fields in molecular clouds: Limitations of the analysis of Zeeman observations. *Astronomy and Astrophysics*, 601:A90.
- Carilli, C. L. (2016a). Imaging Capabilities: Protoplanetary Disks Comparison of ngVLA, JVLA, ALMA. *ngVLA MEMO*.
- Carilli, C. L. (2016b). The Strength of the Core. *ngVLA MEMO*.
- Carilli, C. L. (2017). More on Synthesized Beams and Sensitivity. *ngVLA MEMO*.
- Cazzoli, G., Lattanzi, V., Coriani, S., Gauss, J., Codella, C., Ramos, A. A., Cernicharo, J., and Puzzarini, C. (2017). Zeeman effect in sulfur monoxide. A tool to probe magnetic fields in star forming regions. *Astronomy and Astrophysics*, 605:A20.
- Crutcher, R. M. (2012). Magnetic Fields in Molecular Clouds. *Annual Review of Astron and Astrophys*, 50:29–63.

- Crutcher, R. M. and Kemball, A. J. (2019). Review of Zeeman Effect Observations of Regions of Star Formation K Zeeman Effect, Magnetic Fields, Star formation, Masers, Molecular clouds. *Frontiers in Astronomy and Space Sciences*, 6:66.
- Crutcher, R. M., Nutter, D. J., Ward-Thompson, D., and Kirk, J. M. (2004). SCUBA Polarization Measurements of the Magnetic Field Strengths in the L183, L1544, and L43 Prestellar Cores. *The Astrophysical Journal*, 600(1):279–285.
- Crutcher, R. M., Roberts, D. A., Troland, T. H., and Goss, W. M. (1999). The Magnetic Field of the NGC 2024 Molecular Cloud. *The Astrophysical Journal*, 515(1):275–285.
- Crutcher, R. M., Troland, T. H., Goodman, A. A., Heiles, C., Kazes, I., and Myers, P. C. (1993). OH Zeeman Observations of Dark Clouds. *The Astrophysical Journal*, 407:175.
- Crutcher, R. M., Wandelt, B., Heiles, C., Falgarone, E., and Troland, T. H. (2010). Magnetic Fields in Interstellar Clouds from Zeeman Observations: Inference of Total Field Strengths by Bayesian Analysis. *The Astrophysical Journal*, 725(1):466–479.
- Deo, D. and Kale, R. (2017). Simulations of imaging extended sources using the gmrt and the u-gmrt: Implications to observing strategies. *Experimental Astronomy*, 44.
- Draine, B. T. (2011). *Physics of the Interstellar and Intergalactic Medium*.
- Elmegreen, B. G. (2000). Star Formation in a Crossing Time. *The Astrophysical Journal*, 530(1):277–281.
- Falgarone, E., Troland, T. H., Crutcher, R. M., and Paubert, G. (2008). CN Zeeman measurements in star formation regions. *Astronomy and Astrophysics*, 487(1):247–252.
- Federrath, C. (2016). On the universality of interstellar filaments: theory meets simulations and observations. *Monthly Notices of the Royal Astronomical Society*, 457(1):375–388.
- Galuscak, R. (2004). Septum Feed Revisited. *DUBUS*, 4/2004.
- Greisen, E. W. (2003). AIPS, the VLA, and the VLBA. 285:109.
- Hamaker, J. P., Bregman, J. D., and Sault, R. J. (1996). Understanding radio polarimetry. I. Mathematical foundations. *Astronomy and Astrophysics, Supplement*, 117:137–147.
- Harris, C. R., Millman, K. J., van der Walt, S. J., Gommers, R., Virtanen, P., Cournapeau, D., Wieser, E., Taylor, J., Berg, S., Smith, N. J., Kern, R., Picus, M., Hoyer, S., van Kerkwijk, M. H., Brett, M., Haldane, A., del Río, J. F., Wiebe, M., Peterson, P., Gérard-Marchant, P., Sheppard, K., Reddy, T., Weckesser, W., Abbasi, H., Gohlke, C., and Oliphant, T. E. (2020). Array programming with NumPy. *Nature*, 585(7825):357–362.

- Harrison, R. E., Looney, L. W., Stephens, I. W., Li, Z.-Y., Teague, R., Crutcher, R. M., Yang, H., Cox, E. G., Fernández-López, M., and Shinnaga, H. (2021). ALMA CN Zeeman Observations of AS 209: Limits on Magnetic Field Strength and Magnetically Driven Accretion Rate. *The Astrophysical Journal*, 908(2):141.
- Haverkorn, M. (2015). Magnetic Fields in the Milky Way. In Lazarian, A., de Gouveia Dal Pino, E. M., and Melioli, C., editors, *Magnetic Fields in Diffuse Media*, volume 407 of *Astrophysics and Space Science Library*, page 483.
- Hazdra, P., Galucák, R., and Mazanek, M. (2006). Optimization of prime-focus circular waveguide feed with septum polarization transformer for 1.296 ghz eme station.
- Heiles, C. (1989). Magnetic Fields, Pressures, and Thermally Unstable Gas in Prominent H i Shells. *The Astrophysical Journal*, 336:808.
- Heiles, C. (1997). A Holistic View of the Magnetic Field in the Eridanus/Orion Region. *The Astrophysical Journals*, 111(1):245–288.
- Heiles, C. (2002). A Heuristic Introduction to Radioastronomical Polarization. In Stanimirovic, S., Altschuler, D., Goldsmith, P., and Salter, C., editors, *Single-Dish Radio Astronomy: Techniques and Applications*, volume 278 of *Astronomical Society of the Pacific Conference Series*, pages 131–152.
- Heiles, C. and Crutcher, R. (2005). Magnetic Fields in Diffuse HI and Molecular Clouds. In Wielebinski, R. and Beck, R., editors, *Cosmic Magnetic Fields*, volume 664, page 137.
- Heiles, C., Perillat, P., Nolan, M., Lorimer, D., Bhat, R., Ghosh, T., Lewis, M., O’Neil, K., Salter, C., and Stanimirovic, S. (2001). Mueller Matrix Parameters for Radio Telescopes and Their Observational Determination. *Publications of the ASP*, 113(788):1274–1288.
- Heiles, C. and Troland, T. H. (2003). The Millennium Arecibo 21 Centimeter Absorption-Line Survey. II. Properties of the Warm and Cold Neutral Media. *The Astrophysical Journal*, 586(2):1067–1093.
- Heyer, M. and Dame, T. M. (2015). Molecular Clouds in the Milky Way. *Annual Review of Astron and Astrophys*, 53:583–629.
- Högbom, J. A. (1974). Aperture Synthesis with a Non-Regular Distribution of Interferometer Baselines. *Astronomy and Astrophysics, Supplement*, 15:417.
- Hull, C. L. H. and Zhang, Q. (2019). Interferometric observations of magnetic fields in forming stars. *Frontiers in Astronomy and Space Sciences*, 6:3.
- Hunte, C. (2008). The Jones-Mueller Transformation. *Fizika A*, 17(1):51.
- Hunter, J. D. (2007). Matplotlib: A 2d graphics environment. *Computing in Science & Engineering*, 9(3):90–95.

- Kalberla, P. M. W. and Kerp, J. (2009). The HI Distribution of the Milky Way. *Annual Review of Astron and Astrophys*, 47(1):27–61.
- Kim, J., Lee, J.-W., Lee, T.-K., and Cho, C. S. (2012). Simple and efficient design method of stepped septum polarizer for x-band satellite communication.
- Klein, U. (2006). Radio astronomy: tools, applications and impacts. *Course astro 841*.
- Krumholz, M. R. (2015). Notes on Star Formation. *arXiv e-prints*, page arXiv:1511.03457.
- Leurini, S., Schisano, E., and Pillai, T. (2019). Characterising the high-mass star forming filament G351.776-0.527 with Herschel and APEX dust continuum and gas observations. *Astronomy and Astrophysics*, 621:A130.
- Mac Low, M.-M. and Klessen, R. S. (2004). Control of star formation by supersonic turbulence. *Reviews of Modern Physics*, 76(1):125–194.
- Madau, P. and Dickinson, M. (2014). Cosmic Star-Formation History. *Annual Review of Astron and Astrophys*, 52:415–486.
- Marr, J., Durkota, K., Wilkin, F., Pere, A., Rogers, A., Fish, V., Holodak, G., and Arndt, M. (2011). Demonstrating the principles of aperture synthesis with the very small radio telescope.
- McMullin, J. P., Waters, B., Schiebel, D., Young, W., and Golap, K. (2007). CASA Architecture and Applications. 376:127.
- Molinari, S., Swinyard, B., and Bally, J. (2010). Clouds, filaments, and protostars: The Herschel Hi-GAL Milky Way. *Astronomy and Astrophysics*, 518:L100.
- Mouschovias, T. C. and Ciolek, G. E. (1999). Magnetic Fields and Star Formation: A Theory Reaching Adulthood. In Lada, C. J. and Kylafis, N. D., editors, *The Origin of Stars and Planetary Systems*, volume 540 of *NATO Advanced Study Institute (ASI) Series C*, page 305.
- Mouschovias, T. C. and Morton, S. A. (1991). Ambipolar Diffusion, Cloud Cores, and Star Formation: Two-dimensional, Cylindrically Symmetric Contraction. I. The Issues, Formulation of the Problem, and Method of Solution. *The Astrophysical Journal*, 371:296.
- Nakamura, F., Kamenno, S., Kusune, T., Mizuno, I., Dobashi, K., Shimoikura, T., and Taniguchi, K. (2019). First clear detection of the CCS Zeeman splitting toward the pre-stellar core, Taurus Molecular Cloud 1. *Publications of the ASJ*, 71(6):117.
- Padoan, P. and Nordlund, Å. (1999). A Super-Alfvénic Model of Dark Clouds. *The Astrophysical Journal*, 526(1):279–294.
- Palmeirim, P., André, P., and Kirk, J. (2013). Herschel view of the Taurus

- B211/3 filament and striations: evidence of filamentary growth? *Astronomy and Astrophysics*, 550:A38.
- Price, D. C. and Smirnov, O. M. (2015). Generalized formalisms of the radio interferometer measurement equation. *Monthly Notices of the Royal Astronomical Society*, 449(1):107–118.
- Ragan, S. E., Henning, T., Tackenberg, J., Beuther, H., Johnston, K. G., Kainulainen, J., and Linz, H. (2014). Giant molecular filaments in the Milky Way. *Astronomy and Astrophysics*, 568:A73.
- Robishaw, T. and Heiles, C. (2021). The Measurement of Polarization in Radio Astronomy. In Wolszczan, A., editor, *The WSPC Handbook of Astronomical Instrumentation*, pages 127–158.
- Samek, Z. (2002). Feed for parabolic dish with circular polarization. *10th International EME Conference 2002*, Prague.
- Sarma, A. P., Brogan, C. L., Bourke, T. L., Eftimova, M., and Troland, T. H. (2013). Very Large Array OH Zeeman Observations of the Star-forming Region S88B. *The Astrophysical Journal*, 767(1):24.
- Sarma, A. P., Troland, T. H., Roberts, D. A., and Crutcher, R. M. (2000). VLA OH and H I Zeeman Observations of the NGC 6334 Complex. *The Astrophysical Journal*, 533(1):271–280.
- Sarma, A. P., Troland, T. H., and Rupen, M. P. (2002). VLA H I Zeeman Observations of Centaurus A. *The Astrophysical Journal*, 564(2):696–703.
- Schuller, F., Menten, K., Contreras, Y., G., and Weiß, A. (2009). ATLASGAL - The APEX telescope large area survey of the galaxy at 870 μm . *Astronomy and Astrophysics*, 504(2):415–427.
- Smirnov, O. M. (2011). Revisiting the radio interferometer measurement equation. I. A full-sky Jones formalism. *Astronomy and Astrophysics*, 527:A106.
- Stutz, A. M. and Gould, A. (2016). Slingshot mechanism in Orion: Kinematic evidence for ejection of protostars by filaments. *Astronomy and Astrophysics*, 590:A2.
- Thompson, A. R., Moran, J. M., and Swenson, George W., J. (2017). *Interferometry and Synthesis in Radio Astronomy, 3rd Edition*.
- Troland, T. H. and Crutcher, R. M. (2008). Magnetic Fields in Dark Cloud Cores: Arecibo OH Zeeman Observations. *The Astrophysical Journal*, 680(1):457–465.
- Vlemmings, W. H. T., Lankhaar, B., Cazzoletti, P., Ceccobello, C., Dall’Olio, D., van Dishoeck, E. F., Facchini, S., Humphreys, E. M. L., Persson, M. V., Testi, L., and Williams, J. P. (2019). Stringent limits on the magnetic field strength in the disc of TW Hya. ALMA observations of CN polarisation. *Astronomy and Astrophysics*, 624:L7.

- Wade, P. (2003). Analysis of the OK1DFC Septum Feed. *DUBUS*, 1/2003.
- Wrobel, J. M. and Walker, R. C. (1999). Sensitivity. In Taylor, G. B., Carilli, C. L., and Perley, R. A., editors, *Synthesis Imaging in Radio Astronomy II*, volume 180 of *Astronomical Society of the Pacific Conference Series*, page 171.
- Yun, M. S. (1999). Tidal Interactions in M81 Group. In Barnes, J. E. and Sanders, D. B., editors, *Galaxy Interactions at Low and High Redshift*, volume 186, page 81.



Appendix A

Radio-Polarimetry

Radio-polarimetry (RP) is the measurement of polarization radiation from distant sources using one or more radio-telescopes. Seems easy, unluckily, it is not. Below is described crucial parameters for the understanding of RP and this thesis.

A1 Polarization

In short, polarization is the evolution of the electric field vector of light. Several formalism exist to describe polarization, the application of which depending on the polarimetric principle. Lets assume monochromatic waves, i.e. they all have the same wavelength. Considering a totally polarized wave propagating in the z direction. It is mathematically described by its complex Cartesian components E_x and E_y ,

$$\vec{E}(z, t) = E_x(z, t)\hat{x} + E_y(z, t)\hat{y} \quad (\text{A1.1})$$

Where:

$$\begin{aligned} E_x(z, t) &= E_{x0} \cdot e^{i(kz - \omega t + \phi_x)} \\ E_y(z, t) &= E_{y0} \cdot e^{i(kz - \omega t + \phi_y)} \end{aligned} \quad (\text{A1.2})$$

This is the representation of a plane wave and, $k = 2\pi/\lambda$ is the wave number and $\omega = 2\pi c/\lambda$ is the angular frequency. ϕ_x and ϕ_y are the phases of the two components. This assumptions and the realization of the mathematics (full

demonstration in Klein (2006)) yields to the so called ellipse of polarization (figure A1.1) equation:

$$\left(\frac{E_x}{E_{x0}}\right)^2 + \left(\frac{E_y}{E_{y0}}\right)^2 - 2\frac{E_x \cdot E_y}{E_{x0}} \cdot E_{y0} \cdot \cos \Delta\phi = \sin^2 \Delta\phi \quad (\text{A1.3})$$

where $\Delta\phi = \phi_y - \phi_x$ is the phase difference between the oscillating components of \vec{E} . The equation A1.3 describes an elliptically polarized wave, i.e. the tip of the \vec{E} vector sweeps out an ellipse perpendicular to the z-direction. In this most general situation, the partial waves have a relative phase lag $\Delta\phi$.

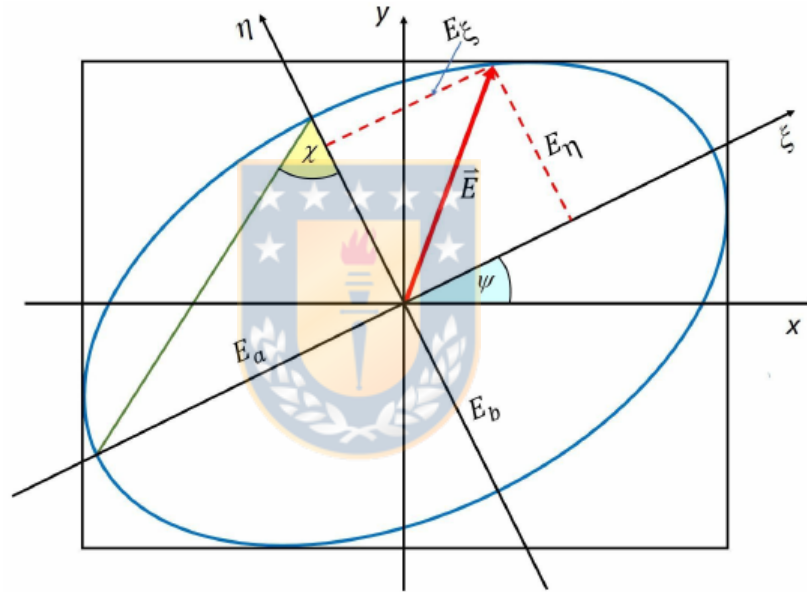


Figure A1.1: Polarization Ellipse

From figure A1.1, it presents different angles and vectors and their relation with the Cartesian components are:

$$\tan 2\psi = \frac{2E_{x0} \cdot E_{y0}}{E_{x0}^2 - E_{y0}^2} \cdot \cos \Delta\phi \quad (\text{A1.4})$$

It is also possible to use circular basis representation of $\vec{E}(z, t)$. This is very useful when circular polarization is necessary.

$$\begin{aligned}
E_r(z, t)\hat{\mathbf{r}} &= E_{r0} \left(\frac{\hat{\mathbf{x}} - i\hat{\mathbf{y}}}{\sqrt{2}} \right) \cdot e^{i(kz - \omega t + \phi_r)} \\
E_l(z, t)\hat{\mathbf{l}} &= E_{l0} \left(\frac{\hat{\mathbf{x}} + i\hat{\mathbf{y}}}{\sqrt{2}} \right) \cdot e^{i(kz - \omega t + \phi_l)}
\end{aligned} \tag{A1.5}$$

Using this representation, then putting the Cartesian basis and circular basis together, it was possible to made a "hybrid" representation of $\vec{\mathbf{E}}(z, t)$:

$$\vec{\mathbf{E}}(z, t) = (E_r + E_l) \frac{\hat{\mathbf{x}}}{\sqrt{2}} + i(E_l - E_r) \frac{\hat{\mathbf{y}}}{\sqrt{2}} \tag{A1.6}$$

where

$$\begin{aligned}
E_r &= E_{r0} e^{i(kz - \omega t + \phi_r)} \\
E_l &= E_{l0} e^{i(kz - \omega t + \phi_l)}
\end{aligned} \tag{A1.7}$$

This will be used to demonstrate the Stokes parameters in circular basis in section [A2.1](#).

Returning to the definition of polarization, exist 3 types of polarization: *linear*, *circular* and *elliptical* polarization, where the last one is the most common form of polarization. In the following items, is explained the 3 types of polarization.

- Linear Polarization:

Continuing with the representation of the components of the electric field given above, linear polarization happen when the two components non zero of $\vec{\mathbf{E}}$ i.e. x and y have no phase difference, but the magnitude of the components are not necessarily equal. When $E_y = 0$, we said that our wave is horizontally linear polarized or is said to be linear polarized in the x direction. When $E_x = 0$, we said that our wave is vertically linear polarized or is said to be linear polarized in the y direction. However, the most common form is when E_x and E_y are different from zero (figure [A1.2](#)). Also, linear polarization oscillates in a single direction.

- Circular Polarization:

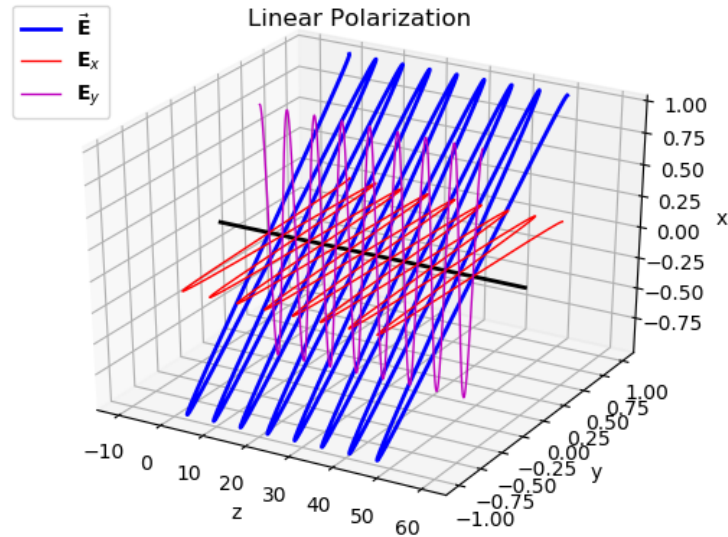
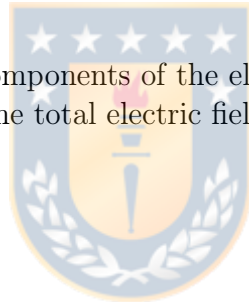


Figure A1.2: The two components of the electric field oscillating in the x and y plane in the z direction. The total electric field is the blue line and forms a line in the xy plane.



Circular polarization happens when the magnitude (amplitude) of the two orthogonal components of E are equal and the phase difference is 90° or -90° (270°). When the phase difference is equal to 90° , the electric field of light is right circular polarized and the tip of \vec{E} draws a circle in the xy plane through time in a counter clockwise direction (figure A1.3). But, when the phase difference is -90° the electric field of light is left circular polarized and the tip of \vec{E} draws a circle in the xy plane through time in a clockwise direction (figure A1.3).

(figure A1.3)

- Elliptical Polarization:

When the above conditions are not observed, we say that our field is elliptically polarized. That is, the phase difference is not a multiple of 90° nor zero. Here, the tip of the \vec{E} draws an ellipse in the xy plane, in counter clockwise or clockwise direction (figure A1.4).

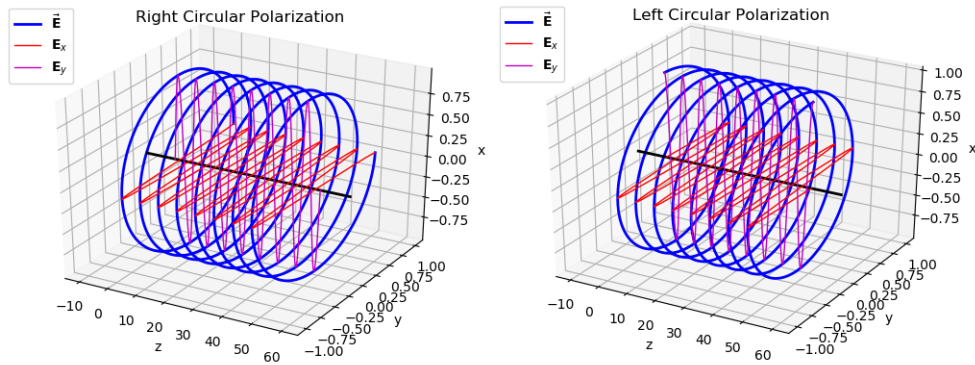


Figure A1.3: The two components of the electric field oscillating in the x and y plane in the z direction with the same magnitude (amplitude) but with a 90° phase. The total electric field forms a helix that moves through time in the z direction and draw a circle in the xy plane.

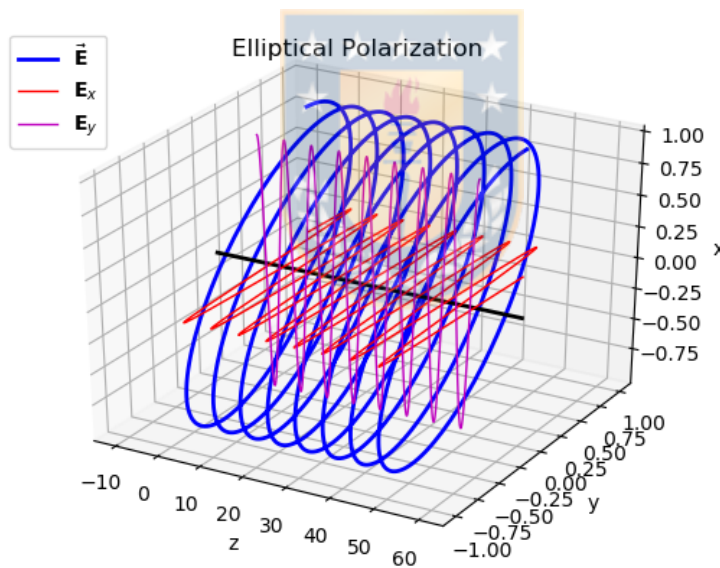


Figure A1.4: The total electric field forms an elliptical helix that moves through time in the z direction and draw an ellipse in the xy plane.

This representation is useful to have a first understanding of polarization, however, it is necessary to add more elements to achieve the observation of polarization. Above is presented the electric field representation of polarization, which is the one used in radioastronomy.

A2 Techniques For Working With Polarization

Here, techniques are referred to all the mathematics and physics that is applied to manage polarization. In general, these techniques are of big importance in radio-polarimetry, the field in radio-astronomy that is in charge to measure polarization from distant sources using radio telescopes.

A2.1 Stokes Parameters

To have a visible and mathematical representation of polarization in the ellipse of polarization or in the plane of polarization, is used the Electric Field components as shown in section X. Astronomers are never interested in E , just because E is transformed in Power i.e the time average of E . The Stokes parameters were defined by *George Gabriel Stokes* in 1852 as a set of four parameters that describe the polarization state of electromagnetic radiation which all denote radiant energy per unit time, unit frequency interval, unit (detector or collector) area (and for extended sources: per unit solid angle) and were named *Stokes Parameters* by *Subrahmanyan Chandrasekhar* in 1947. The Stokes parameters are the elements of the Stokes 1×4 column matrix \mathbf{S} and poses all the information about the different types of polarization of the radiation, i.e. it is fully linear vertical polarized, Left Hand Polarized, etc, but not the absolute phase of the wave.

$$\mathbf{S} = \begin{pmatrix} I \\ Q \\ U \\ V \end{pmatrix} = \begin{pmatrix} S_0 \\ S_1 \\ S_2 \\ S_3 \end{pmatrix} \quad (\text{A2.1})$$

- Stokes I or S_0

This parameter poses the information about the total intensity of the wave but does not store any polarization information. Is represented by the sum of any 2 orthogonal intensities or by the sum of $\langle E_x E_x^* \rangle$ and $\langle E_y E_y^* \rangle$, where the bracket means time average. The last representation are the Stokes parameters expressed in terms of electric fields, is used in radio astronomy and in the representation, is used the Cartesian basis XY of the electric field but also is possible to use the Circular basis RL , so:

$$\begin{aligned}
I &= I_{90^\circ} + I_{0^\circ} = I_{45^\circ} + I_{135^\circ} = I_{RCP} + I_{LCP} = \langle E_x E_x^* \rangle + \langle E_y E_y^* \rangle \\
&= \langle E_r E_r^* \rangle + \langle E_l E_l^* \rangle
\end{aligned} \tag{A2.2}$$

where $*$ denotes complex conjugate of E_p for $p = \{x, y\}$ or $\{r, l\}$ and $i = \sqrt{-1}$.

Using equation A1.6 and eliminating the average notation to avoid a mess. The demonstration in electric field representation in circular basis of Stokes I and the other 3 will be with the following results:

$$\begin{aligned}
E_x E_x^* &= \frac{1}{2} (E_r E_r^* + E_l E_l^* + E_r E_l^* + E_l E_r^*) \\
E_y E_y^* &= \frac{1}{2} (E_r E_r^* + E_l E_l^* - E_r E_l^* - E_l E_r^*) \\
E_x E_y^* &= i \frac{1}{2} (E_r E_r^* - E_l E_l^* - E_r E_l^* + E_l E_r^*) \\
E_y E_x^* &= -i \frac{1}{2} (E_r E_r^* - E_l E_l^* + E_r E_l^* - E_l E_r^*)
\end{aligned} \tag{A2.3}$$

So for Stokes I from equation A2.2 and using A2.3:

$$\begin{aligned}
E_x E_x^* + E_y E_y^* &= \frac{1}{2} (E_r E_r^* + E_l E_l^* + E_r E_l^* + E_l E_r^*) \\
&\quad + \frac{1}{2} (E_r E_r^* + E_l E_l^* - E_r E_l^* - E_l E_r^*) \\
&= E_r E_r^* + E_l E_l^*
\end{aligned} \tag{A2.4}$$

Stokes I parameter can only be positive but the remaining three parameters don't.

- Stokes Q or S_1

Stokes Q is the difference in intensities between horizontal and vertical linearly polarized components and is a measure of the tendency of the wave to prefer the horizontal direction. If $Q > 0$ there is an excess of polarized radiation along the horizontal, while for $Q < 0$, there is a vertical excess. In the XY basis, Q is the rest but in RL basis is different. So:

$$Q = I_{90^\circ} - I_{0^\circ} = \langle E_x E_x^* \rangle - \langle E_y E_y^* \rangle = \langle E_R E_L^* \rangle + \langle E_L E_R^* \rangle \quad (\text{A2.5})$$

and the demonstration for the circular basis representation is

$$\begin{aligned} E_x E_x^* - E_y E_y^* &= \frac{1}{2} (E_r E_r^* + E_l E_l^* + E_r E_l^* + E_l E_r^*) \\ &+ \frac{1}{2} (E_r E_r^* + E_l E_l^* - E_r E_l^* - E_l E_r^*) \\ &= E_r E_l^* + E_l E_r^* \end{aligned} \quad (\text{A2.6})$$

- Stokes U or S_2

Stokes U is the difference in intensities between linearly polarized components at 45° and -45° and represents the preference of the light to be aligned at 45 degrees, with $U < 0$ meaning an excess in linear polarization at an angle -45° to the horizontal.

$$U = I_{45} - I_{-45} = \langle E_x E_y^* \rangle + \langle E_y E_x^* \rangle = -i(\langle E_r E_l^* \rangle - \langle E_l E_r^* \rangle) \quad (\text{A2.7})$$

Continuing with the demonstration in circular basis representation

$$\begin{aligned} E_x E_y^* + E_y E_x^* &= i \frac{1}{2} (E_r E_r^* - E_l E_l^* - E_r E_l^* + E_l E_r^*) \\ &- i \frac{1}{2} (E_r E_r^* - E_l E_l^* + E_r E_l^* - E_l E_r^*) \\ &= -i(E_r E_l^* - E_l E_r^*) \end{aligned} \quad (\text{A2.8})$$

- Stokes V or S_3

This Stokes Parameter indicates the degree of Circular Polarization (CP) of \vec{E} and is defined as the Right CP minus Left CP Intensity (by the *Institute of Electrical and Electronics Engineers* and the *International Astronomical Union*), with values between -1 and 1. Exists two types of CP, Left and Right Circular Polarization. When Stokes V is negative, E is Left circular

polarized and when Stokes V is positive, E is Right circular polarized. How, Stokes Parameters are used when

$$V = I_{RCP} - I_{LCP} = i(\langle E_x E_y^* \rangle - \langle E_y E_x^* \rangle) = \langle E_r E_r^* \rangle - \langle E_l E_l^* \rangle \quad (\text{A2.9})$$

and the demonstration for the circular basis representation is

$$\begin{aligned} i(E_x E_y^* - E_y E_x^*) &= i \frac{1}{2} (E_r E_r^* - E_l E_l^* - E_r E_l^* + E_l E_r^*) \\ &+ i \frac{1}{2} (E_r E_r^* - E_l E_l^* + E_r E_l^* - E_l E_r^*) \quad (\text{A2.10}) \\ &= E_r E_r^* - E_l E_l^* \end{aligned}$$

The polarization can be represented graphically on the Poincare Sphere [A2.1](#)

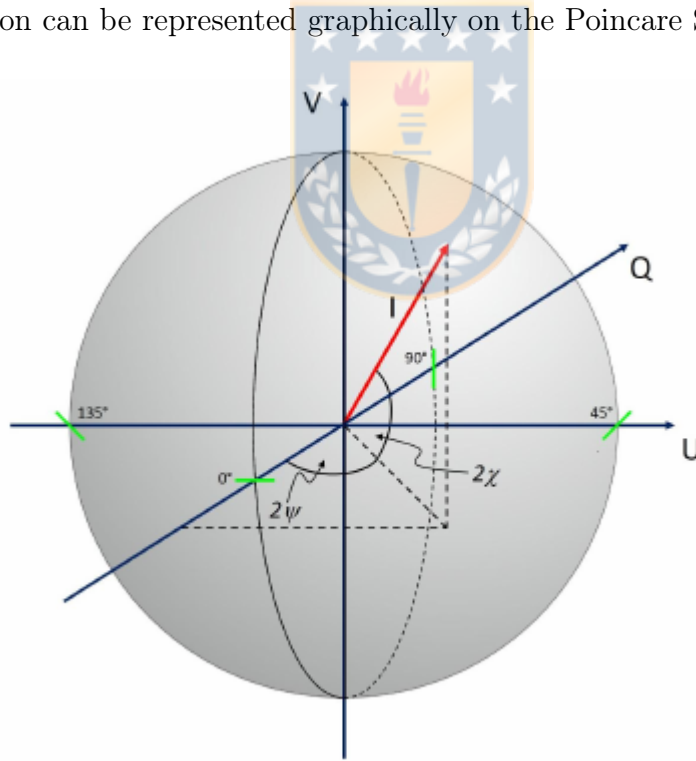


Figure A2.1: The Poincare sphere

Finally, there exist a few relations between the Stokes parameters that are always used in astronomical analysis, this are:

$$\chi = \frac{1}{2} \arctan \left(\frac{U}{Q} \right) \quad (\text{A2.11})$$

which is the polarization angle (figure A2.2) and is measured from north to east, and,

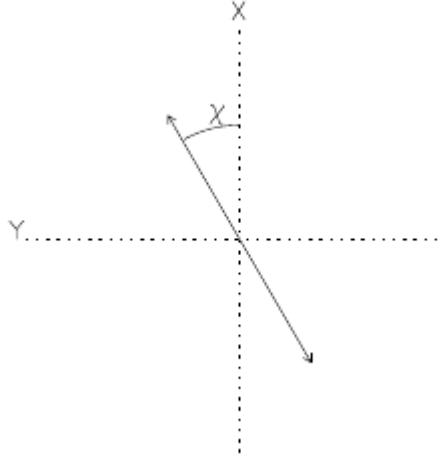


Figure A2.2: The polarization angle χ is measured from X to Y, or from North to East. In dust polarization observation, this angle gives the orientation of the plane-on-the-sky magnetic field component, i.e, morphology.

$$\begin{aligned}
 p_{tot} &= \frac{\sqrt{Q^2 + U^2 + V^2}}{I} \\
 p_{lin} &= \frac{\sqrt{Q^2 + U^2}}{I} \\
 p_{cir} &= \frac{V}{I}
 \end{aligned} \tag{A2.12}$$

are the degree of total, linear and circular polarization, respectively. Notice that V can be positive or negative, so this implies that $p_{circ} < 0$ for a wave with pure RHC polarization and $p_{circ} > 0$ for one with pure LHC polarization.

A2.2 Jones Formalism

Formulated by *Robert Clark Jones* in 1941, Jones formalism or better know as Jones calculus is commonly used when the polarization state is fully polarized. Light which is randomly polarized, partially polarized, or incoherent must be treated using Mueller calculus (section A2.3). In this formalism, polarized light is represented by a 1×2 Jones column vector \mathbf{j} which contain the phase and amplitude of the transverse waves and can be complex:

$$\mathbf{j} = \begin{pmatrix} E_x \\ E_y \end{pmatrix} = \begin{pmatrix} E_{x0}e^{i\phi_x} \\ E_{y0}e^{i\phi_y} \end{pmatrix} \quad (\text{A2.13})$$

With this form, is possible to represent the monochromatic electric field wave moving in the z direction $\vec{\mathbf{E}}(z, t)$ by only adding the frequency and wave number

$$\vec{\mathbf{E}}(z, y) = \mathbf{j}e^{i(kz-\omega t)} = \begin{pmatrix} E_{x0}e^{i\phi_x} \\ E_{y0}e^{i\phi_y} \end{pmatrix} e^{i(kz-\omega t)} \quad (\text{A2.14})$$

Examples of Jones vectors are presented in table [A2.1](#).

Polarization	Jones Vector
Horizontally polarized	$\begin{pmatrix} 1 \\ 0 \end{pmatrix}$
Vertically polarized	$\begin{pmatrix} 0 \\ 1 \end{pmatrix}$
Linear polarized at 45° from the x axis	$\frac{1}{\sqrt{2}} \begin{pmatrix} 1 \\ 1 \end{pmatrix}$
Linear polarized at -45° from the x axis	$\frac{1}{\sqrt{2}} \begin{pmatrix} 1 \\ -1 \end{pmatrix}$
Right-hand circular polarized	$\frac{1}{\sqrt{2}} \begin{pmatrix} 1 \\ -i \end{pmatrix}$
Left-hand circular polarized	$\frac{1}{\sqrt{2}} \begin{pmatrix} 1 \\ i \end{pmatrix}$

Table A2.1: The 6 common normalized Jones vectors used to represent fully polarized light.

Now, what happen when the polarized light represented by a Jones vector enters to an optical system, well, linear optical elements are represented by 2×2 Jones matrices \mathbf{J} that act on the Jones vectors defined above and exist a set of this matrices that depends on the optical needs, e.g., polarizer, phase retarders and rotators matrices that are implemented by various optical elements such as lenses, beam splitters, mirrors, etc. The representation of the Jones matrix is:

$$\mathbf{J} = \begin{pmatrix} J_{00} & J_{01} \\ J_{10} & J_{11} \end{pmatrix} \quad (\text{A2.15})$$

where the elements J_{ij} $i, j = 0, 1$ can be complex. One example of an optical

element are the polarizer that only pass one type of polarization, i.e., a linear polarizer (LP) only pass linear polarization:

$$\mathbf{J}_{\text{LP}} = \begin{pmatrix} 1 & 0 \\ 0 & 0 \end{pmatrix} \quad (\text{A2.16})$$

The operation of Jones vector and matrix is:

$$\mathbf{j}_{in} = \mathbf{J}\mathbf{j}_{out} = \begin{pmatrix} J_{00} & J_{01} \\ J_{10} & J_{11} \end{pmatrix} \begin{pmatrix} E_x \\ E_y \end{pmatrix} \quad (\text{A2.17})$$

so, for a linear polarizer (LP):

$$\mathbf{j}_{in} = \mathbf{J}_{\text{LP}}\mathbf{j}_{out} = \begin{pmatrix} 1 & 0 \\ 0 & 0 \end{pmatrix} \begin{pmatrix} E_x \\ E_y \end{pmatrix} = E_x \quad (\text{A2.18})$$

obtaining only the x component that correspond to a linear vertical polarized wave. Furthermore, a very useful Jones matrix is the phase retarder matrix, which characterizes the phase delays that can produce an optical element and is

$$\mathbf{J}_{PR} = e^{i\phi} \begin{pmatrix} J_{00} & J_{01} \\ J_{10} & J_{11} \end{pmatrix} \quad (\text{A2.19})$$

where ϕ is the phase retarder. One example is a phase retarder with fast axis equal to the x- or y-axis that has zero off-diagonal terms and thus can be conveniently expressed as

$$\begin{pmatrix} e^{i\phi_x} & 0 \\ 0 & e^{i\phi_y} \end{pmatrix} \quad (\text{A2.20})$$

where ϕ_x and ϕ_y are the phase offsets of the electric fields in x and y directions respectively.

The understanding of Jones formalism is of critical importance when it is intended to understand how single dish and interferometric observations of polarization are achieved. Jones matrices are used to represent the different elements that

affect (instrumental polarization) the radiation (represented by the Jones vector) path, i.e., since this comes from the source, pass through the atmosphere, enter to the antenna and so on. Astronomers already know which elements affect the radiation, so, mostly of the work here is to characterize these effects and "subtract" them from the measured radiation (perturbed) to obtain the observed (real) radiation. In principle, this idea looks very simple, however, it is not at all, this is the most complex part in polarization observations in radioastronomy, because, beforehand we know the form that the Jones matrices have, but not the values of the components, also, these values can be complex. This final part of subtraction is done with your raw data, mostly in the part of reduction and calibration. Softwares like CASA [McMullin et al. \(2007\)](#) (Common Astronomy Software Applications) or AIPS++ [Greisen \(2003\)](#) (Astronomical Image Processing System ++) follow these steps to achieve polarization imaging and spectrum analysis for interferometric observations (CASA contains functions for single dish observations), however it is the astronomer's duty to use well these softwares.

A2.3 Mueller Formalism

The Mueller formalism (Mueller 1948, Shurcliff 1962) or Mueller calculus is used in the presence of a non fully polarized electromagnetic wave and Stokes parameters measurement. The Mueller matrix is a 4×4 matrix that characterizes the instrumental polarization produced by the different elements in the optical instrument. Moreover, these Mueller matrices are able to describe polarization (e.g. by a polarizer), retardance (e.g. by a wave plate), as well as depolarization. The importance to know the Mueller matrix for the elements is because knowing which element produces more instrumental polarization and what Stokes parameter is more affected permits, in principle, to calibrate the observations and obtain the real values of \mathbf{S}_{in} . The modification of the Stokes vectors are described by the expression

$$\mathbf{S}_{out} = \mathbf{M} \cdot \mathbf{S}_{in} \quad , \quad (\text{A2.21})$$

where \mathbf{S}_{in} is the Stokes matrix that enters the instrument, \mathbf{M} is the Mueller matrix for an element in the system and \mathbf{S}_{out} is the Stokes matrix affected by instrumental polarization. The general structure of a Mueller matrix is described

by

$$\mathbf{M} = \begin{pmatrix} m_{II} & m_{QI} & m_{UI} & m_{VI} \\ m_{IQ} & m_{QQ} & m_{UQ} & m_{VQ} \\ m_{IU} & m_{QU} & m_{UU} & m_{VU} \\ m_{IV} & m_{QV} & m_{UV} & m_{VV} \end{pmatrix} \quad (\text{A2.22})$$

$$= \begin{pmatrix} I \rightarrow I & Q \rightarrow I & U \rightarrow I & V \rightarrow I \\ I \rightarrow Q & Q \rightarrow Q & U \rightarrow Q & V \rightarrow Q \\ I \rightarrow U & Q \rightarrow U & U \rightarrow U & V \rightarrow U \\ I \rightarrow V & Q \rightarrow V & U \rightarrow V & V \rightarrow V \end{pmatrix} ,$$

The $[i, j]$ ($i, j = I, Q, U$ and V) element merely describes the transmission of the polarization-modifying element(s), and becomes 1 when using normalized Stokes vectors. Mueller matrices of a train of optical elements are multiplicative, but non-commutative

$$\mathbf{S}_{out} = \mathbf{M}_n \mathbf{M}_{n-1} \mathbf{M}_{n-2} \cdots \mathbf{M}_2 \mathbf{M}_1 \cdot \mathbf{S}_{in} \quad \text{not} \quad \mathbf{M}_1 \mathbf{M}_2 \cdots \mathbf{M}_{n-1} \mathbf{M}_n \cdot \mathbf{S}_{in}$$

$$= \mathbf{M}_T \mathbf{S}_{in} \quad , \quad (\text{A2.23})$$

where M_1 is the Mueller matrix of the first element that the radiation encounters and so on. Finally, when we measure the total Mueller matrix \mathbf{M}_T of our instrument, we must multiply the inverse of the total Mueller matrix with \mathbf{S}_{out} to obtain \mathbf{S}_{in} because what we obtain is \mathbf{S}_{out} matrix but not \mathbf{S}_{in} . This can be better understand this way: We are measuring radiation from our source but this radiation is modify by the elements and what we finally obtain is \mathbf{S}_{out} , so to obtain \mathbf{S}_{in} , must be calculated the inverse total Mueller matrix and multiply by \mathbf{S}_{out} , and that is

$$\mathbf{S}_{in} = \mathbf{M}_T^{-1} \mathbf{S}_{out} \quad , \quad (\text{A2.24})$$

where \mathbf{M}_T^{-1} is the inverse matrix of the total Mueller matrix \mathbf{M}_T . The understanding of Mueller formalism is important to understand what elements are affecting the radiation and how subtract them to obtain the real signal, however, this formalism is more used when single dish observations are made. Mueller

formalism can or can not be used in the interferometric equation [A4](#), because the current representation uses Jones formalism. The main difference is that in the Mueller formalism appears a column matrix and in the Jones formalism appears a 2×2 matrix, i.e., both contains the same information but expressed in different forms. This matrix is commonly referred as visibility vector or matrix, respectively. A focused explanation of the expressed before is presented in [A4](#).

A2.4 Linear and Circular Basis

A crucial concept to have in consideration when you are working with this two formalism is that the vector and matrices are going to be different depending of the basis that your are working on, this is related with the nature of your receiving system, that is, the feed or antennas that receive the polarized radiation. Antennas can have any type of feed system, e.g., sometimes communication antennas use LC polarization antennas to only emits and receive radiation that is LC polarized, and no other, making the communication more selective and confidential or any other reason. The majority of the high level radio telescopes around the world have what is know as a dual-polarization feed system, and is basically two antennas, one sensitive to polarization A, and the other one sensitive to polarization B, where A and B are orthogonal. This A and B differentiation is because exist to types of dual-polarization feed systems, circular and linear. E.g., dual-circular polarization feed systems have antenna A sensitive to right-circular polarization and B sensitive to left-circular polarization. Using the equations [A2.2](#), [A2.5](#), [A2.7](#) and [A2.9](#), is possible to obtain the stokes parameters. The other system is a dual-linear polarization feed system, with one antenna sensitive to horizontal polarization and the other one sensitive to vertical polarization. Example of a circular-dual polarization system is the one that the VLA observatory has implemented in the antennas and for linear-dual polarization system is ALMA antennas. This mode of operation when is called full polarization. So, in summary, Stokes parameters for both feed system are obtained as follow:

Linear System:

$$\begin{pmatrix} I \\ Q \\ U \\ V \end{pmatrix} = \begin{bmatrix} XX^* + YY^* \\ XX^* - YY^* \\ XY^* + YX^* \\ i(XY^* - YX^*) \end{bmatrix} \quad (\text{A2.25})$$

Circular System:

$$\begin{pmatrix} I \\ Q \\ U \\ V \end{pmatrix} = \begin{bmatrix} RR^* + LL^* \\ RL^* + LR^* \\ -i(RL^* - LR^*) \\ RR^* - LL^* \end{bmatrix} \quad (\text{A2.26})$$

Notice the permutation of obtaining Stokes Q, U and V. Stokes V is obtained now by the difference of the auto-correlated voltages, Stokes Q is now the sum of the cross-correlated voltages and Stoke U is the difference of the cross-correlated voltages, i.e, $V \rightarrow Q \rightarrow U \rightarrow V$. This happens because is added a 90° phase. This big difference will be also observed in the Jones and Mueller matrices for the respective type of RF system.

A2.5 Jones to Mueller matrix

A Mueller matrix is suited to all types of optical systems, while a Jones matrix completely characterizes the polarization properties of non-depolarizing optical systems. Hence, for a non-depolarizing optical system, Jones matrices and Mueller matrices are equivalent (full demonstration in [Hunte \(2008\)](#)). Below is presented the final result of [Hunte \(2008\)](#) to transform from the 2×2 Jones matrix to the 4×4 Mueller matrix:

$$\begin{aligned}
M &= U[(J \otimes J^*)U^{-1}] \\
&= \frac{1}{\sqrt{2}} \begin{pmatrix} 1 & 0 & 0 & 1 \\ 1 & 0 & 0 & -1 \\ 0 & 1 & 1 & 0 \\ 0 & -i & i & 0 \end{pmatrix} \left[\begin{pmatrix} J_{00}J_{00}^* & J_{00}J_{01}^* & J_{01}J_{00}^* & J_{01}J_{01}^* \\ J_{00}J_{10}^* & J_{00}J_{11}^* & J_{01}J_{10}^* & J_{01}J_{11}^* \\ J_{10}J_{00}^* & J_{10}J_{01}^* & J_{11}J_{00}^* & J_{11}J_{01}^* \\ J_{10}J_{10}^* & J_{10}J_{11}^* & J_{11}J_{10}^* & J_{11}J_{11}^* \end{pmatrix} \right] \\
&\times \frac{1}{\sqrt{2}} \begin{pmatrix} 1 & 1 & 0 & 0 \\ 0 & 0 & 1 & i \\ 0 & 0 & 1 & -i \\ 1 & -1 & 0 & 0 \end{pmatrix} \quad (\text{A2.27})
\end{aligned}$$

This transformation can be really helpful when treating a system of a considerable quantity of elements that by itself produce instrumental polarization, so that way, calculating the Jones matrix and then transforming it to Mueller matrix relieves the work of been calculating 16 parameters. Notice that the inverse of U is equal to the transpose conjugate of itself. Besides, the above representation is for linear basis, the circular transformation differs in the form of the U matrix, and this is:

$$U_{circ} = \frac{1}{\sqrt{2}} \begin{pmatrix} 1 & 0 & 0 & 1 \\ 0 & 1 & i & 0 \\ 0 & 1 & -i & 0 \\ 1 & 0 & 0 & -1 \end{pmatrix} \quad U_{circ}^{-1} = \frac{1}{\sqrt{2}} \begin{pmatrix} 1 & 0 & 0 & 1 \\ 0 & 1 & 1 & 0 \\ 0 & -i & i & 0 \\ 1 & 0 & 0 & -1 \end{pmatrix} \quad (\text{A2.28})$$

A3 Radio-Polarimetry

In section 2.2 was presented the six different diagnostic tools that are used to characterize magnetic fields in the universe. This tools give to astronomers different information about the magnetic field and the medium physics by measuring the state of polarization. After this quick review, it was left on purpose the open question about Zeeman effect and polarization, this because Zeeman effect is the co-protagonist of this thesis project and because before explaining how Zeeman effect is detected and used to measure the magnetic field, it is necessary to explain first what is polarization, techniques used to measure polarization

(section A2, respectively) and now, the basis of single dish radio-polarimetry. The basis of interferometric polarimetry is presented after this section (section A4).

A3.1 Native Linear and Circular Dual Polarization Systems

This section continues with the explained in section A2.4, this makes this part straightforward and less complex to understand. So, remembering, the feed is the antenna (or antennas) that have the mission to illuminate the main reflector of the radio telescope or how is commonly said, feeds the reflector (been fed, the action that does the feed). In Radio Astronomy exist different types of antennas and feeds. The type of the antenna depend on the principal needs of the observation e.g. angular resolution, directivity, high Gain, a broad main beam (lobe) or multiple beams pointing the sky. For this project is necessary a broad beam with low side lobes illuminating the reflector, one for a type of polarization and other for the orthogonal type of polarization. In Heiles (2002) and Robishaw and Heiles (2021) is presented a native dual-polarization feed, that is , two antennas A and B, separated a small distance (the necessary to avoid mutual coupling) where antenna A is sensitive to polarization A and antenna B is sensitive to polarization B. A and B polarization are orthogonal (vertical-horizontal or right-left circular polarization). From the literature that is based this report, the authors define two types of native dual-polarization (DP) system: linear DP Feed and Circular DP Feed, been the first designed to receive linear polarization (vertical and horizontal) and the other one been designed to receive circular polarization (right and left) and the difference can be seen in section A2.4. The image of a diagram in figure A3.1 is a basic example of a DP system, which does not make any distinction in what type of polarization is sensitive. It exist different types of this diagram, however, this one simplify

For this two types of dual-polarization feed or more generally, for a dual-polarization system, the elements need to be adjust to a set of orthogonal polarization, this changes modify the structure of the element Mueller matrix, i.e., depending on the design of the feed, the Mueller matrices will depend of different parameters. The next section summarizes only the Mueller matrices of 4 different elements in our native dual-polarization feed basing on Heiles et al. (2001),

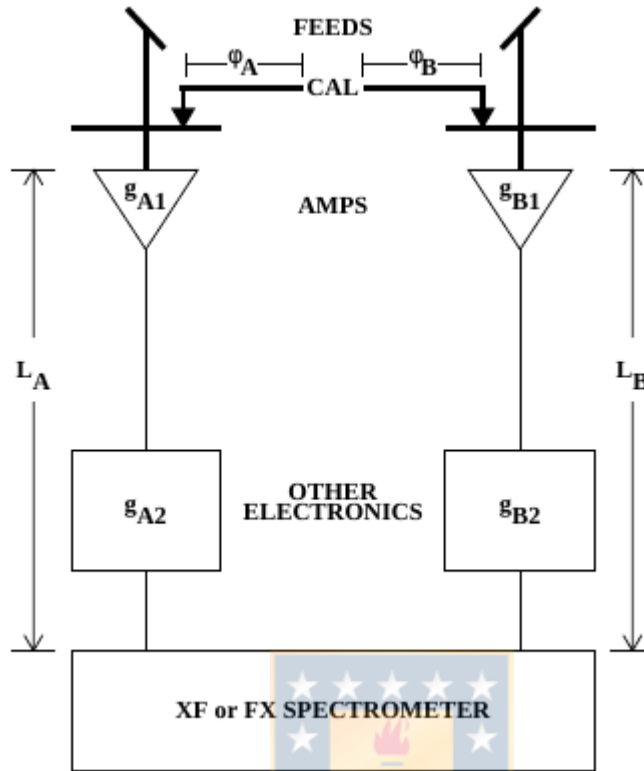


Figure A3.1: Block diagram of dual-polarized (A and B) single-dish system. The noise diode (a.k.a. cal) output is injected through short cables and directional couplers with combined phase delays ϕ_A and ϕ_B . The total voltage gain of polarization channel A is $g_A = g_{A1}g_{A2}$; the voltage gains are complex, with an amplitude and a phase. The total cable length for channel A is length L_A , which includes the run from the dish to the correlator input so it can be very long (more than 1 km at the Green Bank Telescope). The thick lines represent mechanical structures or passive electronics that do not change with time; the thin lines represent active electronics and other circuitry that do change with time and need calibration. Image from [Robishaw and Heiles \(2021\)](#).

however, Mueller formalism is not commonly used to describe the interferometric equation.

A3.2 Element Mueller Matrix

In section [A2.3](#), was explained that the Muller matrix are used to change the type of polarization. In radio polarimetry or more generally, radio telescopes system is formed by a main reflector that reflects the electromagnetic wave to the focus, where is the feed (section [A3.1](#)). Next, is the radio receiver with all the elements that transform the electromagnetic wave depending in what are the intentions

of the observation. Finally, the digital sign ends in a computer where it can be worked. All this process, since the electromagnetic wave is reflected in the main reflector, pass to the radio receiver and ends in the computer, is affected by the elements that produce instrumental polarization. This instrumental polarization and how the electromagnetic wave is affected are manage with the Mueller matrix. The Mueller matrix poses 16 elements that can or can't be independent. The next Mueller matrices are for a dual-polarization feed system (linear or circular) with two antennas sensitive to two orthogonal polarization, that is, antenna A is sensitive to a E_A field and antenna B is sensitive to a E_B .

1. Sky Mueller Matrix

This is the first element Mueller matrix that the radiation encounters and is the rotation matrix or better know as the sky Mueller matrix:

$$\mathbf{M}_{\text{sky}} = \begin{pmatrix} 1 & 0 & 0 & 0 \\ 0 & \cos 2PA_{az} & \sin 2PA_{az} & 0 \\ 0 & -\sin 2PA_{az} & \cos 2PA_{az} & 0 \\ 0 & 0 & 0 & 1 \end{pmatrix} \quad (\text{A3.1})$$

where PA_{az} is the parallactic angle ([A3.2](#)) that is zero in azimuth zero and increase toward the east. Notice that the m_{II} and m_{VV} parameters don't change the state of polarization but the central 2×2 sub-matrix is, of course, nothing but a rotation matrix. This is because the linear polarization parameters (Stokes Q and U) rotates with respect to us, the observer, but Stokes I and V are not affected.

$$PA_{az} = \arctan \left(\frac{\cos \lambda \sin h}{\sin \lambda \cos \delta - \cos \lambda \sin \delta \cos h} \right) \quad (\text{A3.2})$$

2. Feed Mueller Matrix

Also, in section [A2.5](#), was said that from a 2×2 Jones matrix is possible to get a 4×4 Mueller matrix. The following Mueller matrices have their own Jones matrices from where can be.... The second element Mueller matrix is the one associated for the feed that modified the incoming voltages and is defined in [Heiles et al. \(2001\)](#) as

$$\mathbf{M}_F = \begin{pmatrix} 1 & 0 & 0 & 0 \\ 0 & \cos 2\alpha & \sin 2\alpha \cos \chi & \sin 2\alpha \sin \chi \\ 0 & -\sin 2\alpha \cos \chi & \cos^2 \alpha - \sin^2 \alpha \cos 2\chi & -\sin^2 \alpha \sin 2\chi \\ 0 & -\sin 2\alpha \sin \chi & -\sin^2 \alpha \sin 2\chi & \cos^2 \alpha + \sin^2 \alpha \cos 2\chi \end{pmatrix} \quad (\text{A3.3})$$

where α is the amount of coupling into the orthogonal polarization and χ is the phase angle of that coupling. For example, for a native linear feed $\alpha = 0$ and $\chi = 0$; for a native circular feed $\alpha = 45^\circ$ and $\chi = 90^\circ$. For the native circular feed the Stokes parameters are permuted

$$\begin{pmatrix} 1 & 0 & 0 & 0 \\ 0 & 0 & 0 & 1 \\ 1 & 0 & 1 & 0 \\ 1 & -1 & 0 & 0 \end{pmatrix} \begin{pmatrix} I \\ Q \\ U \\ V \end{pmatrix} = \begin{pmatrix} I \\ V \\ U \\ -Q \end{pmatrix} \quad (\text{A3.4})$$

Also, the Jones matrix is

$$\mathbf{J}_F = \begin{pmatrix} \cos \alpha & \sin \alpha e^{i\chi} \\ \sin \alpha e^{i\chi} & \cos \alpha \end{pmatrix} \quad (\text{A3.5})$$

However, the elements are never perfect so the element Mueller matrix for an imperfect feed is

$$\mathbf{M}_{\text{IF}} = \begin{pmatrix} 1 & 0 & 2\epsilon \cos \phi & 2\epsilon \sin \phi \\ 0 & 1 & 0 & 0 \\ 2\epsilon \cos \phi & 0 & 1 & 0 \\ 2\epsilon \sin \phi & 0 & 0 & 1 \end{pmatrix} \quad (\text{A3.6})$$

3. Amplifier Mueller matrix

The amplifier is an electronic element in the system in charge of increase the power of the signal if is required. Continuing with the assumption of two antennas, the two polarization channels go through different amplifier chains, A and B. The Jones matrix of this element is

$$\mathbf{J}_{\text{amp}} = \begin{pmatrix} g_a e^{i\psi_a} & 0 \\ 0 & g_b e^{i\psi_b} \end{pmatrix} \quad (\text{A3.7})$$

which poses the form of phase retarded Jones matrix [A2.2](#). So, for this matrix, the dependent parameters are g_a and g_b that are the voltage gain, and ψ_a and ψ_b which are the phase delays. To obtain the Mueller matrix is possible to use the Jones to Mueller transformation of section [A2.5](#) and also serves as a demonstration, so

$$\mathbf{M}_{\text{amp}} = U[(\mathbf{J}_{\text{amp}} \otimes \mathbf{J}_{\text{amp}}^*)U^{-1}] \quad (\text{A3.8})$$

is equal to

$$\mathbf{M}_{\text{amp}} = \frac{1}{\sqrt{2}} \begin{pmatrix} 1 & 0 & 0 & 1 \\ 1 & 0 & 0 & -1 \\ 0 & 1 & 1 & 0 \\ 0 & -i & i & 0 \end{pmatrix} \left[\begin{pmatrix} G_a & 0 & 0 & 0 \\ 0 & e^{i\psi} & 0 & 0 \\ 0 & 0 & e^{-i\psi} & 0 \\ 0 & 0 & 0 & G_b \end{pmatrix} \frac{1}{\sqrt{2}} \begin{pmatrix} 1 & 1 & 0 & 0 \\ 0 & 0 & 1 & i \\ 0 & 0 & 1 & -i \\ 1 & -1 & 0 & 0 \end{pmatrix} \right] \quad (\text{A3.9})$$

and operating gives

$$\mathbf{M}_{\text{amp}} = \begin{pmatrix} 1 & \frac{\Delta G}{2} & 0 & 0 \\ \frac{\Delta G}{2} & 1 & 0 & 0 \\ 0 & 0 & \cos \psi & -\sin \psi \\ 0 & 0 & \sin \psi & \cos \psi \end{pmatrix} \quad (\text{A3.10})$$

where $\Delta G = G_a - G_b = g_a^2 - g_b^2 \lll 1$ (G_a and G_b are the power gain) and $\psi = \psi_a - \psi_b$. In [Heiles et al. \(2001\)](#), $G_a + G_b = 2$ because they are dealing with fractional polarization and $g_a g_b = 1$.

4. The Total Mueller matrix

The radiation first encounters the feed, producing Stokes parameters as specified by \mathbf{M}_F . Next it suffers the restricted set of imperfections associated with \mathbf{M}_{IF} . Finally it proceeds through the amplifier chains, undergoing \mathbf{M}_{amp} . The product of these matrices, in this order $\mathbf{M}_{\text{tot}} = \mathbf{M}_{\text{amp}} \cdot \mathbf{M}_{\text{IF}} \cdot \mathbf{M}_F$:

$$\mathbf{M}_{\text{tot}} = \begin{pmatrix} 1 & [-2\epsilon \sin \phi \sin 2\alpha + \frac{\Delta G}{2} \cos 2\alpha] & 2\epsilon \cos \phi & [2\epsilon \sin \phi \cos 2\alpha + \frac{\Delta G}{2} \sin 2\alpha] \\ \frac{\Delta G}{2} & \cos 2\alpha & 0 & \sin 2\alpha \\ 2\epsilon \cos(\phi + \psi) & \sin 2\alpha \sin \psi & \cos \psi & -\cos 2\alpha \sin \psi \\ 2\epsilon \sin(\phi + \psi) & -\sin 2\alpha \cos \psi & \sin \psi & \cos 2\alpha \cos \psi \end{pmatrix} \quad (\text{A3.11})$$

Then for a dual linear feed ($\alpha = (0^\circ, 90^\circ)$):

$$\mathbf{M}_{\text{TOT, lin}} = \begin{pmatrix} 1 & \pm(\Delta G/2) & 2\epsilon \cos \phi & 2\epsilon \sin \phi \\ \Delta G/2 & \pm 1 & 0 & \pm 2\delta\alpha \\ 2\epsilon \cos(\phi + \psi) & \pm 2\delta\alpha \sin \psi & \cos \psi & \mp \sin \psi \\ 2\epsilon \sin(\phi + \psi) & \mp 2\delta\alpha \cos \psi & \sin \psi & \pm \cos \psi \end{pmatrix}$$

and for a dual circular feed ($\alpha = (45^\circ, 135^\circ)$):

$$\mathbf{M}_{\text{TOT, circ}} = \begin{pmatrix} 1 & \mp 2\epsilon \sin \phi & 2\epsilon \cos \phi & \pm(\Delta G/2) \\ \Delta G/2 & \mp 2\delta\alpha & 0 & \pm 1 \\ 2\epsilon \cos(\phi + \psi) & \pm \sin \psi & \cos \psi & \pm 2\delta\alpha \sin \psi \\ 2\epsilon \sin(\phi + \psi) & \mp \cos \psi & \sin \psi & \mp 2\delta\alpha \cos \psi \end{pmatrix}$$

Finally the full Mueller matrix will be the product between this matrix and the sky matrix $\mathbf{M}_{\text{tot}} \cdot \mathbf{M}_{\text{sky}}$.

A4 The Radio Interferometric Measurement Equation

The motivation of this project to get into how polarized radiation is detected using an interferometer born by the needs of detect high spectral resolution of Zeeman effect line polarization and sensitivity in filamentary structure at a few hundred of parsecs. The Radio Interferometer Measurement Equation (RIME) is a matrix-based mathematical model that describes the response of a radio interferometer in observation of polarization. This equation, in terms of astronomy years can be considered as new, this equation was first presented in Hamaker et al (1996) [Hamaker et al. \(1996\)](#) and four more papers (a series of 5 papers) and then revisited by O.M. Smirnov (2011) [Smirnov \(2011\)](#). The main difference is that Hamaker

used a *1times4* column vector to represent the correlated products between the antenna pair, named coherency vector and, Smirnov used a 2×2 matrix named visibility matrix which also contains the correlated products. For the derivation of the RIME, lets start with a point source which travel from (z-direction). The electric field can be represented as follow:

$$\mathbf{e} = \begin{pmatrix} e_a \\ e_b \end{pmatrix} \quad (\text{A4.1})$$

Where it has been used an arbitrary notation (a, b) just for the moment. Now, the different changes that the sign suffers can be worked out with Jones formalism (see section A2.2). For example, the changes form electric field to voltage in the feed of one antenna, can be represented as follow:

$$\mathbf{v} = \begin{pmatrix} v_a \\ v_b \end{pmatrix} = \mathbf{J}\mathbf{e} \quad (\text{A4.2})$$

For a full response of an antenna, the Jones matrix of equation A4.2 is referred as the total Jones matrix and contains all propagation effects along the signal path (including electronic effects in the antenna/feed itself). Remembering from A2.2 that the operation is linear and non-commutative, the order here is very important.

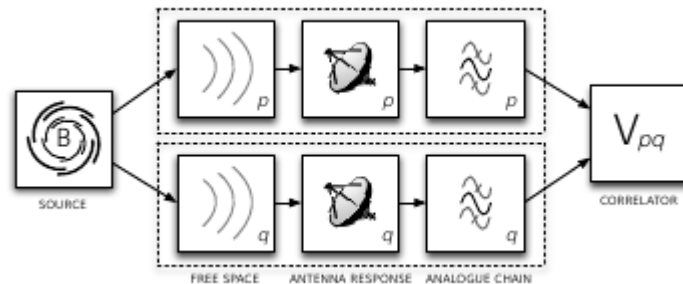


Figure A4.1: Block diagram showing a simple model of an interferometer that can be modelled with the RIME. Radiation from a source propagates through free space to two telescopes, p and q. After passing through the telescope’s analogue chain, the two signals are interfered in a cross-correlator. Credits: D.C. Price and O. Smirnov (2015) [Price and Smirnov \(2015\)](#)

However, lets leave this part here, but we will use it in a few lines. Interferometric observations use arrays of antennas that works in pairs of antennas, two spatially

separated antennas p and q measure two independent voltage vectors \mathbf{v}_p , \mathbf{v}_q . A block diagram for a (simplified) two-element interferometer is shown in Figure A4.1. From left to right, the figure shows the journey of a signal from a source right through to the correlator. The radiation from the source is picked up by two antennas, which we have denoted with subscript p and q. The radiation follows a unique path to both of these antennas; each antenna also has associated with it a unique chain of analogue components that amplify and filter the signal to prepare it for correlation. Each of these sub-scripted boxes may be represented by a Jones matrix; alternatively an overall Jones matrix can be formed for the p and q branches (the dashed areas). In an interferometer, the voltages are fed into a correlator, which produces 4 pairwise correlations between the components of \mathbf{v}_p and \mathbf{v}_q :

$$V_{pq} = 2 \begin{pmatrix} \langle v_{pa}v_{qa}^* \rangle & \langle v_{pa}v_{qb}^* \rangle \\ \langle v_{pb}v_{qa}^* \rangle & \langle v_{pb}v_{qb}^* \rangle \end{pmatrix} = 2(\langle \mathbf{v}_p \otimes \mathbf{v}_q \rangle) = 2(\langle \mathbf{v}_p \mathbf{v}_q^H \rangle) \quad (\text{A4.3})$$

Where the angle brackets denote averaging over some (small) time and frequency bin. For the last expression, the operator \otimes denotes the matrix outer product and H represents the conjugate transpose operation (also called a Hermitian transpose). The Kronecker product is sometimes denoted with this symbol by Hamaker et al but for this operation will be used \otimes . Now we can see how the RIME emerges, Starting with some arbitrarily distant vector \mathbf{e} , our signal travels along two different paths to antennas p and q. Following Eq. (2), each propagation path has its own total Jones matrix, \mathbf{J}_p and \mathbf{J}_q . Combining Eqs. A4.2 and A4.3, we get:

$$\begin{aligned} V_{pq} &= 2 \langle \mathbf{J}_p \mathbf{e} (\mathbf{J}_q \mathbf{e})^H \rangle = 2 \langle \mathbf{J}_p (\mathbf{e} \mathbf{e}^H) \mathbf{J}_q^H \rangle = 2 \mathbf{J}_p \langle \mathbf{e} \mathbf{e}^H \rangle \mathbf{J}_q^H \\ &= 2 \mathbf{J}_p \begin{pmatrix} \langle e_x e_x^* \rangle & \langle e_x e_y^* \rangle \\ \langle e_y e_x^* \rangle & \langle e_y e_y^* \rangle \end{pmatrix} \mathbf{J}_q^H \end{aligned} \quad (\text{A4.4})$$

Where for the last expression it has been used a Cartesian coordinate system to represent the matrix and also has been removed the p and q notation, remembering that the complex conjugate parameters are the one from the antenna q. The use of this Linear coordinate system is because in radio telescope exist at the moment to type of dual polarization systems, linear X-Y and circular R-L. As mentioned

in section A2 the nature of the system will change the mathematical expression, i.e., all the matrices and vectors will be different from one coordinate frame to another, however, the propagation effects do not change. For the last expression in equation A4.4, the one inside the parenthesis is related with Stokes parameters as follows:

$$2 \begin{pmatrix} \langle e_x e_x^* \rangle & \langle e_x e_y^* \rangle \\ \langle e_y e_x^* \rangle & \langle e_y e_y^* \rangle \end{pmatrix} = \begin{pmatrix} I + Q & U + iV \\ U - iV & I - Q \end{pmatrix} = \mathbf{B} \quad (\text{A4.5})$$

Where the last expression is the *brightness matrix* \mathbf{B} , given us the first form of the RIME for a single point source:

$$V_{pq} = \mathbf{J}_p \mathbf{B} \mathbf{J}_q^H \quad (\text{A4.6})$$

which quite elegantly ties together the observed visibilities V_{pq} with the intrinsic source brightness \mathbf{B} , and the per-antenna terms \mathbf{J}_p and \mathbf{J}_q . Is important to mark that a real-world interferometer will have some "corrupting" effects in the signal path, in addition to the nominal phase delay, so, all this effects are considered in the Jones matrix.

Finally the RIME for multiple discrete sources and for a continuous brightness distributions are as follow:

- **Multiple N discrete sources:**

$$V_{pq} = \sum_s \mathbf{J}_{sp} \mathbf{B}_s \mathbf{J}_{sq}^H \quad (\text{A4.7})$$

Where the s is the s -source from the total N . The contributions of each source to the measured visibility matrix V_{pq} add up linearly. The signal propagation path is different for each source s and antenna p , but each path can be described by its own Jones matrix \mathbf{J}_{sp} .

- **Continuous brightness distribution:**

In the more general case, the sky is not a sum of discrete sources, but rather a continuous brightness distribution $\mathbf{B}(\sigma)$, where σ is a (unit) direction

vector. For each antenna p , we then have a Jones term $\mathbf{J}_p(\sigma)$, describing the signal path for direction σ . To get the total visibility as measured by an interferometer, we must integrate Eq. A4.4 over all possible directions, i.e. over a unit sphere:

$$V_{pq} = \int_{4\pi} \mathbf{J}_p(\sigma) \mathbf{B}(\sigma) \mathbf{J}_q^H(\sigma) d\Omega \quad (\text{A4.8})$$

A5 Sensitivity

Sensitivity is a measure of the weakest source of radio emission that can be detected [Wrobel and Walker \(1999\)](#). It is a figure of merit as far as radio observations are concerned, as well as other parameters that are derived from this parameter or are related, therefore, its measurement is important, however, there is a parameter before this is also used to measure the performance of an antenna, this parameter is the equivalent flux density of the system or better known by its acronym SEFD (System Equivalent Flux Density ^{1 2 3}). To calculate this parameter, it was used the standard equation below

$$SEFD = 2k_B T_{sys} / \eta_a * A_p = \frac{2k_B T_{sys}}{A_{eff}} \quad (\text{A5.1})$$

Where k_B is the Boltzman's constant (1.38×10^{-23} J/K = 1.38×1000 Jy/K), η_a is the antenna efficiency, A_p is the physical or geometric area of the antenna equal to $\pi D^2/4$ and T_{sys} is the system temperature. Sometimes it can be found expressed as

$$SEFD = \frac{T_{sys}}{K} \quad (\text{A5.2})$$

Where $K = (\eta_a A_p) / (2k_B)$ ⁴ it is simply the gain or *sensitivity*, it is not the sensitivity that we are looking for, rather, it is a measure of the performance of

¹System Equivalent Flux Density is defined as the flux density of a source that would deliver the same amount of power

²SEFD is defined as the flux density of a radio source that doubles the system temperature

³which are formally defined as the measured flux density of an unresolved source within a telescope's beam that would double the total system noise.

⁴This parameter is also known as DPFU or Degrees per Flux Unit

the antenna. In addition, higher SEFD translates to low sensitivity, therefore, this value is sought to be small. Additionally, this value times the power signal-to-noise ratio $r_{S/N}$ is equivalent to the source flux density [S. Issaoun et al \(EHT memo 2017\)](#). Therefore, the SEFD takes into consideration the efficiency and collection area of the antenna, plus the noise of the system. In summary, the overall performance of an antenna is measured by the SEFD in units of Janskys.

$$SEFD = \frac{T_{sys}e^\tau}{\eta_l G} \Rightarrow S_{source} = SEFD \times r_{S/N} \quad r_{S/N} = \eta_l e^{-\tau} \frac{T_{src}}{T_{sys}} \quad (A5.3)$$

Now going back to the "basics", the radiometer equation gives us the signal to noise ratio of an antenna:

$$S/N = T_{src}/T_{rms} = T_{src}/\frac{T_{sys}}{\sqrt{\Delta\nu\tau}} = \frac{T_{src}}{T_{sys}}\sqrt{\Delta\nu\tau} \quad (A5.4)$$

However, it is convenient to work this value based on the SEFD. Using:

$$T_{src} = \frac{A_{eff}}{2k_B} S_\nu \quad A_{eff} = \frac{\lambda^2}{4\pi} G \quad (A5.5)$$

we have:

$$T_{src} = \frac{T_{sys}}{\sqrt{\Delta\nu\tau}} = \frac{A_{eff}}{2k_B} S_\nu \Rightarrow S_{\nu,rms} = \frac{2k_B T_{sys}}{A_{eff} \sqrt{\Delta\nu\tau}} = SEFD/\sqrt{\Delta\nu\tau} \quad (A5.6)$$

As a useful data $\sqrt{\Delta\nu\tau} = \sqrt{n}$, where n is the number of data points.

A5.0.1 Interferometer sensitivity

Each antenna will have its own SEFD, so for an antenna pair we have $SEFD_i$ and $SEFD_j$. Also, accumulation time τ_{acc} , system efficiency η_s . The full derivation of the following value can be found in [Wrobel and Walker \(1999\)](#). The sensitivity of an interferometer will be (in Jansky):

$$\Delta S_{ij} = \frac{1}{\eta_s} \times \sqrt{\frac{SEFD_i SEFD_j}{2\Delta\nu\tau_{acc}}} = \frac{1}{\eta_s} \times \frac{SEFD}{\sqrt{2\Delta\nu\tau_{acc}}} \quad (\text{A5.7})$$

If we consider that SEFD is the same for each antenna.

$$\Delta I_m = \Delta S/\sqrt{L} \quad L = \frac{1}{2}N(N-1) \times \frac{\tau_{int}}{\tau_{acc}} \quad (\text{A5.8})$$

A5.0.2 Sensitivity in imaging (NRAO)

$$\Delta I_m = \frac{SEFD}{\eta_c \sqrt{n_{pol} N(N-1) \tau_{int} \Delta\nu}} \quad (\text{A5.9})$$

Sensitivity in imaging (for ALMA technical handbook ⁵):

$$\begin{aligned} \sigma_s &= \frac{w_r 2k_B T_{sys}}{\eta_q \eta_c A_{eff} (1-f_s) \sqrt{N(N-1) n_p \Delta\nu \tau_{int}}} \\ &= \frac{w_r SEFD}{\eta_q \eta_c (1-f_s) \sqrt{N(N-1) n_p \Delta\nu \tau_{int}}} \end{aligned} \quad (\text{A5.10})$$

Point Source Sensitivity (Butler & Wootten 1999 - [ALMA Memo. No. 276](#)):

For this equation we use D in meters.

$$\Delta S = \frac{4\sqrt{2}kT_{sys}}{\gamma\epsilon_q\epsilon_a\pi D^2 \sqrt{n_p [N(N-1)/2] \Delta\nu \Delta t}} \quad (\text{A5.11})$$

Spectral Line Sensitivity (Butler & Wootten 1999 - [ALMA Memo. No. 276](#)):

For this equation we use D in meters and change $\Delta\nu$ to $\nu\Delta\nu/c$. Also, in the last expression is better to change the units of the observed frequency in GHz and the speed of light in km per GHz, this is $c[km/s] = c[km \times Hz] = c[km \times Hz] \times 10^{-9} = c[km \times GHz]$ being equal to 0.0003 km per GHz.

$$\Delta S = \frac{2kT_{sys}\sqrt{c}}{\gamma\epsilon_q\epsilon_a A_p \sqrt{n_p [N(N-1)] \nu_{GHz} \Delta v_{km/s} \Delta t}} \quad (\text{A5.12})$$

Brightness Temperature Sensitivity (Butler & Wootten 1999 - [ALMA Memo. No. 276](#)):

⁵<https://almascience.eso.org/documents-and-tools/cycle8/alma-technical-handbook/view>

$$\Delta T = \frac{\Delta S \lambda^2}{2k\Omega_s} \quad (\text{A5.13})$$

Where Ω_s is the synthesized beam solid angle, and is equal to:

$$\Omega_s = \frac{\pi}{4 \ln 2} \theta_s^2 \quad \theta_s = 76 / B_{max,km} / \nu_{GHz} \quad \text{The last expression is easy to demonstrate} \quad (\text{A5.14})$$

So:

$$\Delta T = \frac{2 \ln 2}{\pi k} B_{max}^2 \Delta S = 0.32 B_{max,km}^2 \Delta S_{mJy} \quad (\text{A5.15})$$

$S_\nu \rightarrow T_b$:

Link of full demonstration in [TBconv](#).

$$T = 1.222 \times 10^3 \frac{I}{\nu^2 \theta_{maj} \theta_{min}} \quad (\text{A5.16})$$

Where I is in unit of mJy/beam, the frequency in GHz and θ_{maj} and θ_{min} are the half-power beam widths along the major and minor axes, respectively, in units of arcsec.